
Template-assisted growth and characterization of ZnO-based nanowire arrays and 3D networks

Application of nanowire networks for photoelectrochemical water splitting

Templat-gestütztes Wachstum und Charakterisierung von ZnO-basierten Nanodrahtarrays und 3D Netzwerken

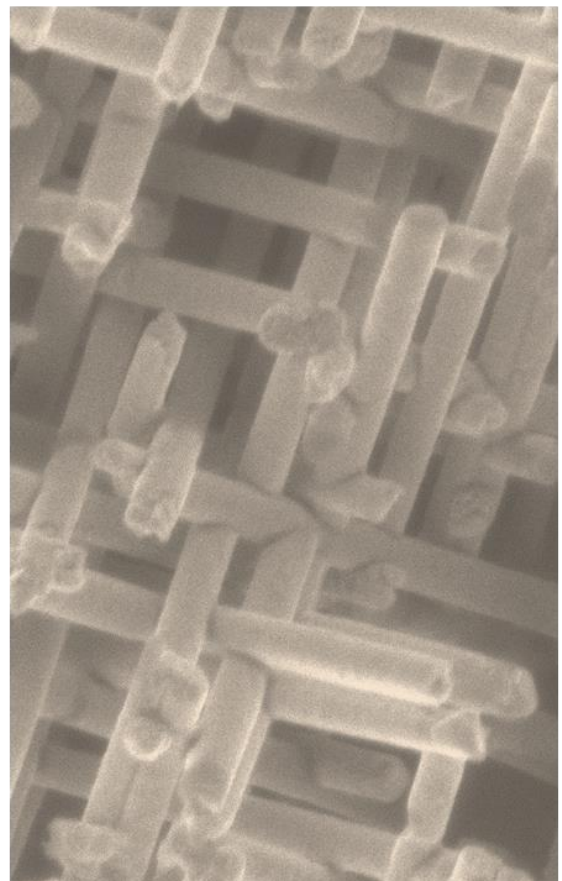
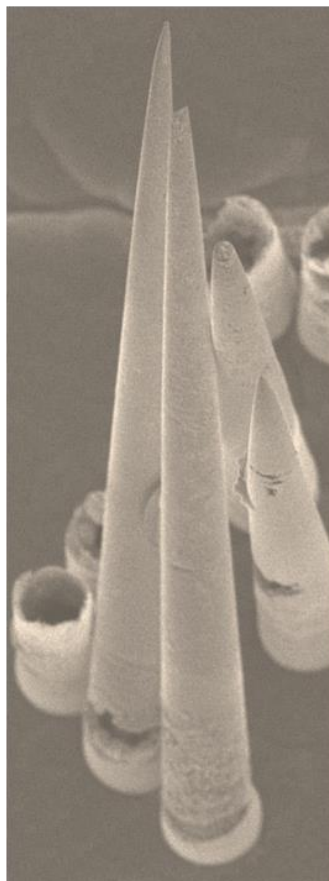
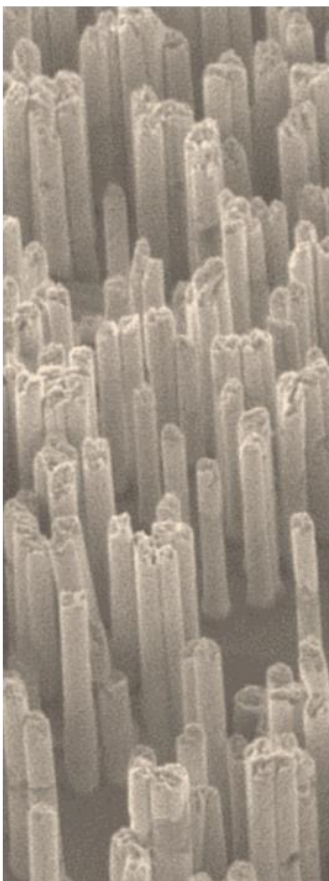
Zur Erlangung des Grades eines Doktors der Naturwissenschaften (Dr. rer. nat.)
genehmigte Dissertation von **M.Sc. Liana Movsesyan** aus Jerewan (Armenien)

Tag der Einreichung: 19.07.2016, Tag der Prüfung: 06.10.2016

1. Gutachten: Prof. Dr. Christina Trautmann
2. Gutachten: Prof. Dr. Wolfram Jaegermann

Material- und Geowissenschaften, D17

Darmstadt - 2017



Templateassisted growth and characterization of ZnO based nanowire arrays and 3D networks

Application of nanowire networks for
photoelectrochemical water splitting

Liana Movsesyan

2016

Template-assisted growth and characterization of base nanowire arrays and 3D networks: application of nanowire networks for photoelectrochemical water splitting

Templatgestütztes Wachstum und Charakterisierung von basierten Nanodrahtarrays und 3D Netzwerken Anwendung der Nanodrahtnetzwerke für elektrochemische Wasserspaltung

Genehmigte Dissertation von M.Sc. Liana Movsesyan aus Jerewan (Armenien)

1. Gutachten: Prof. Dr. Christina Trautmann
2. Gutachten: Prof. Dr. Wolfram Langemann

Tag der Einreichung: 19. Juli 2016

Tag der Prüfung: 06. Oktober 2016

Darmstadt 17

Bitte zitieren Sie dieses Dokument als:

URN: urn:nbn:de:tuprints:5444

URL: <http://tuprints.ulb.tu-darmstadt.de/5444>

Dieses Dokument wird bereitgestellt durch

E-Publishing Service der TU Darmstadt

<http://tuprints.ulb.tu-darmstadt.de>

tuprints@ulb.tu-darmstadt.de



Die Veröffentlichung steht unter folgender Creative Commons Lizenz:

Namensnennung Keine kommerzielle Nutzung Keine Bearbeitung 4.0 International

<https://creativecommons.org/licenses/by/4.0/>

Erklärung zur Dissertation

Hiermit versichere ich, Liana Movsesyan, die vorliegende Dissertation ohne Hilfe Dritter nur mit den angegebenen Quellen und Hilfsmitteln angefertigt zu haben. Die aus den Quellen entnommen wurden, sind als solche kenntlich gemacht. Diese Arbeit hat in oder ähnlicher Form noch keiner Prüfungsbehörde vorgelegen.

Datum: 19.07.2016

Unterschrift:

I herewith formally declare that I have written the submitted thesis independently. I did not use any outside support except for the quoted literature and other sources mentioned in the paper. I clearly marked and separately listed all of the literature and all of the other sources which I employed when producing this academic work, either literally or in content. This thesis has not been handed in or published before in the same or similar form.

In the submitted thesis the written copies and the electronic version are identical in content.

Date: 19.07.2016

Signature:

The work presented in this thesis has been conducted at the Materials Research Group of the GSI Helmholtz Center for Heavy Ion Research. It was sponsored by the scholarship program from Beilstein Institute for Advancement of Chemical Sciences (Frankfurt), DFG 1583 and DFG SPP 1613 projects.

ō Y g " c t g " x k u k v q t u
here for one hundred years at the very
most. During that period we must try
to do something good, something
useful with our lives. If you contribute
to other people's happiness, you will
h k p f " v j g " v t w g " o g

Dalai Lama XIV

Table of Contents

Abstract	vii
Zusammenfassung	ix
Introduction	xi
1. Theoretical background	1
1.1. Ion-track technology	1
1.2. Electrodeposition	3
1.3. Structural and physical properties of ZnO	6
1.3.1. Crystal structure	7
1.3.2. Band structure	7
1.3.3. Electrical properties	8
1.4. Photoelectrochemical water splitting	9
1.5. Metalsemiconductor contact	13
2. Sample preparation and characterization methods	16
2.1. High resolution scanning electron microscopy (HRSEM)	16
2.2. Energy dispersive X-ray spectroscopy (EDX)	17
2.3. X-ray diffraction (XRD)	18
2.4. High resolution transmission electron microscopy (HRTEM)	18
2.5. Photoelectrochemical (PEC) measurements	19
2.6. X-ray photoelectron spectroscopy (XPS)	19
3. Fabrication of etched track membranes	22
3.1. Parallel cylindrical pores by symmetric etching	22
3.2. Vertically aligned conical pores by asymmetric etching	25
3.3. Membranes with networks of interconnected pores	25
4. Electrodeposition and characterization of ZnO nanowires	30
4.1. Cylindrical micro and nanowires	30
4.1.1. Preparation of the electrode	31
4.1.2. Synthesis of arrays with parallel cylindrical ZnO wires	32
4.1.3. Influence of the electrolyte concentration on the morphology of the wires	33
4.1.4. Influence of the applied potential on the morphology and texture of the wires	33
4.1.5. Relation between nanowire diameter and crystallographic properties	36
4.1.6. Crystallographic properties and composition depending on wire length	39
4.1.7. Mechanical stability of the arrays	40
4.2. Vertically aligned conical ZnO wires	41
4.3. Nanowire networks	47
4.3.1. Optimization of growth conditions for ZnO networks	48
4.3.2. Enhancement of the mechanical stability of the networks	51
5. ZnO nanowires and nanowire networks as TiO ₂ shell	56
5.1. ZnO nanowires with amorphous TiO ₂	56
5.2. ZnO and ZnO/anatase TiO ₂ core/shell nanowire networks	59

6. Photoelectrochemical measurements	67
6.1. Description of film and nanowire network photoanodes	67
6.2. Photoelectrochemical performance of nanowire networks vs. films	69
6.3. XPS analysis of ZnO and ZnO ₂ /TiO ₂ nanowire photoanodes	77
Summary and Outlook	84
Appendices	87
A: Etching rates of network based membranes	87
B: ZnO nanotube networks by electrochemical deposition	87
C: TiO ₂ nanotube networks by atomic layer deposition	88
D: Si nanowire networks	90
E: Sample preparation for TEM measurements	91
F: Au nanowire networks	92
G: PEC measurements of ZnO/TiO ₂ network with tuned wire diameters	92
References	94
Acknowledgments	102
Curriculum Vitae Liana Movsesyan	105
Í G W] Y b WY ' U g ' 5 f h Í ' [U ` ` Y f m	109

Abstract

In recent years, research on the fabrication of semiconductor nanowires has attracted increasing interest in various fields of research. Especially, the successful synthesis of ZnO micro- and nanoscale structures has paved the way to numerous applications for devices including nanogenerators, sensors, solar and fuel cells.

This work focuses on the synthesis of ZnO nanowire arrays and nanowire networks by electrochemical deposition in etched membranes. Three different geometries of nanowire-based structures are discussed: (1) vertically aligned cylindrical ZnO nanowires, (2) ZnO nanocones, as well as (3) mechanically stable three-dimensional (3D) ZnO and ZnO/TiO₂ nanowire networks.

To establish a reproducible growth process of ZnO etched membranes, the electrodeposition parameters of vertically aligned cylindrical ZnO nanowires are investigated by independently varying the applied potential during the electrodeposition, the thickness of the membranes, and the concentration of the electrolyte (Zn(NO₃)₂). The influence of these parameters on the morphological and crystallographic properties of the nanowires is analysed by means of high resolution scanning electron microscopy (HRSEM) and X-ray diffraction (XRD). ZnO nanocone arrays with μm size bases and nm size tips are fabricated applying two growth approaches: base and tip base. The arrays are analysed by SEM in terms of mechanical stability.

An important part of this thesis is the design and synthesis of 3D ZnO nanowire networks. The number density and diameter of nanowires in the network are optimized to obtain mechanically stable 3D building blocks with a high surface area. The crystallographic properties are studied by XRD, high resolution transmission electron microscopy (HRTEM), selected area electron diffraction (SAED), and angle annular darkfield (HAADF) imaging. Knowledge drawn from these investigations is crucial for the implementation of these 3D nanoarchitectures into devices, such as photodiodes and electrodes.

Furthermore, the stability of ZnO-based nanowire networks in aqueous environment under applied potential and illumination is tested. In particular, they are employed as photoanode model systems for photoelectrochemical water splitting. The measurements are performed on pure ZnO and core/shell ZnO/TiO₂ nanowire networks compared to those of their film counterparts. The role of the TiO₂ layer as a protection layer against photo(electro)chemical corrosion of ZnO as well as the efficient charge separation and transport from nanowires to the electrolyte is highlighted.

By using X-ray photoelectron spectroscopy (XPS) contamination and chemical composition on the surface of the networks are quantified before and after photoelectrochemical measurements. Additionally, a Schottky barrier is formed at the

ZnO-Au and TiO₂-Au contacts are theoretically determined from the values of the work function and the valence band position.

The work presented in this thesis shows how the outstanding flexibility of the atomic layer deposition technology combined with electrochemical deposition opens new options for fabrication of complex ZnO-based nanowire structures. The possibility to control the length, diameter and orientation allows the production of standing high aspect ratio structures which are promising for a wide range of applications, including energy conversion and storage.

Zusammenfassung

In den letzten Jahren hat die Herstellung von Halbleitern Nanodrähten zunehmendes Interesse in verschiedenen Forschungsgebieten geweckt. Insbesondere eröffnet die erfolgreiche Synthese von ZnO Mikro- und Nanostrukturen eine Vielzahl von Anwendungen z.B. Nanogeneratoren, Sensoren, Solar- und Brennstoffzellen.

Die vorliegende Arbeit konzentriert sich auf die Synthese von ZnO Nanodrahtarrays, Nanodrahtnetzwerken mittels elektrochemischer Abscheidung in geätzten Ionenspurmembranen. Drei verschiedene Geometrien von Nanodrahtstrukturen wurden abgeschieden und analysiert: vertikal ausgerichtete Arrays von (1) zylindrischen (2) konischen ZnO Nanodrähten sowie (3) mechanisch stabile dreidimensionale (3D) ZnO/TiO₂ Nanodrahtnetzwerke.

Um einen reproduzierbaren Wachstumsprozess von ZnO in Ionenspurmembranen zu erzielen, wurden die Abscheidungsparameter für vertikal ausgerichtete zylindrische Nanodrähte sowie die angelegte Spannung, der Durchmesser der Poren in den Membranen, und die Konzentration des Elektrolyten (Zn(NO₃)₂) unabhängig voneinander variiert. Der Einfluss dieser Parameter auf die morphologischen und kristallographischen Eigenschaften der Nanodrähte wurde mittels hochauflösender Rasterelektronenmikroskopie (HRSEM), Röntgenbeugung (XRD) analysiert. Konische ZnO Nanodrahtarrays mit µm breiten Basen und nm großen Spitzen wurden mit zwei verschiedenen Wachstumsmethoden hergestellt. Die mechanische Stabilität dieser Nanostrukturen wurde mit Hilfe von Rasterelektronenmikroskopie hinsichtlich ihrer mechanischen Stabilität untersucht.

Ein wichtiger Teil dieser Arbeit ist die Entwicklung und Synthese von 3D ZnO Nanodrahtnetzwerken. Die Anzahl und der Durchmesser dieser Nanodrähte wurden optimiert, um mechanisch stabile 3D Strukturen mit großer Oberfläche zu erhalten. Die Kristallstruktur wurde mittels XRD, hochauflösender Transmissionselektronenmikroskopie (HRTEM), Feinbereichsbeugung (SAED) und Ringdunkelfeldabbildung (HAADF) untersucht. Die hierdurch erhaltenen Erkenntnisse sind wichtig für die Implementierung dieser 3D Nanoarchitekturen in komplexere Bauteile wie z.B. Photodioden.

Die Lebensdauer von ZnO-basierten Nanodrahtnetzwerken in wässriger Umgebung wurde bei angelegter Spannung und unter künstlichem Sonneneinstrahlung (Solar, AM 1.5) getestet. Die Netzwerke dienten als Modellsystem für Photoanoden zur photoelektrochemischen Wasserspaltung. Die Messungen wurden für reine ZnO und Core/Shell ZnO/TiO₂ Nanodrahtnetzwerke durchgeführt und mit den entsprechenden Referenzstrukturen verglichen. Die Rolle der TiO₂ Schicht als Schutzschicht gegen photo(elektro)chemische Korrosion von ZnO sowie für einen effizienten Ladungstransport aus den Nanodrähten zum Elektrolyten wird erörtert.

Mittels Röntgenphotoelektronenspektroskopie (XPS) wird die Kontaminationen und die chemische Zusammensetzung der Oberfläche der Nanodrahtnetzwerke vor und nach photoelektrochemischen Messungen quantifiziert. Zusätzlich werden die Höhen der Schottkybarriere an den ZnO- und TiO₂-Au Kontakten aus den Werten der Austrittsarbeit und Valenzbandposition theoretisch bestimmt.

Die durchgeführten Arbeiten zeigen, wie die große Flexibilität der Ionenspurtechnologie in Verbindung mit elektrochemischer Abscheidung zu neuen Verfahren zur Herstellung komplexer ZnO-basierter Nanodrahtsysteme führen kann. Die Möglichkeit die Länge, den Durchmesser und die Orientierung dieser Nanodrähte frei wählen zu können, erlaubt die Herstellung freistehender Strukturen mit hohem Aspektverhältnis, die für ein breites Spektrum an Anwendungen, wie z.B. für Energieumwandlung und -speicherung, geeignet sind.

Introduction

Nanoscale engineering is one of the most prominent and actual research topics nowadays. The demand for more advanced and next generation devices leads to extensive research effort in nanoscale technology. For miniaturization and increasing of the device efficiency, dimensionally nanowires are of great interest. In particular, nanowires are excellent model systems for the investigation of size and geometry effect on physical characteristics such as optical^{1,6}, electrical,^{7,10} magnetic,^{11,14} electronic,^{15,17} and thermal^{18,20} properties. In addition, the integration of nanowires into micro and macro devices requires the development of strategies to assemble them into three-dimensional (3D) building blocks with enhanced mechanical stability, flexibility and high surface area.

ZnO micro and nanoscale structures have attracted tremendous interest for numerous applications. Studies on ZnO nanostructures are motivated by the technologically relevant properties of ZnO including transparency, piezoelectricity, natural type conductivity, high thermal stability, high electron mobility ($>100\text{ cm}^2/\text{Vs}$), a wide direct band gap of 3.3–3.6 eV, as well as a large exciton binding energy of 60 meV. Additional advantages of ZnO include its non-toxicity as bulk material, low cost, and the wide availability on earth. These properties make ZnO nanoparticles promising for the integration in a wide range of devices including transistors,²³ sensors,^{24,25} nanogenerators, piezoelectric devices, solar cells,^{23,27,28} and photoelectrodes for water splitting, protected and/or integrated in tandem cells.^{29,30} The application of ZnO in photodetectors, light emitting diodes, and laser diodes that operate in the blue and ultraviolet region of the light spectrum are also being studied. ZnO nanowires embedded in membranes may for example serve as X-ray detectors.³⁴

ZnO nanostructures are fabricated by top-down methods including electron beam and optical lithography,^{35,36} as well as by bottom-up methods such as gas synthesis,³⁷ metal organic chemical vapor deposition,³⁸ and electrodeposition from a seed layer.³⁹ However, a large scale production of ZnO wires with these techniques is limited by various factors including time and cost efficiency or control and tuning of size and geometry. Template-assisted electrodeposition combines both approaches and enables the synthesis of nanowires with simultaneous control over length, diameter, and composition.^{40,43} The template method has demonstrated to be very suitable for fabrication of metal and semiconductor structures with tuned size and crystallinity. By adjusting the growth parameters, Teteris, Molares *et al.* showed that it is possible to grow both single and polycrystalline Cu nanowires inside polycarbonate track-etched membranes.⁴⁴ Pan *et al.* reported the synthesis of single crystalline Ni and Co nanowires in an aluminum oxide (AAO) templates.⁴⁵ However, reports on the electrodeposition of semiconductor nanowires in polymer templates are rather limited, in part similar for Zn. *et al.* reported the electrodeposition of ZnO nanowires in polymer membranes with pores of few hundred nm diameter using Zn(NO₃)₂ electrolyte. *incotet et al.* studied

the electrochemical growth of ZnO nanowires from Zn(OH)₂ in AAO templates and compared the results with the growth of pure Zn nanowires. The influence of the applied potential during pulsed electrodeposition on the morphology and crystallographic properties of ZnO films was studied by Manzano⁴⁸. However, the influence of the potentiostatic deposition conditions on the structure and morphology of ZnO nanowires with diameters, as reported in this thesis, has not been discussed before. This is important in order to understand relevant properties such as electrical resistivity, charge carrier generation and transport, and photoluminescence of the wires, which play an important role in the efficiency of ZnO nanowire-based devices.

To date, the synthesis of nanowire and nanorod-based 3D architectures continues being a challenge. The synthesis of tungsten oxide nanowire networks by thermal evaporation approach was reported by Zhou *et al.*⁴⁹ and Ponzoni *et al.*⁵⁰. The growth of nanowires along six crystallographically equivalent directions resulted in the intersection of rectangular nanowires and the formation of a network with a junction angle of nearly 90°. These structures show good crystallinity, however, the width of the wires was not controlled, ranging from several tens of nm to 200 nm. Moreover, the size of networks as a continuous system is only 1-10 μm. Wang *et al.* reported the synthesis of ZnO connected networks by a high temperature vapor deposition process.⁵¹ The network consisted of nanorods and nanowires with diameters of 10-20 nm. These mesh-like structures have a uniform height of 120 μm, however, they exhibit an inhomogeneous distribution over the substrate. The main drawback of this technique is the limited and non-controlled interconnectivity between adjacent nanowires, large diameter distribution and the limited height up to 30 μm. Moreover, only a few compounds are endowed with an ability to grow in 3D building blocks.

These limitations and challenges can be circumvented by using template-based growth with pre-designed templates including mesoporous silica, anodic alumina and track polymer membranes. Let *et al.* performed electrodeposition of different metal and semiconductor networks in 3D mesoporous silica⁵². The diameters of the network ligaments ranged from 2 to 20 nm. However, with the existing technology, it is challenging to obtain large scale networks with controlled porosity and height larger than several microns. A successful fabrication of ordered 3D interconnected nanoarchitectures in anodic porous alumina was achieved by Martín⁵³. These templates are prepared by a two-step anodization process and consist of a well-ordered nanotubular network with a 100 nm range. Although the position and amount of junctions can be precisely adjusted by the anodization parameters, the angle between the pores at the junctions is fixed at 90° and no optimization for this parameter has been reported yet. Additionally, a pore widening is observed in these networks, which still needs to undergo optimization in order to obtain networks with a uniform pore diameter.

Among the templated techniques for fabrication of hierarchical structures, track technology is very attractive because it allows for easy tuning of the height (up to 100 μm) and area (up to $\sim 20^2 \text{ cm}^2$) of the network, the diameter (20 to few hundreds of nm), number density (up to 10^8 cm^{-2}) and interconnectivity of the wires in the template as well as the angle between interconnected wires. 3D structured templates based on irradiation performed at the GSI Helmholtz Center for Heavy Ion Research have been successfully used for electrochemical deposition of ZnO,⁵⁴ Sb⁵⁵ and Ag⁵⁶ nanowire networks, electroless plating of Au, Ni, Cu, Pt and Ag⁵⁷ and atomic layer deposition of Al₂O₃, SiO₂ and TiO₂⁵⁸ nanotube networks as well as Pt, Cu and Ag superstructures consisting of interconnected nanowires and microscale pores.⁵⁹ The compact design, mechanical stability and high surface area of nanowire based 3D hierarchical systems can be advantageous for example to facilitate efficient light absorption and charge transport in photoelectrodes^{30,60,63} and optical elements^{64,65} to enhance the performance of sensors,^{50,66} batteries^{67,68} and supercapacitors⁶⁹ or to achieve high electric field confinement and enhancement in plasmonic hollow nanocavities,⁷⁰ as well as for computer and chip technologies.⁷¹

This thesis focuses on the synthesis and characterization of ZnO nanowire based structures applying track technology in combination with electrochemical deposition. The overall goal of this work has been to optimize irradiation, etching and electrodeposition parameters to achieve a reproducible and controlled growth of ZnO nanostructures. Detailed analysis of the shape, size, morphology and crystallinity of the wires is of prime importance for applications.

Three different geometries were studied namely arrays of vertically aligned cylindrical nanowires and nanocones as well as nanowire networks. It is shown that applying a low concentration of the electrolyte leads to the growth of nanowires with a smooth surface. Varying the applied potential of the electrodeposition, the texture of ZnO wires changes. The nanopore diameter is found to be a tool to vary the preferred orientation of the wires. The mechanical stability of cylindrical nanowire arrays after dissolution of the polymer is studied by altering the aspect ratio (length to diameter of the wire). Membranes with conical pores are employed as templates for the electrodeposition of conical ZnO wires. Two growth approaches are discussed, top-down and bottom-up. In both cases, the arrays are polycrystalline, but the morphology changes significantly depending on the growth direction.

ZnO nanowire networks with different nanowire diameters and number densities were synthesized, and these parameters were optimized to obtain reproducible, freestanding and stable structures. The growth density of these networks was improved by adding one more irradiation step to the standard network irradiation process and applying a mask over a predefined area. Additionally, photoelectrochemical performance of ZnO and core/shell ZnO/TiO₂ nanowire networks was tested and compared to their film counterparts, resulting in higher photocurrents for the network structures. The surface imaging before and

photoelectrochemical measurements shows that the TiO₂ layer protects the ZnO network from corrosion and morphological changes.

The thesis is composed of six chapters. Chapter 1 describes the theoretical background and working principle of the techniques used for this thesis as well as the characteristic parameters of ZnO relevant for the explanation of the results. Chapter 2 introduces the methods of characterization and the measurement techniques. Chapter 3 depicts the preparation processes of membranes with vertically aligned cylindrical and conical channels as well as networks of interconnected nanowires. The main results of the synthesis, growth optimization and characterization of ZnO cylindrical and conical wire arrays as well as nanowire networks are presented. Chapter 4 The characterization of crystallinity and composition of pure ZnO and ALD-coated ZnO/TiO₂ core/shell nanowires and networks is presented. Chapter 5 Lastly, Chapter 6 sheds light on the photoelectrochemical measurements performed with bare ZnO and core/shell ZnO/TiO₂ nanowire networks in order to test their reliability and stability for future applications. The morphology and composition of the surface before and after the measurements is discussed.

1. Theoretical background

This chapter introduces the concepts of the triode technology and electrical deposition in polymeric membranes. The main properties of ZnO, which are relevant for this thesis, are elucidated. The working principle of photoelectrochemical water splitting at semiconductor contacts is described.

1. Theoretical background

1.1. Ion-track technology

When passing through matter, heavy ions dissipate their energy mainly because of elastic and inelastic coulomb interactions with atoms of the material if the ion velocity is low (0.01 MeV per nucleon (MeV/u), elastic collisions (nuclear energy loss) dominate whereas at higher ion velocities the interaction is influenced by inelastic collisions that lead to ionization and electronic excitation processes (electronic energy loss) for the fabrication of track membranes swift heavy ions of several MeV/u are used. This energy loss per unit path length (dE/dx) is based on electronic stopping energy loss related to the charge of the ion projectile and is described by the Bethe-Bloch formula:

$$(1)$$

where m_e is the mass of the electron, v is the velocity of the ion, (c is the speed of light) Z is the charge state of the ion, N is the number density of the electrons in the material A is the atomic number of the target, and I is the mean ionization potential of atoms in the target medium, through which the particle is passing correction factors, which take relativistic effects into account. The main conclusions arising from the Bethe-Bloch formula are the following: the energy loss (also called stopping power) depends on the charge of the ion, the electron density of the material, and it is a function of the ion velocity, v/c . In the case where the stopping of the ions in the material is mainly derived from inelastic collisions, nuclear stopping is often ignored. The energy loss of Bi ions in polycarbonate as a function of the ion energy per nucleon calculated by means of the SRIM-2003 code (Stopping and Range of Ions in Matter) is shown in Figure 1a in a double logarithmic scale. The dashed green and red curves correspond to electronic and nuclear energy loss, respectively, and the solid blue curve represents the total energy loss.

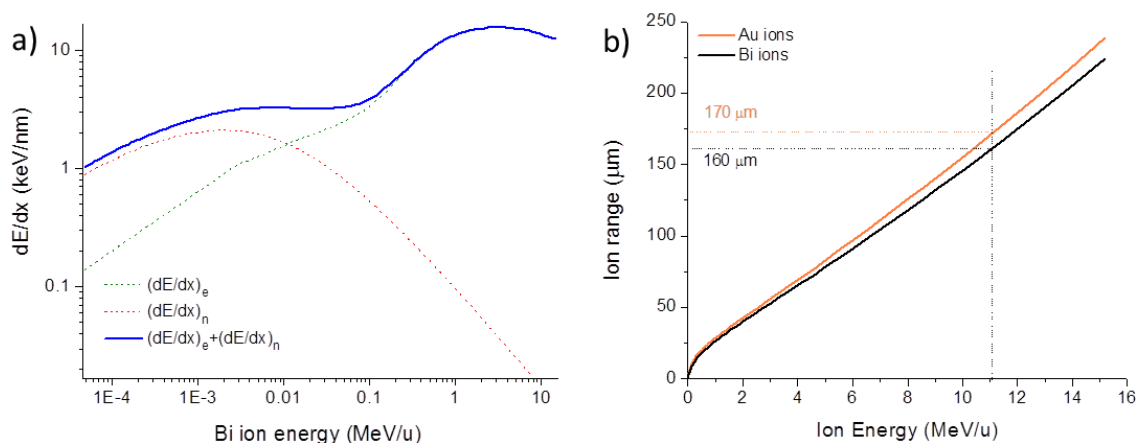


Figure 1: (a) Energy loss of Bi ions and (b) range of Au (orange) and Bi (black) ions in polycarbonate as a function of the specific ion energy according to the SRIM-2003 code simulation

The complete penetration depth (R_p) of the ion with initial energy E_0 can be determined from the following expression⁷³

$$R_p = \int_0^{E_0} \frac{dE}{(dE/dx)_e + (dE/dx)_n}, \quad \text{with } \frac{dE}{dE/dx}_e = \frac{E}{\rho} \frac{d\rho}{dE}, \quad \frac{dE}{dE/dx}_n = \frac{E}{\rho} \frac{d\rho}{dE} \quad (2)$$

where $(dE/dx)_e$ and $(dE/dx)_n$ are the electronic and nuclear energy losses per unit path length, respectively. The range of Au and Bi ions which were used in this work (polycarbonate foils calculated using the SRIM-2003 code) is presented in Figure 1b. The dashed lines correspond to the values of penetration range and energy of Bi (black) and Au (orange) ions, being 160 and 170 for Bi and Au ions with an energy of 1.1 MeV/u, respectively. Considering the penetration range of the ion, polymer foils have thicknesses of few tens m can be assembled in stacks so that several foils are irradiated in one step.

Depending on the ion energy and the charge state, the energy loss produces structural defects and compositional variations in the polymer. The damage formed along the trajectory of each incident ion is called latent track. Tracks have commonly a cylindrical geometry and a diameter between 5 and 10 nm depending on ion energy loss and target material. In polymer, the energy loss of heavy ions leads to the cleavage of the chemical bonds, amorphization and outgassing of small volatile fragments.^{74,75}

Schematic representation of the irradiation process is shown in Figure 2. The swift heavy ions used for irradiation at the UNILAC provide highly aligned parallel tracks. The beam incidence can be varied from normal to the sample surface down to grazing angles. In contrast to commercial track membranes, those fabricated at the GSI are characterized by a very small angular spread

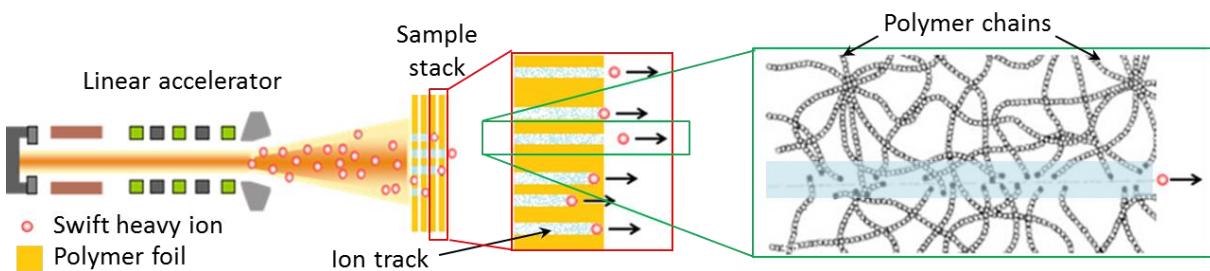


Figure 2 Schematic representation of the linear accelerator (UNILAC) at the GSI and irradiation process of a stack of polymer foils under normal incidence. The zoomed images show schematically a single track consisting of broken bonds of polymer chains (adapted from^{43,78}).

By means of chemical etching irradiated foils are converted to porous membranes selectively removing the damaged material and thereby turning each ion track into an individual open pore. Since each ion creates one track, the number of the pores in the membrane is equal to the ion fluence (number of ions per area). The size and homogeneity of the etched pores depend on the properties of the target material (e.g. density, composition, crystallinity), the energy loss of the ions, the etching time and etching solution. In addition, not

obtain pores with uniform diameter and well defined shape, the etching rate along the irradiated track (k_{track}) should be much higher than isotropic etching of the non-irradiated bulk material (k_{bulk}). The ratio $k_{\text{track}}/k_{\text{bulk}}$ will determine the opening angle of the pore. If $k_{\text{track}} \gg k_{\text{bulk}}$, the resulting pores have a cylindrical shape, whereas conical pores are achieved in the case of a smaller etching rate ratio. The fabrication of membranes with parallel cylindrical and conical pores as well as with interconnected pore networks are described in detail in Chapter 3. It is important to mention that prior to etching, both sides of all irradiated polymer foils used for experiments in this thesis are exposed to UV light in air. It is known that UV irradiation modifies the chain compounds inside the track without significant effects on the virgin PC thus improving the diffusion of the etching solution along the track. Besides, it triggers creation of new chain ends and acidic compounds which are highly sensitive to etchant. As a result UV treatment affects the etching rate and improves selectivity and the monodispersity of the nanopores.

1.2. Electrodeposition

The template method, and in particular electrodeposition in etched track membranes combines both top-down and bottom-up approaches and has demonstrated to be a very appropriate technique for the growth of nanostructures with small size and high surface volume ratio.²⁰²² It enables the synthesis of nanowires and tubes with simultaneous and excellent control over length and diameter. The template method has been demonstrated to be very suitable for the fabrication of metal and semimetal nanostructures with tuned composition, and crystallinity.²¹²³ Besides continuous single component wires, also segmented as well as multicomponent²³⁸² and alloy⁸³⁸⁴ structures can be fabricated.

Electrodeposition of microwires and nanowires is carried out using electrochemical cells consisting of two or three electrodes which are connected to a potentiostat for controlling and measuring the current and potential. The setup can be operated either potentiostatically (constant applied potential) or galvanostatically (constant applied current), as well as in pulsed electrodeposition conditions (pulsed applied potential). In this work, potentiostatic growth in a three-electrode configuration is applied. This method allows for a precise control of the composition of the deposit not only for one but also for multicomponent materials with a chosen stoichiometry.⁸⁴

The thermodynamic potential needed for the electrochemical reactions is determined by the Nernst equation, which describes the redox potential of a redox couple by the following equation:⁸⁵

$$E = E^{\circ} + \frac{RT}{nF} \ln \frac{a_{\text{ox}}}{a_{\text{red}}} \quad (3)$$

where E is the standard electrode potential of the redox couple with respect to the normal hydrogen electrode (NHE) and a_{ox} and a_{red} are the activities of the oxidized and reduced

species, respectively. R is the gas constant (8.3145 J/mol·K), T is the temperature, n is the number of electrons involved in the reaction, and F is the Faraday constant (96485 C/mol). Thermodynamically, when the potential applied to the working electrode is more negative than E^0 (in case of reduction), electrodeposition takes place and the ions in the electrolyte are reduced and may form a solid material on the working electrode.

In the simplest case of metals, electrodeposition is a process of reducing metal ions in an aqueous solution upon application of a potential. When the current flows from the counter electrode to the working electrode, the metal ions in the electrolyte travel to the working electrode and are reduced on the metallic substrate by capturing electrons. The corresponding reaction that takes place is as follows

$$(4)$$

The schematic of the electrochemical cell with the three electrodes (working, counter and reference) is connected to the potentiostat as shown in Figure 3. The membrane with sputtered and electrodeposited metal layers on one side always acted as a working electrode which was in contact with the copper ring of the cell. As the counter electrode a platinum wire and as a reference electrode Ag/AgCl (sat. KCl) were used. In this setup the potential is applied to the working electrode with respect to the reference electrode. The fixed potential of the Ag/AgCl reference electrode vs the standard hydrogen electrode at 25 °C allows reproducibility for all experiments.

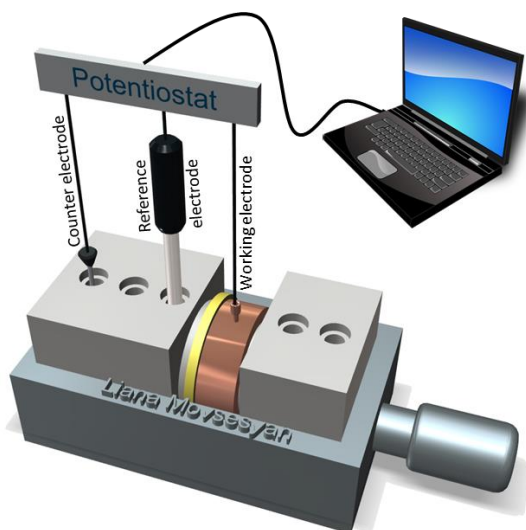


Figure 3: Schematic of electrochemical cell for nanowire growth by using three electrodes (working, counter, and reference) connected to a potentiostat, which is controlled via computer. The metallic layer sputtered and electrodeposited on one side of the membrane served as a working electrode.

The growth process was monitored and controlled by recording chronoamperometric vs. time curves during electrodeposition, which enabled us to monitor the different growth steps during the synthesis (Figure 4)

The charge and mass transfer of the deposited material are quantified with Faraday's law, which states that the mass of the deposited material is directly proportional to the amount of transferred charge

$$(5)$$

where i is the current passing through the circuit during the time between t_1 and t_2 , M and z are the molar mass and valence of the deposited atoms, respectively, and F is Faraday's constant. With this formula, the amount of deposited material can be calculated from the $i-t$ curves recorded during electrodeposition. Figure 4 presents a typical chronoamperometric curve for electrodeposition of ZnO in the cylindrical channels of a polycarbonate membrane with an average pore diameter of 250 nm and density of 10 pores/cm².

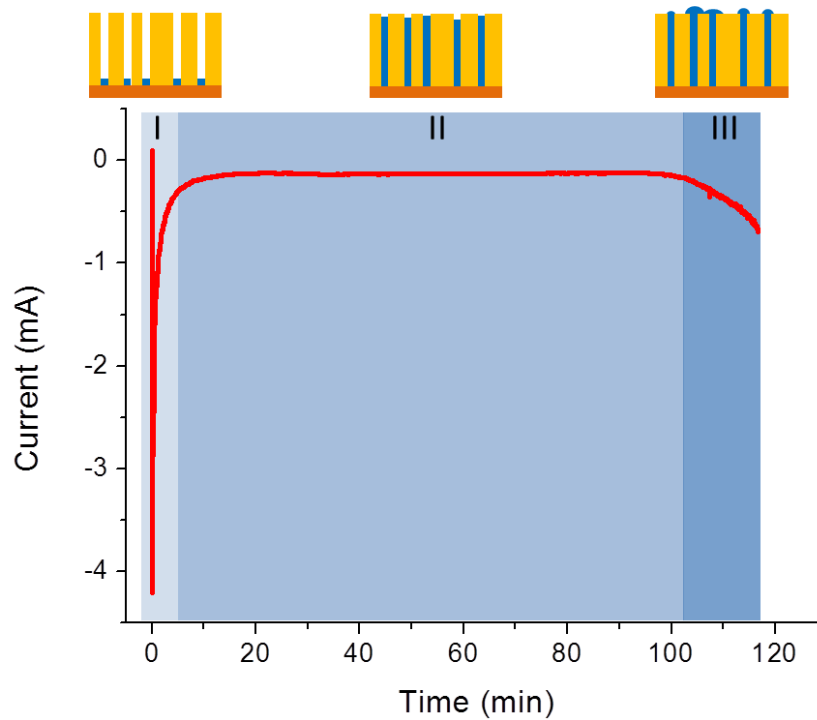


Figure 4: Representative chronoamperometric curve recorded during electrodeposition of ZnO nanowires, showing the dependence of the deposition current with respect to the time of three regimes of nanowire growth.

At the beginning of the deposition process, the current rapidly increases (as absolute value) and then decreases during the following minutes. This effect is attributed to the charging of the double layer (Helmholtz plane) and formation of the diffusion layer, as well as to nucleation processes. As the growth of nanowires inside the membrane continues (region II), the current remains almost constant. Finally, the pores are completely filled, called caps start to grow on top of the wires expanding on the surface of the membrane. This growth is indicated by an increase in current due to the increased effective area where the

growth takes place in region III.⁸⁷ By following this current behavior during nanowire growth, the deposition can be stopped at a defined time period, e.g. to obtain nanowires of a certain length.

In the case of multicomponent materials, such as metal oxides, growth takes place in more than one step depending on the electrolyte composition. For the synthesis of metal oxides, electrodeposition from nitrate-based solutions is one of the most common techniques. The driving force in this process is the nitrate reduction which leads to a local pH increase in the electrolyte due to formation of OH^- ions. In this work, an aqueous electrolyte of zinc nitrate hexahydrate ($\text{Zn}(\text{NO}_3)_2 \cdot 6\text{H}_2\text{O}$) was used for the growth of ZnO nanowires which takes place in several steps. First, upon application of the potential, hydroxyl ions are formed at the cathode/electrode surface according to reaction (6) in the presence of Zn^{2+} ions in the solution hydroxylation reaction takes place $\text{Zn}(\text{OH})_2$ (reaction 7). If the electrolyte is heated, elevated temperature $\text{Zn}(\text{OH})_2$ is dehydrated thus resulting in the formation of fully crystalline ZnO according to reaction 8. As mentioned before, the local pH in the bath close to the electrode as well as in the pores is increased due to the formation of OH^- ions, leading to the preferential growth of ZnO inside the pores of the membrane. Depending on the ratio of the produced OH^- and Zn^{2+} ions and the supersaturation in the bath, the crystal growth will behave differently to different crystal orientations. Therefore, the crystallinity depends on the concentration of ions^{39,55,88}



Previous studies reported the electrodeposition of ZnO nanostructures from $\text{Zn}(\text{NO}_3)_2$ with pH values adjusted between 7 and 11 by adding NaOH to the electrolyte. To avoid degradation of the polymer by high pH electrolytes during wire growth, an as-prepared electrolyte with pH 5 was used in this work. The [f c k h \ ' d f c W Y g g \ ' h c c \ _ \ ' d \ ' U W Y] for parallel arrays and wire networks, respectively.

1.3. Structural and physical properties of ZnO

During the past few years, the research activities on zinc oxide (ZnO) have significantly increased. The history of the research on ZnO goes back to 1930s reaching its peak in the late 1960s due to the availability of single crystalline bulk ZnO produced by chemical vapor deposition (CVD).^{92,93} [\ ' h \ c i [\ ' N b C \ '] g \ ' h e r e \ ' a r e \ ' s t i l l \ ' m e r o u s \ ' o p e n \ ' Y f \] U \ ' z \ '] there are still numerous open questions about the structural and physical properties of this material. Particularly, nanoscale 1D structures, such as nanowires, nanobelts, nanoflowers, nanoribbons, nanorods, nanowalls, and nanotubes, have been drastically attracted the attention of scientists due to their promising application in technology.²³

1.3.1. Crystal structure

ZnO can crystallize in three possible polymorphs: wurtzite, rocksalt, and zinc blende. Thermodynamically, the most stable phase is the wurtzite crystal structure, where each Zn atom is surrounded by a tetrahedron of four oxygen atoms, and vice versa. The wurtzite structure has a hexagonal unit cell with two lattice constants: $a = 0.325 \text{ nm}$ and $c = 0.52 \text{ nm}$ at ambient conditions, and belongs to the $P6_3mc$ space group.⁹⁴ The structure consists of interpenetrating hexagonal close-packed (hcp) layers of zinc and oxygen, displaced with respect to each other along the c -axis.⁹⁴ The schematic representation of the ZnO wurtzite lattice with the primitive cell is shown in Figure 5a. The crystallographic orientations of the a - and m -planes are highlighted in Figure 5b. The directions and planes for hexagonal structures are indexed either with three digit Miller indices (hkl) or four digit Bravais indices $(hkil)$. For ZnO, it is more common to use the four axes, a_1 , a_2 , a_3 , and c , and therefore four indices, where h , k and i are related as follows: $h + k + i = 0$. This relation allows the transformation of Miller to Bravais indices, and vice versa. The c -axis is always referred to as the z -direction, and the plane perpendicular to this axis is the hexagonal xy -plane. The latter are the most commonly observed facets and the main polar surfaces in wurtzite ZnO, arising from the strong bond polarity of Zn^{2+} and O^{2-} ions being either zinc or oxygen terminated. Other polar surfaces also often observed in wurtzite ZnO are $\{10\bar{1}0\}$ and $\{11\bar{2}0\}$, which are non-polar surfaces due to the equal amount of Zn and O

23,27,496

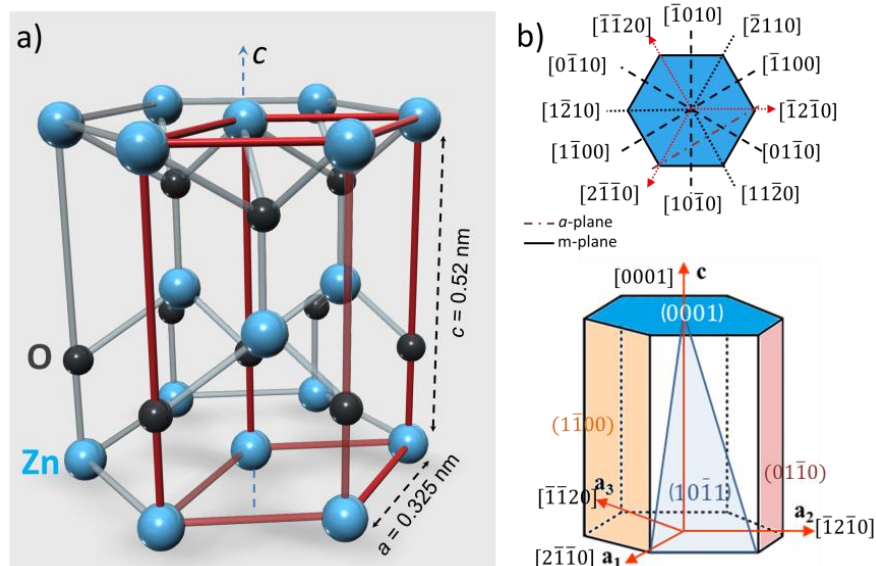


Figure 5: a) Schematic representation of the wurtzite ZnO with a primitive cell b) crystallographic orientations of planes that are commonly present in the wurtzite phase.

1.3.2. Band structure

ZnO is a III-VI semiconductor with a wide band gap of $3.37 \pm 0.01 \text{ eV}$ at room temperature, which is in the near UV spectral range.⁹⁴ The first theoretical and experimental

studies of the electronic band structure of ZnO in the late 1960s and 1970s^{95,97,98} Energy bands of hexagonal ZnO are shown in Figure 6. Both the valence band (VB) maximum and the conduction band (CB) minimum are positioned at the same $k = 0$ wave vector, indicating that ZnO has a direct band gap. Several theoretical and experimental works have shown the presence of bands in ZnO at around 6 eV below the VB, which correspond to Zn orbitals. Due to the significant overlap of d orbitals, Zn has broader bands than any other III-VI compound.⁹⁷ The states closer to the VB maximum correspond to d orbitals, whereas the s bands are situated far below the VB (20 ~ eV). The CB is formed mainly by the empty Zn s^{99,100} The bond in wurtzite ZnO has a³ covalent nature.

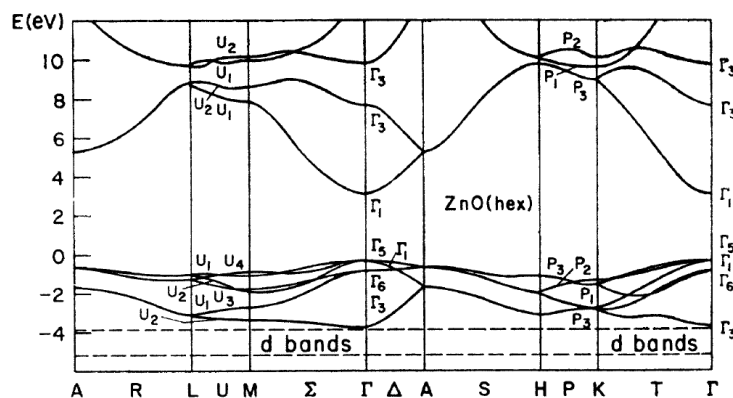


Figure 6: Energy band of hexagonal ZnO according to Rössler (1969)⁹⁷

Among all III-VI compounds, ZnO has the largest excitation binding energy, of 60 meV^{21,22} which makes ZnO a very interesting material for photonic devices due to its broad emission band.

1.3.3. Electrical properties

Both theoretical and experimental studies on the electrical properties of ZnO films and nanostructures have been reported for several decades. Because of the presence of oxygen vacancies in the structure, normally undoped ZnO has intrinsic n-type conductivity. The more oxygen vacancies are present, the higher is the electron density. As a result, ZnO is a III-VI semiconductor with a very high electron mobility ($\sim 200 \text{ cm}^2 \text{ V}^{-1} \text{ s}^{-1}$ at 300 K, $\sim 2000 \text{ cm}^2 \text{ V}^{-1} \text{ s}^{-1}$ at 50 K),¹⁰¹ which is expected to improve the performance of electronic devices based on this material. A higher electron Hall mobility was reported in studies of ZnO/MgZnO heterostructures reaching up to $5500 \text{ cm}^2 \text{ V}^{-1} \text{ s}^{-1}$.¹⁰² For transparent conductive oxide devices, ZnO is often doped with group III metals like Al, Ga, and In, which enhances the n-type conductivity of ZnO.^{103,105} For a long time, intensive efforts have been put in research on the synthesis of p-type ZnO, which is one of the main challenges of this material. p-ZnO is mainly obtained by doping with phosphorus or nitrogen.¹⁰⁶ Despite the vast number of reports, the fabrication of p-type ZnO is hardly reproducible.

1.4. Photoelectrochemical water splitting

One of the most important but challenging technological issues of the century is the shift from fossil fuels to renewable energy sources, such as wind power, solar energy, and biofuels. The main problem related to the use of fossil fuels such as coal, natural gas and oil products is the release of CO₂ into the atmosphere and the limited and quickly diminishing amount of fossil fuel sources. Renewable energy sources have a potential to substitute fossil fuels and serve as a sustainable energy source providing a clean environment. Large scale research has been performed and is ongoing worldwide in search of environmentally friendly energy sources. In 1883, the first solar cell based on selenium was made by Charles Fritts. However, this solar cell did not have a large scale use because of the sunlight to electricity conversion efficiency less than one percent. In 1954, the first practical Si-based solar cell was demonstrated at the Bell laboratories by Daryl Chapin, Gerald Pearson and Calvin Fuller with an efficiency of about six percent. This was the highest reported value at that time. Efforts to produce photovoltaic devices with high efficiency still continue at present.

A new approach to obtain a clean, cost-efficient and domestically produced energy source was proposed by Akiyama Fujishima and Kenichi Honda in 1972. They demonstrated the first successful experiment of assisted water splitting using an n-type TiO₂ photoanode connected with a platinum black electrode in a photoelectrochemical (PEC) cell for hydrogen production as a renewable energy source. Then, many efforts have been devoted to this research field. More efficient water splitting systems have been obtained by combining several materials such as a tandem cell, adding co-catalysts and applying different configurations of PEC cells.^{110,113} Albeit increasing the efficiency of both photocurrent conversion and generation and collection of hydrogen remain challenging, light-driven PEC water splitting for hydrogen production is one of the most promising and dominating fields of research today.

The principle of the PEC cell is based on the physics of semiconductor photoaction. Important parameters to be considered during the choice of the materials are

- ◁ the band gap of the semiconductor to be small enough to absorb light in relatively wide range of the solar spectrum
- ◁ the position of the CB minimum and VB maximum with respect to the hydrogen and oxygen redox potentials for efficient hydrogen and oxygen evolution reaction (HER and OER, respectively), i.e. the CB minimum must be higher in energy than the standard redox potential of H⁺/H₂ couple, and the VB maximum must be lower than the standard redox potential of the O₂/O couple
- ◁ the stability against (photo)electrochemical corrosion in aqueous electrolytes,

- efficient separation and transfer of minority charge carriers from the core of the photoelectrode to the semiconductor/electrolyte interface and the majority charge carriers to the counter electrode, with minimum recombination

A vast variety of single- and multicomponent materials, such as Al_2O_3 , TiO_2 , Cu_2O , Fe_2O_3 , WO_3 , GaP , GaN , Si , CdS , CdSe , BiVO_4 , NaTaO_3 , La and many others have been studied.^{11, 118} The standard redox potential of the $\text{O}/\text{H}_2\text{O}$ couple is 1.23 V versus the reversible hydrogen electrode (RHE), which means that the band gap of the photoelectrode material must be larger than this thermodynamic minimum value of potential for splitting the water. The positions of several common semiconductors respect to the redox potentials for water splitting are shown in Figure 7a.

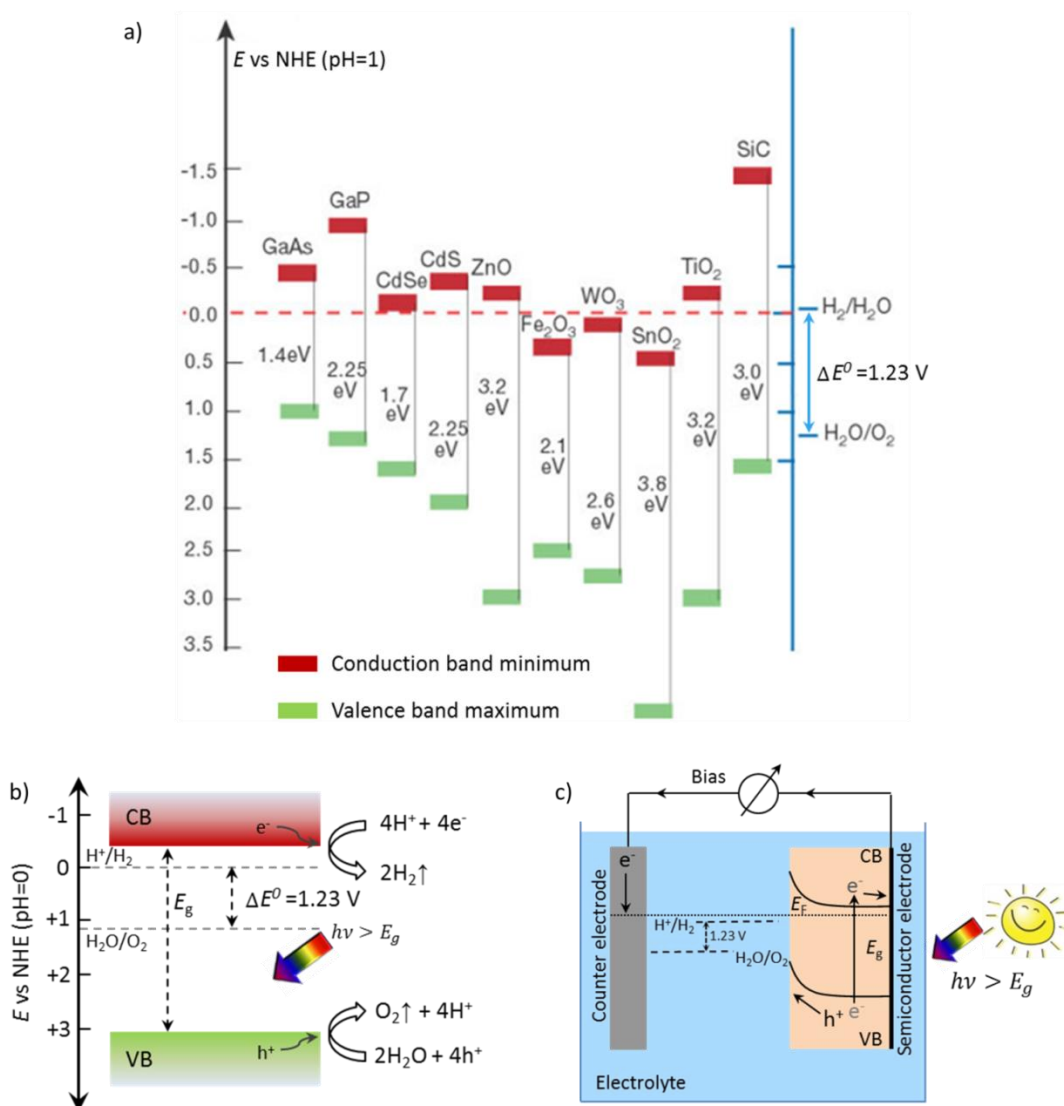


Figure 7a) Relation between the band position of different semiconductors and redox potentials for water splitting (adapted from [118]), b) schematic representation of the band structure of ZnO under illumination together with hydrogen and oxygen evolution reactions, c) schematic of a PEC cell with a photoanode and metallic counter electrode

The basic principle of the overall water splitting process is schematically shown in Figure 1. When a semiconductor photoelectrode is illuminated with absorbed photons having energy greater than the band gap energy, electrons are excited into the CB thus forming electrons, which are separated by the formed electric field in the depletion layer. If the semiconductor is immersed into water-based electrolyte, the holes from the VB will drive the OER producing oxygen gas and electrons from the CB will lead to the formation of hydrogen by the HER according to the following reactions:



The semiconductor serves as a photon-DEC cell if it has n-type conductivity (electrons are the majority charge carriers) a photocathode if the conductor type (holes are the majority charge carriers). The schematic of a simple PEC with an n-type photoanode like ZnO, is shown in Figure 2. The cell consists of the semiconductor photoelectrode (working electrode), a metal counter electrode (typically Pt), and a reference electrode required to control the potential of the working electrode. If a bias is applied, the photogenerated electrons and holes will separate. The holes will travel to the surface of the n-type semiconductor, where the OER will take place at the electrode/electrolyte interface and electrons will travel through the external circuit to the counter electrode driving the HER.¹¹⁸ It is common to use Ag/AgCl reference electrode for measurements, whereas for data analysis and for ease of comparison with other systems reported in literature, the Nernst equations used to convert the potentials reversible hydrogen electrode (RHE) (

$$E_{\text{RHE}} = E_{\text{Ag/AgCl}} + 0.059 \text{ V} \cdot \text{pH} \quad (11)$$

where E_{RHE} is the converted potential vs. RHE, $E_{\text{Ag/AgCl}}$ is the potential applied to the Ag/AgCl (sat. KCl) reference electrode used, and $E^0 = 0.197 \text{ V}$ is the standard potential of a Ag/AgCl reference electrode⁸⁶ at 25

To improve the efficiency of PEC cells, the possible recombination of photogenerated charge carriers traveling to the semiconductor surface or counter electrode should be minimized. For this, nanowire-based photoelectrodes are of interest due to their one-dimensional shape and geometrical orientation which provide higher light absorption and more efficient charge carrier separation and transport to the surface electrodes as compared to bulk materials.^{120,122} The reduced nanowire diameter and large surface area of the photoelectrode/electrolyte interface facilitate the rapid transport of photogenerated charge carriers to the wire surface and faster redox reactions, respectively. For example, the diffusion length of bulk ZnO at 25°C is ~440 nm which increases with higher temperature.¹²³ If a film photoelectrode is much thicker than the diffusion length of the minority charge carriers, in this case holes (h⁺), not all holes (especially the ones generated in deeper layers of

semiconductor) will reach the film (Figure 8a). In contrast to this, for the more available surface area of nanowires, the holes will have a shorter path to quickly diffuse to the electrode/electrolyte interface, thereby reaching the substrate and flow to the external circuit (Figure 8b). Hence charge transport limitations can be circumvented by means of adjustment of nanowire diameter. However, enhanced light absorption is expected for nanowires compared to films so extensive light scattering.¹²⁴ The reflected light from one wire can be absorbed by the neighboring wire, and if the photon energy is larger than the band gap energy of the material, the reflected light can also excite electrons into the CB. For this approach, a nanowire geometry might be beneficial. Also, a composite structure with wide and narrow band gap materials is of interest. The photons which are not absorbed by the wide band gap material, those that are reflected at the surface can excite charge carriers in the narrow band gap material. Another important parameter that should be considered during the material choice is the optical thickness, where L_p is the absorption coefficient. For more efficient devices, the light penetration depth should be comparable with dimensions of the photoelectrode, e.g. film thickness or nanowire diameter.

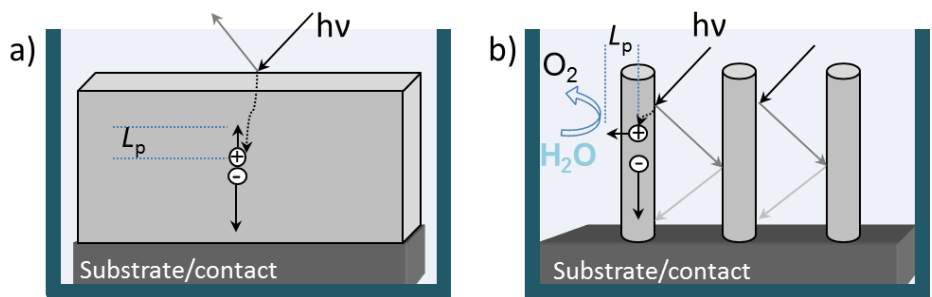


Figure 8: Schematic representation of photoanodes showing long and short path lengths for photogenerated holes to the electrode surface: a) film and b) nanowire array, L_p is the diffusion length to the hole.

One further route to successful transport and collection of photogenerated charges is the use of photoelectrodes with high crystallinity. Electron-hole recombination is less likely to occur in single crystalline structures, whereas the grain boundaries in materials with poor crystallinity are limiting aspects because they serve as traps and recombination centers for electrons and holes.^{11,41,24}

Last but not least, the lifetime of the photoelectrodes should be mentioned. Even if the band position of the semiconductor perfectly matches the OER and HER potential, the photoanode (electro)chemical corrosion should be taken into account. This is probably the most severe limitation for the choice of photoelectrode material. For most non-oxide materials, decomposition or oxidation of the surface is typical, while for oxide materials, the thermodynamic stability is accompanied with the oxidization.¹²⁴ In particular, ZnO tends to decompose in aqueous solution under illumination following the reaction below.^{11,41,25,26}

Fortunately, there are several simple oxide semiconductors such as TiO₂ or SnO₂ which have excellent stability against chemical and photo corrosion in a wide range of pH values of electrolyte. Coating other photoactive electrodes with these materials can help to extend the lifetime of the device. In this work, ZnO photoanodes were coated with TiO₂ layers of different thicknesses by atomic layer deposition (ALD). The protective role of the TiO₂ layer during PEC measurements is discussed in Chapter 6.

1.5. Metal-semiconductor contact

To describe metal-semiconductor contacts, band diagrams are usually built to visualize alignment of the bands at the interface of two materials. This section introduces several characteristic parameters for semiconductors to describe the band diagrams.

A schematic of the band of a metal and a semiconductor (e.g. ZnO, TiO₂) before and after bringing them into contact are shown in Figure 9 (a) and (b) respectively. The band structure of the metal is characterized by work function ϕ_m . On the diagram, ϕ_m is the distance between the Fermi level (the highest occupied electron energy level at absolute zero temperature) of the metal and the vacuum level E_{vac} and represents the amount of the energy that is required to transport an electron from the Fermi level to the vacuum level. The characteristic parameters shown on the diagram for a semiconductor are the following:

- < band gap E_g - distance between the minimum of the conduction band (E_c) and the maximum of the valence band (E_v),
- < work function W_{sc} - the distance of the Fermi level (E_F) from the vacuum level,
- < ionization energy I_{sc} - the distance of the valence band maximum from the vacuum level.

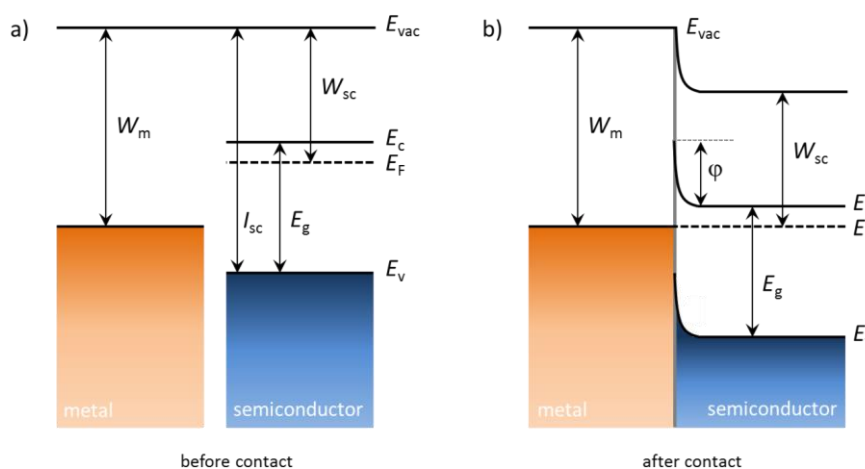


Figure 9 Energy bands for a metal and a semiconductor (a) before and (b) after bringing into contact. The Fermi level of the metal is lower than that of the semiconductor, i.e.

Figure 9 shows the case of type I semiconductor-metal contact without a bias for which $W_{sc} < W_m$, as for ZnO/Au or TiO₂-Au contacts discussed in detail in Section 6.3. When the two materials are brought into a contact, electrons start to flow from the semiconductor to the metal and vice versa. For the condition $W_m < W_{sc}$, the metal becomes negatively charged. This process will continue until the system reaches the thermodynamic equilibrium, i.e. the Fermi energies are equal (Figure 9b) and the diffusion currents of the electrons flowing in both directions will be identical. The height of the potential barrier, which is formed at the interface of the two materials due to band bending for electrons flowing from the semiconductor to the metal defined by their work functions as $\phi^b = W_m - W_{sc}$. This potential difference is denoted as contact potential, and the barrier height for the mentioned conditions is known as Schottky barrier and Schottky contact, respectively.

By means of e.g. X-ray or ultraviolet photoelectron spectroscopy (XPS or UPS), the work function and the distance of the valence band from the Fermi level can be determined. The band gap of the semiconductor is measured using ultraviolet visible (UV-Vis) light spectroscopy. These three parameters provide information about the positions E_c , E_f , and E_v versus the vacuum level. Examples of band alignment based on XPS and UPS measurements for TiO₂ and Au-ZnO are shown in Section 6.3.

2. Methods and sample preparation for characterization

In this chapter, the characterization methods are presented. The morphology, crystallinity and composition of nanowire-based structures are analysed using high resolution scanning electron microscopy (HRSEM), energy dispersive X-ray spectroscopy (EDX), X-ray diffraction (XRD), high resolution transmission electron microscopy (HRTEM) with high-angle annular dark field imaging (HAADF), selective area electron diffraction (SAED), electron energy loss spectroscopy (EELS) and X-ray photoelectron spectroscopy (XPS). The general process parameters used for atomic layer deposition (ALD) and photoelectrochemical (PEC) measurements are described.

2. Sample preparation and characterization methods

2.1. High resolution scanning electron microscopy (SEM)

Scanning electron microscopy (SEM) is a widely used technique for characterization of the morphology of nanomaterials and nanostructures. It uses a focused beam of accelerated electrons to scan the surface of the specimen to obtain a raster image. As an electron hits the surface of the sample, a number of interactions occur between the beam electrons and the atoms of the specimen resulting in emission of different types of electrons (secondary, backscattered, Auger) and X-rays (Bremsstrahlung, characteristic). By collecting the emitted secondary electrons on a cathode ray tube, a topographic image of the specimen is obtained. Collection of backscattered electrons from deeper levels of the sample allows for contrast imaging of multicomponent structures where the atomic numbers of components differ widely.

In this study, a high resolution scanning electron microscope (HRSEM, JEOL JSM7401F) equipped with two secondary electron detectors at different positions with respect to the sample stage was used to image the fabricated membranes and nanostructures.

Prior to the SEM analysis, the polymer membranes were sputtered with a 8 nm thick Au layer (20 s) using an Edwards Sputter Coater S150B, by applying a pressure of 10⁻¹ Torr and a potential of 115 kV resulting in a current varying between 15 and 30 mA. The sputtered conductive layer the charging effect for SEM were avoided. The microscope was operated at an accelerating voltage of 40 kV in SEM mode. The topography and the pore size were analyzed with low secondary electron imaging (LEI) at a working distance of 8 mm.

To investigate the pore geometry inside the carbonate membranes produced by heavy ion irradiation and subsequent chemical etching, the cross section of the membranes was imaged. The samples were prepared in collaboration with Loïc Burr (Materials Research department, GS) by irradiating pre-etched membranes with high fluence of 5 × 10¹⁰ ions/cm² using Au ions with energy of 5.6 MeV/u followed by a 24 h UV treatment on each side of the samples. Due to the severe beam induced embrittlement, the membranes easily break in liquid nitrogen which allows for imaging the cross section of the membrane. Alternatively, the embrittlement of the polycarbonate membranes was obtained by immersing the samples in Aqua Regia solution for ~2 month at room temperature. More details about this process can be found in the doctoral thesis of Loïc Burr.¹²⁸ After breaking the membranes, the samples were glued onto a specially designed SEM sample holder (UWIhcz - \$õh c' section). Prior to the SEM analysis the samples were coated with Au, as described above. For these samples SEM was operated at 10 kV with LEI detector.

For SEM investigation of the nanowire and network, the polymer membranes were dissolved in dichloromethane (CH₂Cl₂, for analysis, Merck) in several steps. The nanowire arrays/networks embedded in the polymer membranes were placed horizontally in sample

holders in such a way, that the edges were fixed by folding of the sample which can cause damage to the wires. SiO_2 was dropped continuously on top of the samples. The level of dichloromethane (with polymer residues) raised the sample holder but did not cover the sample. If the solution covered the sample, it might contaminate the surface of the sample with the dissolved polymer residues. A continuous flow of CH_2 was found to be an important step. If the sample with partially dissolved polymer was exposed to air for a relatively long time (a minute or more), it seemed to harden resulting in broken wires. After repeating this step, the samples were immersed in fresh CH_2Cl_2 bath and left for 1h. This last step was repeated three to four times. Finally, the free standing nanowire arrays and 3D nanowire networks with the metallic electrode were dried in air and inspected by SEM. Both ZnO and ZnO/TiO₂ nanowire arrays, networks and films were characterized by using SEM in gentle beam mode (GBow) with an upper secondary electron detector (SEI) at 2 kV accelerating voltage at a distance of 8 mm.

For nanowire diameter and length analysis, single nanowires were transferred onto Si wafer pre-cleaned with acetone and deionized water. The following two methods were applied: (i) after dissolution of the membrane, some of the wires were detached from the electrode by exposing the samples immersed in CH_2Cl_2 to an ultrasonic bath (Elma, Transsonic T460/H) for a few seconds. The released nanowires were then transferred to a Si wafer by drop casting the nanowire- CH_2Cl_2 mixture. (ii) The wires still embedded in the membrane were immersed in dichloromethane in a centrifuge tube. After an ultrasonic treatment for 150 s, the tube was centrifuged three to five times at 4000 rpm for 1 min using Heraeus Biofuge primo R Centrifuge. In between these steps, the dichloromethane bath was replaced with a fresh one. Before each step of centrifugation, the nanowires with the fresh dichloromethane were mixed on a shaker for 20 min to disperse the wires in the solution for better cleaning. Finally, the solution containing the wires was casted onto Si wafers. The samples were analyzed by operating the SEM at the same conditions as for nanowire arrays and networks attached to the substrates.

Core-shell nanowires and small pieces of nanowire networks were transferred onto TEM grids (Plano GmbH) by drop casting the wires with CH_2Cl_2 onto the grids. To analyze the samples in transmission electron microscopy (TEM), 10 kV accelerating voltage was applied. The wires were imaged with LEI detector at a working distance of 8 mm. To study the dispersity of the nanowires, which were transferred onto TEM grids by the grid on the surface of the network, GB-Low mode at 2 kV and probe current at a distance of 8 mm was used.

2.2. Energy dispersive X-ray spectroscopy (EDX)

Characteristic X-ray emitted from the sample depend on the atomic number of element and the structure and are mainly used for quantitative and qualitative analysis.

The composition of the nanowire arrays, networks and single wires was studied by energy dispersive X-ray spectroscopy (Bruker) in the SEM. Point spectra and scans were recorded by applying an accelerating voltage of 10 or 20 kV and a probe current of 10 depending on the amount of material, at a fixed distance of 8. The acquisition time was 8-min for multipoint scan and 10 min for line scan. The analysis of the spectra was done by using the Quantax software from Bruker.

2.3. X-ray diffraction (XRD)

XRD is a nondestructive technique that uses a collimated beam of X-rays to investigate the arrangement of atoms within a crystal. When a beam strikes the sample it diffracts in different directions from the atoms of crystal planes. If the wavelength λ of the incident radiation equals the crystal lattice spacing d , constructive interference is produced. The diffracted rays can be detected. The resulting diffractogram provides information about crystallographic orientation and lattice parameters of the crystal, defects, stresses, etc.

The crystallographic structure of the cylindrical and conical nanowire arrays still embedded in the membrane was analyzed by using a diffractometer (XRD) (Difert X-Ray generator, HZG-4 goniometer in Bragg-Brentano geometry) with a generator voltage of 40 kV and current of 30 mA using $\text{Cu K}\alpha$ ($\lambda = 1.54056 \text{ \AA}$). The device was operated by the θ - 2θ scan mode. The XRD patterns of networks after dissolution of the membrane were recorded with a D2 PHASER diffractometer (Bruker), which was operated at a generator voltage of 30 kV and current of 10 mA. With this device the scan rate and integration time were $2^\circ/\text{min}$ and 10 s , respectively. The data were analyzed by using the X'Pert software.

2.4. High resolution transmission electron microscopy (HRTEM)

Transmission electron microscopy (TEM) is one of the techniques allowing for analysis of material structure on an atomic scale. It enables the analysis of the crystal structure, chemical composition and contaminations through diffraction pattern and electron energy loss analysis. In TEM accelerated electrons are projected onto a thin specimen and penetrate the sample undergoing either elastic or inelastic scattering with its atoms. The transmitted electrons are used to build a high resolution TEM image and/or selected area electron diffraction (SAED) pattern. Inelastic scattered electrons of low energy are detected by a high-angle annular dark field (HAADF) detector for mass contrast imaging and/or by a spectrometer for electron energy loss spectroscopy (EELS) allowing for chemical mapping and composition analysis.

To analyze the crystallinity and purity of ZnO and ZnO/ZnS as well as the homogeneity and phase of TiO₂ layers coated on top of ZnO wires by atomic layer deposition

(ALD), the wires from arrays and networks were transferred to Ted Morgan as explained in Appendix E. In collaboration with Dr. Wilfried Sigle from the MPI for Solid State Research in Stuttgart the wires were inspected by using high resolution transmission electron microscope (HRTEM, JEOL 200CF) together with high angle annular dark field (HAADF) imaging and electron energy loss spectroscopy. Selected area electron diffraction was used for analysis of crystallographic structure of the wires in situ. The device was operated at an accelerating voltage of 200 kV and a current of 15 μ A.

2.5. Photoelectrochemical (PEC) measurements

The photoelectrochemical (PEC) measurements presented in the thesis were performed at the GSI in Darmstadt and University of Twente (The Netherlands) group of Prof. Dr. Guido Mul

The setup at the GSI consisted of a LS108 solar simulator from LOT Quantum Design GmbH (AM 1.5G) a Reference 600 potentiostat (GAMRY Instrument) and a PECC-2 photoelectrochemical cell (ZAHNER Elektrik GmbH & Co. KG) with an Oring defining the photoactive area of the sample.

For the PEC measurements at the University of Twente a setup consisting of a 300 W Xe lamp with AM 1.5 filter (Newport corporation), a potentiostat (VERSASTAT4, Pine Applied Research), and a PEC photoelectrochemical cell (ZAHNER Elektrik GmbH & Co. KG) with a 7 mm O-ring were used.

All measurements were performed in 0.1 M K_2SO_4 (Sigma Aldrich) aqueous solution with a pH of 5.6. The distance of the PEC cell was calibrated with a Si solar cell (Newport Oriel, P/N 91150V) to obtain an illumination of 1 sun on the sample.

2.6. X-ray photoelectron spectroscopy (XPS)

X-ray photoelectron spectroscopy (XPS) is a surface sensitive technique for analysis of chemical composition and electronic states of a material within a depth of ~10 nm on the surface of a specimen. When an incident photon ($h\nu$) hits the surface of the sample with energy higher than the ionization energy of the electrons, they are ejected from the sample. The kinetic energy (E_{kin}) of the released electrons can be detected by a photoelectron spectrometer. It is related to incident photon energy by $E_{kin} = h\nu - (E_b + \phi)$, where E_b is the binding energy required to transfer the excited electron to the Fermi level and ϕ is the work function of the spectrometer. A spectrum revealing the number of ejected electrons vs energy provides information about the energy levels of the inner electron shells of the specimen atoms.

XPS was applied to analyze the surface of nanowire networks and/or corrosion of the surface after PEC measurements as well as to estimate possible contaminations on the wires (e.g. residues from polymer or dichloromethane) which might

affected the PEC performance. XPS was also used to determine the work function and the valence band positions for visualization of the band alignment of Au/TiO₂ Schottky contacts. The measurements were performed at the DAISY 8.5 f a g h U X h D g Integrated System for Fundamental research) of the Surface Science Program of Prof. Dr. Wolfram Jaegermann at the TU Darmstadt in collaboration with Dr. Florent Yang. The spectra were recorded by using a PHOIBOS 225 (Specs GmbH) analyzer and a c b c W \ f c a U h] W ' 5 ` ' ? ' ' f U X] U h] c b ' k] h \ ' Y I W] h U h] measurement, the system was calibrated with a high purity Ag sample (freshly sputter cleaned under Ar atmosphere) with a very high purity to calibrate the Fermi level. For determination of the work function, a negative bias of 3 V was applied between the analyzer and the sample for distinguishing the signal from the sample.

3. Fabrication of etched ion track membranes

Ion irradiation and etching processes required for the fabrication of etched ion track membranes are described in this chapter. Three main geometries are discussed: aligned cylindrical and conical channels as well as interconnected channel networks. Superstructures consisting of both vertically and horizontally interconnected channels are introduced.

3. Fabrication of etched ion-track membranes

Etched ion track membranes were prepared by etching of irradiated foils. During this process the damaged material in the tracks is selectively removed converting the ion track into channels (pores). By adjusting the fluence (number of ions per area) the number of pores in the membrane can be controlled. Each ion passing through the polymer foils creates one track. Using different irradiation and etching conditions (e.g. concentration of the etchant, temperature and etching time and setup configuration), polycarbonate membranes were fabricated with parallel cylindrical, parallel conical and interconnected cylindrical nanochannels (Figure 10). Irradiation and etching conditions employed for the fabrication of these three types of templates are presented in the following section

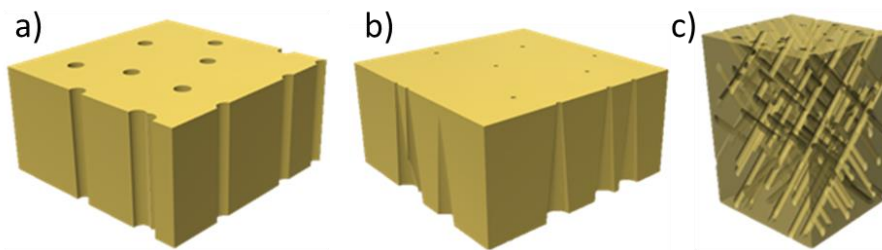


Figure 10 Schematic representations of membranes with a) parallel cylindrical, b) conical interconnected cylindrical pores

3.1. Parallel cylindrical pores by symmetric etching

Polycarbonate (PC) foils with thickness of 30 μm (Makrofol N, Bayer AG) were irradiated with ~ 2 GeV Au and Bi ions at the X0-beamline of the universal linear accelerator (UNILAC) at GSI. In order to fabricate membranes with parallel nanochannels, the irradiation was performed under normal beam incidence (perpendicular to the foil surface) typically applying a fluence of 10^{19} ions/ cm^2 . Prior to etching, both sides of the irradiated polymer foils were exposed to UV light (30 W, 312 nm, Vilber Lourmat) in air to improve the homogeneity of the pore diameter distribution over the whole sample.^{81,29} By immersing the irradiated foils in 6M sodium hydroxide (NaOH, Sigma Aldrich, > 97 %) solution at 75°C the tracks were selectively dissolved and converted into cylindrical channels. Given by the general etching of the bulk polymer the total thickness of the membrane slightly increases (Figure 1a).⁷⁶ Symmetric etching was performed in a double-walled cylindrical pot connected to a heating water (Figure 1b). In this configuration the etching solution had an access to the tracks from both sides of the irradiated foils to improve the convection and to keep the bath temperature constant, solution was stirred at 250 rpm. To produce multiple membranes with identical pore diameter, four samples were etched at the same time. Various etching times were employed between 1.5 and 108 min. The schematic of the evaluation of the track and the channel opening with the increase of time are shown in Figure 1c. Under these etching conditions, the pore diameter increased linearly with etching time. However, the etching rate varied depending on the aging of the

polymers, i.e. the time between irradiation and etching processes. Longer aging periods led always to higher etching rates. The values usually varied between 20 and 30 nm/min. After etching the membranes were rinsed with deionized water by immersion in multiple water baths and finally dried in air.

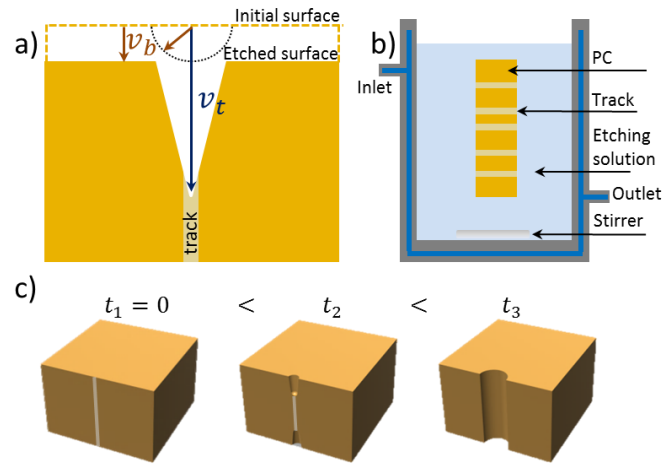


Figure 11: Schematic representation of a) etching of a track, b) thermostated pot for asymmetric etching, and c) nanochannel formation for different etching times

Pore size and size distribution were analyzed by SEM. For membranes etched without UV treatment an inhomogeneous size distribution of the pores was observed (Figure 12a). Areas marked with red and orange in Figure 12a show smaller and larger pores with average diameters of 1702 and 35074 nm, respectively, as compared to the mean diameter of the majority of the pores being 300 nm. A pre-sensitization step with 1h UV light on each side of the irradiated foils before etching yielded a more homogeneous etching and size distribution (Figure 12b). The average pore diameter of this sample was 220

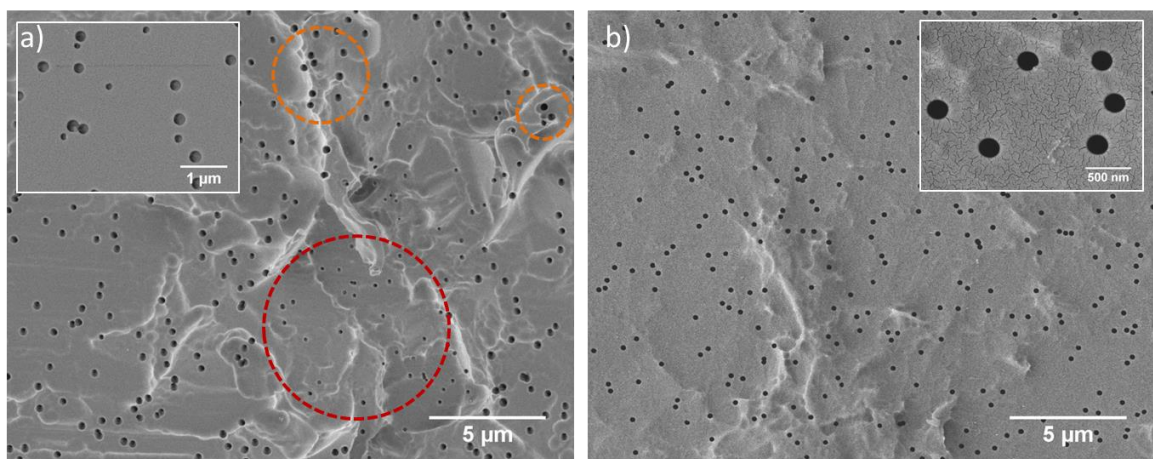


Figure 12: Representative SEM images of the surface of track membranes etched under identical conditions a) without and b) with a pre-sensitization step showing a broad (a) and a uniform (b) distribution of the pore diameters.

Figure 13 shows the average pore diameters and standard deviation of samples etched for different etching times. All samples were sensitized with UV light prior to the etching. However, the ion type and the aging periods for these foils were different, which resulted in diverse etching rates. The black and green curves show a perfect linear dependence. However, the aging times are different, being 4.5 months for the black curve, and 19 months for the green curve. Additionally, they were irradiated with different ions: Bi ions (black curve) and Au ions (green curve), both with an energy of 11 MeV. Since the energy loss of both ions in the PC foils is comparable, the difference in etching rates (22.37 nm/min for black and green curves, respectively) is assigned to the aging of irradiated foils. The etching rate was deduced from the slope of the linear fits. The inset in Figure 13 shows the etching rate values as a function of the age of the irradiated foils. The red curve corresponds to samples which were irradiated with Au ions and the longest aging period of 44 months. Despite the deviation at the point corresponding to 5 min etched sample, assuming the linear behavior, the etching rate was calculated from the slope to be 28 nm/min.

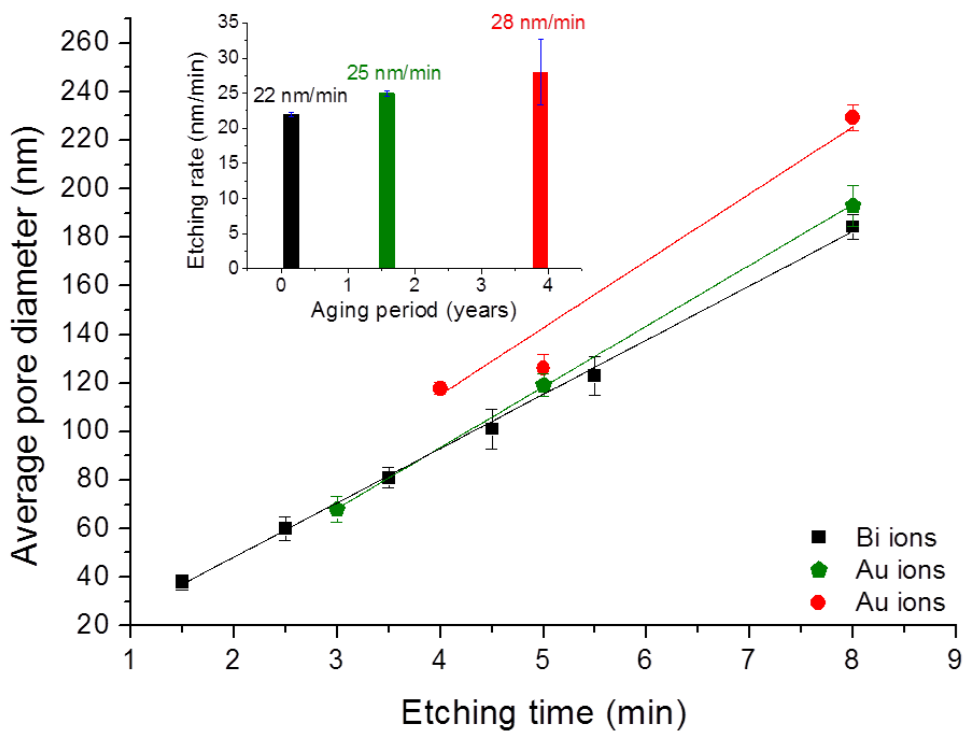


Figure 13: Average pore diameters measured with SEM as a function of etching periods 4.5 month (black), 19 month (green), 44 months (red).

Last but not least, the variation of the etching rate from sample to sample can also arise from the concentration of the etching solution and the temperature in the bath: higher pH and temperature will result in faster etching, and vice versa.

3.2. Vertically aligned conical pores by asymmetric etching

To fabricate membranes with conical channels, the etching of the irradiated PC foils with a thickness of 30 μm and parallel tracks with a number density of 10^8 cm^{-2} was performed in a specially constructed electrochemical cell under asymmetric etching conditions. A schematic of the setup is shown in Figure 14a. The foils were introduced in between two compartments of the cell. One compartment was filled with the etching solution containing a mixture of 9M NaOH and methanol in a 60:40 volume ratio, while the other compartment was filled with deionized water which served as a stopping solution. In such a configuration, the etching took place only on one side. Due to the addition of methanol to the NaOH etchant, a conical pore geometry with a large base and reduced tip diameters was achieved. During the etching process, the temperature of the cell and solution was kept at 30°C. A potential of 1 V was applied between two gold electrodes that were immersed in the etching and stopping solutions. The potential difference between the two electrodes prevented the backflow of OH^- ions of the etching solution into the stopping solution, thereby slowing down the etching process and allowing the formation of conically shaped channels. The current as a function of etching time was monitored and recorded. Once the tracks were etched through, the current started to flow and increased with time (Fig. 14b). The breakthrough point is indicated by a sharp current increase occurring at 40 s. The samples were etched for 12 min, resulting in conical pores with a base and tip diameters of 2.5 μm and 700 nm, respectively.

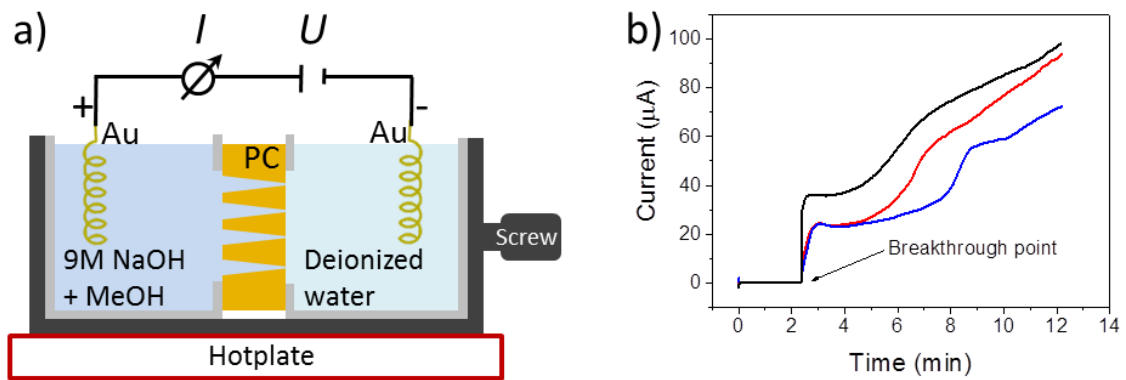


Figure 14: a) Schematic of asymmetric etching setup consisting of two compartments for etching and stopping solutions, and the membrane fixed in between the two compartments. b) vs. time curves of chemical etching of conical pores with a similar breakthrough point for different samples.

3.3. Membranes with networks of interconnected pores

Membranes with interconnected nanopore networks were prepared by chemical etching of irradiated PC foils with tilted intersecting ion tracks. The networks were obtained by irradiating the foils at different angles with respect to the surface normal of the polymer foil (Figure 15). At each position, the foils were irradiated with a fluence of 10^8 or $2 \cdot 10^9$ ions/ cm^2 , resulting in a total fluence of

2 10^{19} , 4 10^{19} and 8 10^{19} ions/cm² respectively. The irradiated foils were symmetrically etched for 15 min in 6M NaOH at 50°C (as described in Section 3.1), which resulted in networks of nanochannels with defined channel diameter and the etching rate is slightly slower than that in case of parallel cylindrical pores, which is probably due to the complex and dense structure of interconnected pores. According to a systematical SEM analysis of series of 5, 7 and 9 min samples, the etching rate was 22 nm/min (Appendix A). The total inner surface of the nanopore networks depends on the ion fluence and channel diameter

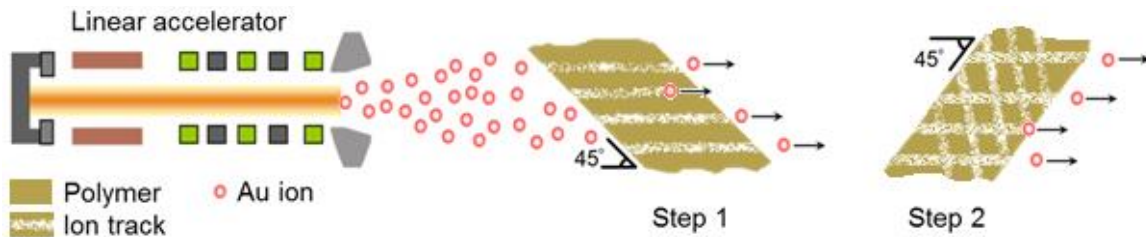


Figure 15 Irradiation scheme for obtaining nanochannel networks (only two out of four directions are shown).

Figure 16a shows the schematic of the sections of the simplest configuration of a network structure irradiated in four steps. Unfortunately, long term etching of high networks (e.g. more than 7 min etching of networks with total density of 10^{18} cm⁻²) led to dissolution of the membranes because of severe overlap of etched pores. This seemingly inevitable problem was circumvented by irradiating the network samples additionally from a fifth position under normal incidence of the beam (perpendicular to the surface of the foils) instead of increasing the fluence of ions for irradiation under an angle. In other words, to obtain the same total track density of 10^{18} cm⁻² (2 10^{19} ions/cm² from 4 directions) the foils irradiated with 1.6×10^{19} ions/cm² from 5 directions. The cross section of such network structure is shown in Figure 16b, where the parallel vertical pores correspond to the fifth step of irradiation. This fifth step also has a positive influence on the homogeneous growth and mechanical stability of the network electrodeposited in membranes. Another approach to increase the surface area was irradiation of pre-etched membranes with conical or cylindrical pores (Figure 16 c,d). First, the 30 and 60 μ m thick PC foils were irradiated with heavy ions using a rather low fluence varying between 5 and 10 10^{19} ions/cm² under normal incidence of the beam. After symmetric or asymmetric etching, vertically aligned cylindrical and conical pores were obtained. In a second step, these membranes were irradiated with higher fluences under 4 tilted beam incidences to obtain a network configuration. The etching process after the second irradiation resulted in a network combined with vertically aligned conical cylinders with significantly increased surface area. Last but not least, reverse networks were fabricated, where the network had a height of 1/3 or 2/3 of the length of the cylindrical conical channels (Figure 16 e,f). These structures may be useful for the synthesis of very long

wire arrays. They will allow stabilization of the array at the base of the wires, whereas the top of the wires will stay free of network while vertically aligned without assembling bunches. This property is especially important e.g. for nanowire array emitters.

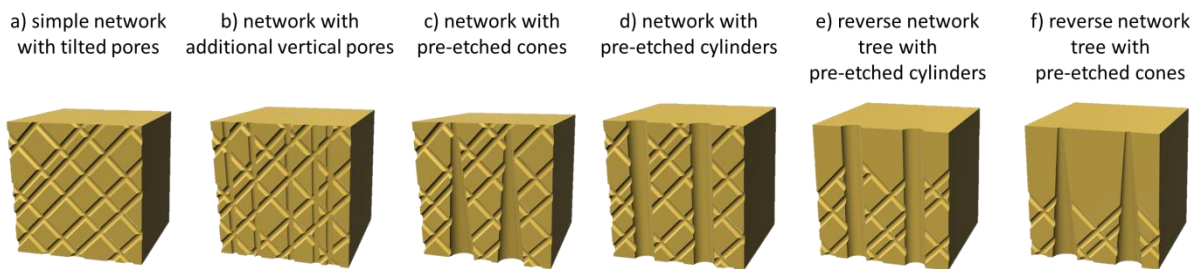


Figure 16: Schematics representation of cross-sections of) the simplest and b) advanced configurations of a network structure obtained after etching of PC foils irradiated for four and b) five steps networks combined with pre-etched vertical (c) conical and d) cylindrical array: e, f) reverse network tree structures showing cylindrical or conical pores support network at the base.

Figure 17 shows representative SEM images of a network membrane surface (a) and cross-sections (b) of different types of network structures. In Figure 17a, a typical porosity surface of a network membrane is shown (here the total pore number density is 10^9 pores/cm²). The inset presents a higher magnification image of 210 nm pores formed by irradiation from four different directions (marked with arrows) under an angle of 45° and etched for 10 min. The cross-section of a similar membrane with pores of 150 nm diameter (etched for 7 min) is shown in Figure 17b. The roughness at the edge of the polymer is due to the breaking of the membrane. Three of the four irradiation directions are indicated by arrows in the zoomed image. For the fourth direction, only the openings can be identified from this image. Figures 17c and 17d show the cross-section of networks combined with pre-etched vertically aligned conical and cylindrical channel arrays respectively. The inset in Figure 17c shows the cross-section of a cone with the network channels penetrating through the cones. The two insets in Figure 17d present the cross-section (top) and surface (bottom) of a membrane with pre-etched cylindrical pores (20 min etching, density of 10^6 cm⁻²) and post-etched nanochannel network (5 min etching).

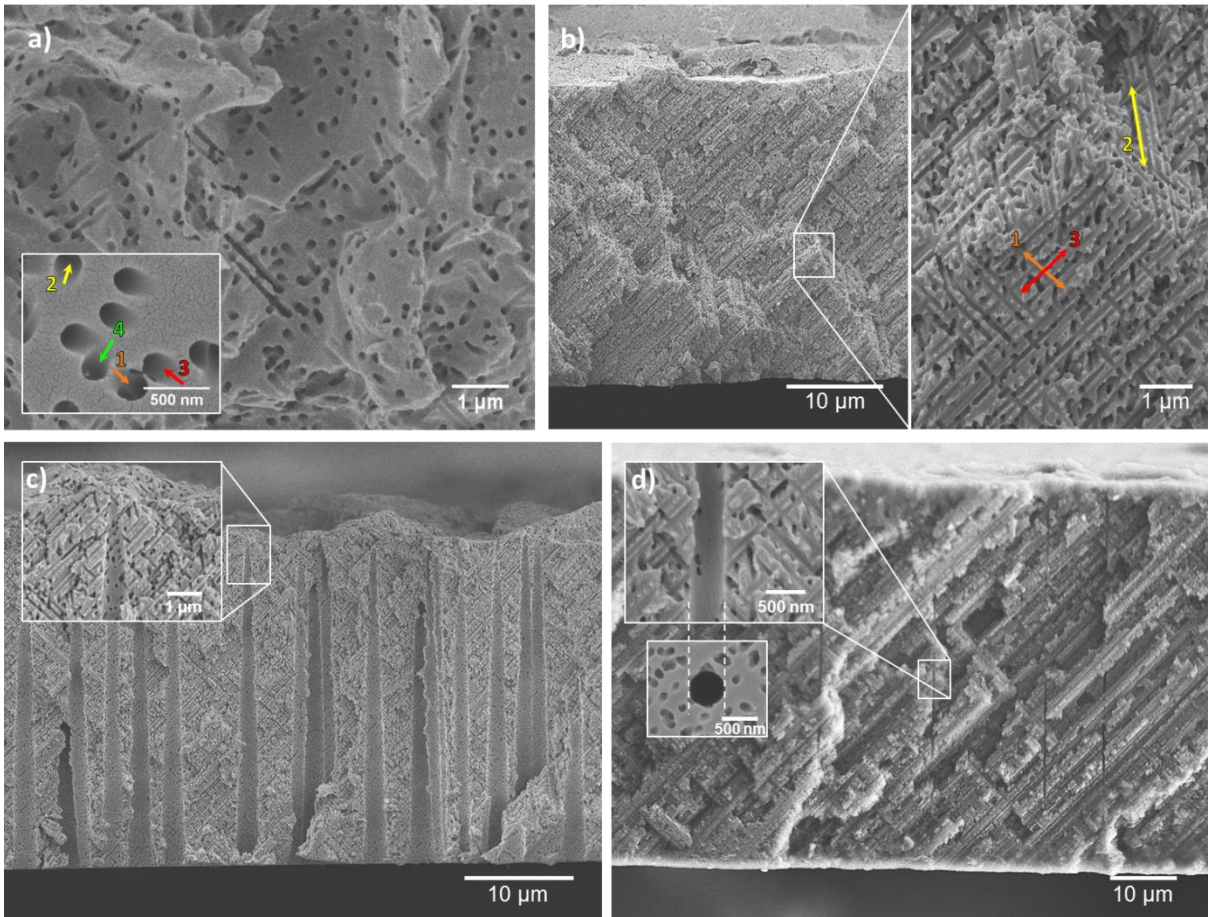


Figure 17: SEM images of a) the surface of a network membrane with an inset showing a network formed by irradiation from four different directions under an angle of -45° ; b) membranes with high aspect ratio network channels indicating three out of four directions of intersecting pore networks combined with vertically aligned channels; c) conical channel arrays. The inset in (c) presents the cross-section of the tip of a conical network. The two insets in (d) show the section (top) and surface (bottom) of a membrane with preetched cylinder and polished channel network.

Additionally, series of PC foils were irradiated with a lead mask in front of foil stack. These masks, which had defined circular opening in the center with a diameter of 5, 7 or 15 mm, prevented the penetration of the heavy ions through the mask, and only the open area to the foil was irradiated. This resulted in the formation of networks with a confined area, which improved the efficiency of the electrodeposition process (see Section 4.3.1).

The synthesis of ZnO cylindrical, conical nanowires and interconnected nanowire network inside etched membranes is discussed in Chapter 4

4. Electrodeposition and characterization of ZnO micro and nanowires

This chapter deals with the reproducible growth of ZnO nanowire based structures in a controlled manner. The electrodeposition conditions, such as the applied potential, electrolyte concentration and electrodeposition time as well as the pore diameter were varied to study their influence on the morphology and the crystallographic properties of the aligned cylindrical nanowire arrays. Additionally, vertically aligned conical ZnO nanowire arrays are presented. A nanowire network system consisting of tilted intersecting cylindrical wires is highlighted. The growth conditions and parameters of the wires (diameter, density and length) in the networks are adjusted in order to obtain homogeneous and stable 3D structures.

4. Electrodeposition and characterization of ZnO micro- and nanowires

Etched ion track membranes are being used since decades as templates for the electrochemical deposition of nanostructures inside the channels. In general, electrodeposition of micro- and nanowires can be carried out using either a two electrode setup in potentiostatic or galvanostatic mode, as well as by pulsed electrodeposition conditions. In this work, a two electrode setup was used for electrodeposition of a so called backelectrode, which is deposited on one side of the membrane to close the pores and serve as a working electrode for the membrane during the growth of the nanowires. The synthesis of ZnO nanowires was performed in a three electrode configuration in potentiostatic mode, as described in Section 2.2. The process for the synthesis of ZnO nanostructures is schematically shown for the case of networks in Figure 18, and consists of the following steps: a) irradiation of polycarbonate (PC) film with a heavy ion (e.g. Au or Bi), b) chemical etching for transformation of the ion tracks into channels, c) sputtering and electrodeposition of metallic layer (backelectrode) as an electrical contact, d) electrodeposition of nanowires, e) removal of the polymer by dissolution in dichloromethane. The same steps were employed for the synthesis of the arrays of the cylindrical nanowires.

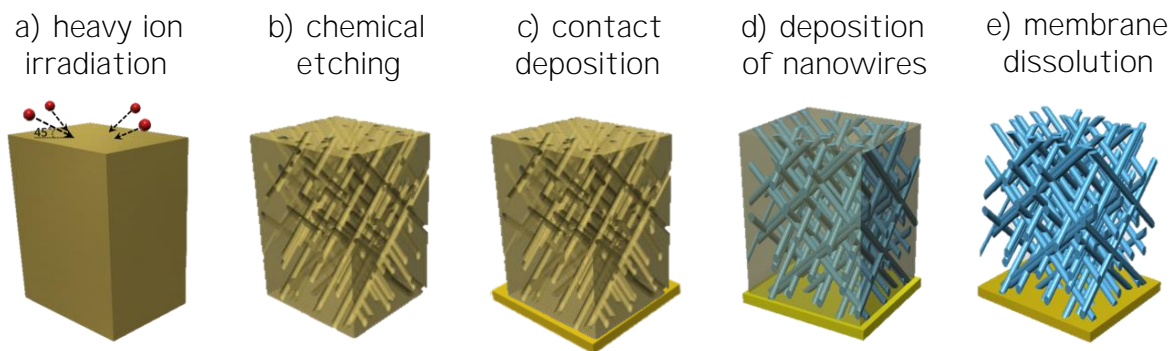


Figure 18 Schematic view of different steps of nanowires synthesis a) heavy ion irradiation, chemical etching in 6M NaOH, c) gold sputtering and electrochemical deposition of metallic (Au or Cu) backelectrode as a back contact, d) electrochemical deposition of nanowires, e) dissolution of the polymer.

4.1. Cylindrical micro- and nanowires

For electrodeposition of parallel cylindrical nanowires, 30 μm thick membranes with pore number density of 10^9 cm^{-2} were used. Different parameters and conditions, such as the applied potential, size of the pores in the membranes, electrodeposition time, and concentration of the electrolyte were varied in order to observe changes of morphology, composition and texture of the wires depending on deposition conditions. The electrodeposition and characterization of ZnO nanowires are presented in the following sections.

4.1.1. Preparation of the back-electrode

Prior to the electrodeposition of the back-electrode, a 20 nm thick Au layer was sputtered (Edwards Sputter Coater S150B, 1.5 Torr, 1.6 kV, 15-20 mA) on one side of the PC membrane to provide an electrical contact to the sample. This sputtered layer was then reinforced with either gold or copper back-electrode which closes the channels on one side of the membrane and thereby prevents flow of the electrolyte through the pores to the back side of the sample. Additionally, the back-electrode acts as a working electrode during electrodeposition of the nanowires. Both Au and Cu layers serving as back-electrodes were electrochemically deposited in an electrode setup shown in Figure 9 for the case of Au deposition. The PC membrane was introduced in the vessel between the two Teflon compartments in such a way that the sputtered side was in contact with the Au bath which was used to electrically contact the membrane. The Au layers were grown at a constant potential of 0.7 or 0.8 V resulting in a current of 1 mA. A commercial gold sulphite (AuSF, 15 g/L Au, METAKEM) was used as electrolyte. A Au rod was the anode. Cu back-electrodes were deposited at a constant potential of 0.5 V using a solution of 238 g CuSO₄·5H₂O (Sigma Aldrich, >98%) and 21 g H₂SO₄ (Merck, 99.7%) and a Cu rod as anode which resulted in a current of 20 mA during the electrodeposition.

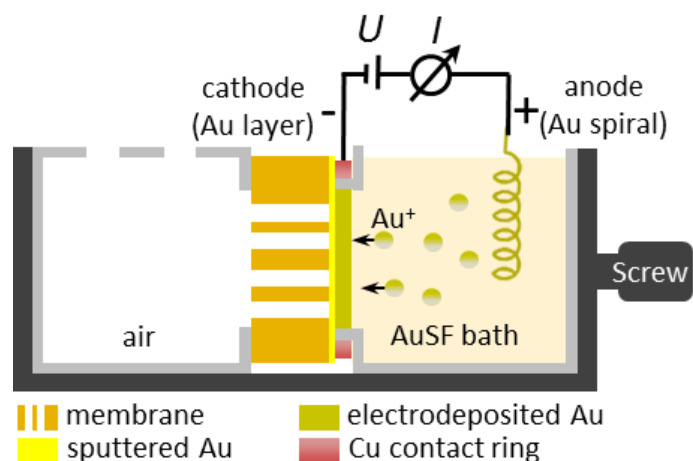


Figure 9. Schematic representation of the electrode setup for electrodepositing an Au layer on the sputtered gold of the membrane by applying a constant potential of 0.8 V.

Depending on the pore size of the membrane, the deposition time for the back-electrode was increased to assure the complete coverage of the pores. For pores with a diameter up to 300 nm, Cu and Au layers were deposited for 45 min and 3.5 h, respectively, which corresponded to a thickness varying between 7 and 10 μm in both cases. After deposition of the back-electrode, the samples were rinsed with deionized water and dried with a stream of nitrogen gas.

4.1.2. Synthesis of arrays with parallel cylindrical ZnO wires

Figure 20 schematically presents the three electrode configuration of the setup employed for electrochemical deposition of the wire array. The electrodeposition was performed using a potentiostat (GAMRY Instruments, Reference 600C) with Cu layer on the membrane acting as a working electrode, Pt spiral wire (Good fellow, 99.9+%) as a counter electrode and a Ag/AgCl reference electrode (Sensortechnik Meinsberg GmbH KCl). The membrane was fixed in between two Teflon cell compartments so that the metallic layer was in contact with copper rings serving as contact between the membrane and the external circuit.

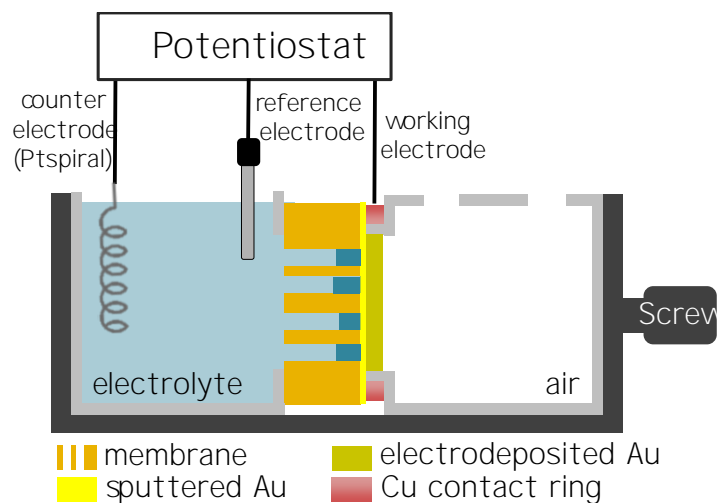


Figure 20 Schematic representation of the three electrode setup consisting of working, counter and reference electrodes and connected to potentiostat

30 μm thick etched ion track membranes with various pore diameters between 40 and 300 nm were employed as templates. Aqueous solution containing 0.1 or 1 M zinc nitrate hexahydrate $\text{Zn}(\text{NO}_3)_2 \cdot 6\text{H}_2\text{O}$ was used as an electrolyte. To wet the pores of the membrane completely, the electrolyte was filled in the cell 1 h before applying. Different potentials ranging between 0.5 and -1 V vs. Ag/AgCl and a temperature varying between 60 $^\circ\text{C}$ and 80 $^\circ\text{C}$ were applied and adjusted for reproducible growth of these wires. Influence of the deposition parameters (deposition time, electrolyte concentration and potential) on the morphology and crystallographic properties of the nanowires was investigated by using scanning electron microscopy (SEM) (energy dispersive X-ray spectrometry (EDX)), and X-ray diffraction (XRD), respectively. The sample preparation processes for the measurements are described in Chapter 4. Novelty was the study of the influence of the pore diameter on the crystallographic properties of ZnO nanowires. The results are summarized in the following sections.

4.1.3. Influence of the electrolyte concentration on the morphology of the wires

30 μm PC foils with pore diameter of ~ 200 nm and density of 1.0 were employed as templates to grow ZnO nanowires using 0.1 and 1 M $\text{Zn}(\text{NO}_3)_2 \cdot 6\text{H}_2\text{O}$ electrolytes at fixed temperature and potential being 80 and 0.8 V vs. Ag/AgCl, respectively. As an initial step the parameters for the temperature and potential were adapted from Sim⁴⁶. After the electrodeposition, the polymer matrix was removed by immersing the samples into a dichloromethane bath and washing in several steps. The morphology of the clean wires was studied by using SEM.

Figure 21 shows SEM images of the resulting deposits from a) 0.1 M and b) 1 M electrolytes. The wires grown using a lower concentration electrolyte display a smoother surface (Figure 21a) as compared to the wires which were deposited from a higher concentration electrolyte bath (Figure 21b). The deposition rate was slower for the sample grown from the 0.1 M electrolyte due to the lower concentration of the ions, which led to the growth of continuous and smooth wires, while very rough and brittle wires were obtained from the higher concentrated bath (1 M). For this further studies of different ZnO wires were performed by using 0.1 M electrolyte.

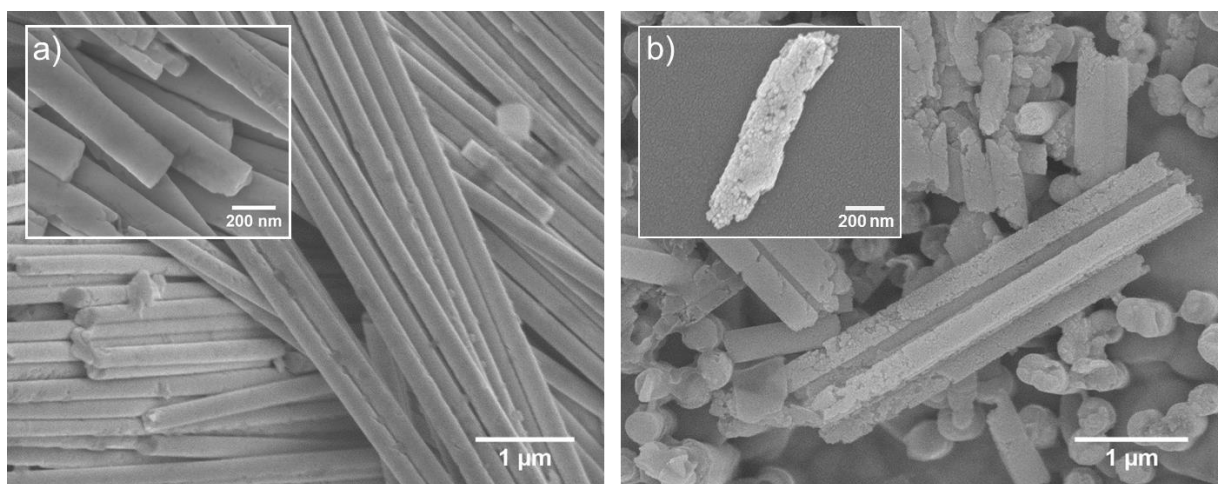


Figure 21: SEM images of ZnO wires with a) smooth and b) rough morphology prepared at a temperature of 80 $^{\circ}\text{C}$ and a potential of 0.8 V vs. Ag/AgCl using 0.1 and 1 M $\text{Zn}(\text{NO}_3)_2 \cdot 6\text{H}_2\text{O}$ electrolytes respectively.

4.1.4. Influence of the applied potential on the morphology and texture of the wires

To study the influence of the electrodeposition potential on the morphology and crystal structure of the nanowires, series of identically prepared membranes with channel diameter of 250 nm and Cu back electrodes were prepared. Potentials between 0.5 and 0.8 V vs. Ag/AgCl were applied using a 0.1 M $\text{Zn}(\text{NO}_3)_2 \cdot 6\text{H}_2\text{O}$ electrolyte at 80 $^{\circ}\text{C}$. Cyclic voltammetry previously performed using membranes with a Cu back electrode, applying negative potentials from 20 V vs. Ag/AgCl at a scan rate of 10 mV/s, revealed a reduction peak at 0.8 V, which was assigned to the reduction of H^+ . The chosen applied

potentials are thus less negative than the reduction potential. Figure 22a shows representative chronoamperometric (CA) curves of three electrodeposition processes at applied potentials of 0.5, -0.7, and -0.8 V. The deposition current increases with the increase of applied potential, which is related to a larger amount of deposited charge.⁸⁷ At various potentials different ratios of Zn²⁺ and OH⁻ ions are reproduced: higher potentials lead to the formation of more ions, so in this case more charge is deposited on the same area of the working electrode than in the case of lower potential.

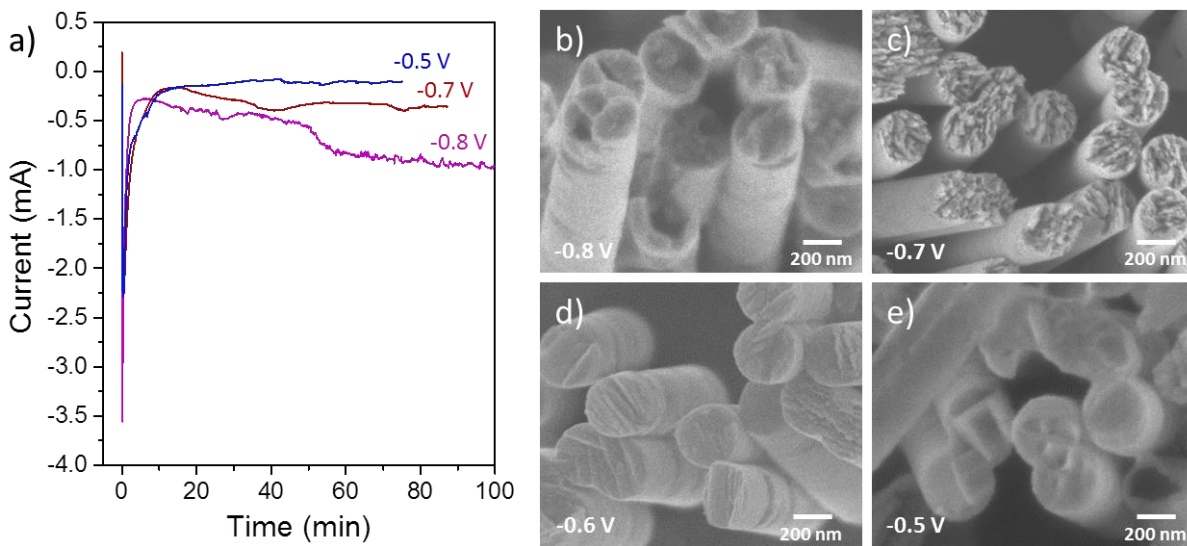


Figure 22: a) Chronoamperometric curves of electrodeposition of ZnO nanowire arrays at potentials of 0.5 (blue) -0.7 (red) and -0.8 (purple) V vs. Ag/AgCl at 80 / ° G 9 A (top view) of nanowires with 250 nm diameter synthesized at different potentials (-0.8 V (b), d) -0.6 V, and e) -0.5 V vs. Ag/AgCl.

Figure 22 (b-e) show top views of four nanowire samples deposited at potentials of 0.8 V (a), -0.7 V (b), -0.6 V (c), and 0.5 V (d) vs. Ag/AgCl. The images indicate a clear change in wire morphology depending on the applied potential. Nanowires deposited at 0.8 V display tips with a poorly defined shape, whereas the tips of the wires deposited at -0.7 V exhibit small spike-like grains. At a potential of -0.6 V the tips show platelet-like grains parallel to the surface, normal indicating a possible change of crystal orientation. Wires deposited at -0.5 V display tips which look smoother and seem to consist of larger grains. The different tip morphologies are an indication that the applied voltage has an influence on the grain size and the crystallographic structure of the wires.

Furthermore, the crystallographic orientation of the nanowire arrays deposited at various potentials was investigated by XRD. Figure 23a displays the XRD patterns normalized to the (002) reflection. At 2θ = 35.1°, 38.1°, 47.5°, and 56.6°, respectively, reflections of the (100), (101), (110), and (112) planes were observed, corresponding to known values of hexagonal wurtzite ZnO with cell constants a = 3.25 Å and c = 5.19 Å. All samples show the presence of several ZnO reflections indicating that the nanowires are either polycrystalline, i.e. each wire consists of grains with different orientations or the array

consists of single crystalline nanowires where each wire has a different orientation. No reflections at higher Bragg angles were detected. Neither pure ZnO nor ZnO were detected. The XRD patterns show reflections from the ZnO (1010), ZnO (0002), ZnO (1011), Au (111), Cu (111), ZnO (1012), Cu (200), ZnO (1120) and ZnO (1120) planes. The Au layer was sputtered on the substrate.

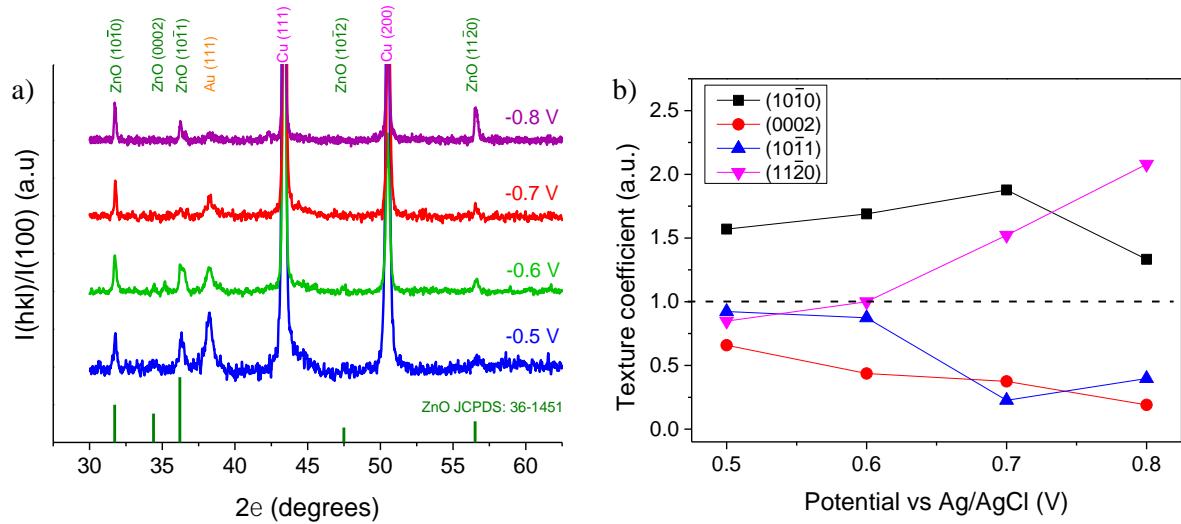


Figure 23: (a) Normalized XRD patterns of 250 nm ZnO nanowire arrays deposited at -0.8 V (purple), -0.7 V (red), -0.6 V (green) and -0.5 V (blue) vs. Ag/AgCl. The bars in green correspond to the values from JCPDS card No. 36-1451. (b) corresponding texture coefficients of the (black), (red), (blue), and (pink) reflections.

Compared to the ZnO reflections expected for diffraction of polycrystalline powder (JCPDS 36-1451), vertical lines in Figure 23(a) spectra exhibit an enhanced ZnO reflection. This is in contrast to most electrodeposited ZnO films and nanowires reported in literature, where the growth perpendicular to the planes is more favorable. For these nanowire arrays, the relative intensities of the (1010) and (1120) reflections decrease and the intensity of the (0002) reflections increases with the increase of the applied potential. This may indicate that at higher voltages more (1120) planes are formed, while at lower voltages the growth of (1010) planes predominates. This effect can also be related to the different morphology of the tips shown in Figure 22.

To investigate the preferred orientation of the nanowire arrays, the texture coefficient of given (hkl) planes for all relevant orientations were calculated using the following equation,

$$T.C. = \frac{I(hkl)}{\sum I(hkl)} \cdot \frac{\sum I_{std}(hkl)}{I_{std}(hkl)} \quad (13)$$

where n is the number of peaks (hkl), $I(hkl)$ is the intensity of the reflection measured from the nanowire array (given in Miller indices), and $I_{std}(hkl)$ is the intensity of the

corresponding peak of a ZnO powder reference. The increase of polycrystalline samples, TC is one for all planes, whereas $TC > 1$ indicates a preferential orientation of the grains in the sample and $TC \approx 1$ would mean that the structure is single crystal. The calculated texture coefficients are shown in Figure 23b. The texture coefficients do not increase from ~1.6 to ~1.9 for the wire arrays deposited at potentials between 0.5 and 0.7 V, and decreases to ~1.3 for 0.8 V. The TC values above one for the planes indicate that the preferred orientation is still parallel to the wire axis. The values in Figure 23b also reveal an increase of TC at more negative potentials for all samples. In particular, for nanowires prepared at the increase of TC is accompanied by a small decrease of θ . Moreover, for nanowire arrays deposited at higher potentials, the TC for the hkl and $h'k'l'$ planes diminish. However, given that $n = 4$, the samples do not exhibit a strong texture, but rather the presence of crystals oriented in various directions, and a moderate preferred orientation ($\theta = 45^\circ$ for $U = -0.8V$).

4.1.5. Relation between nanowire diameter and crystallographic properties

In order to investigate how the diameter of nanochannels in the membrane influences crystallographic orientation of the wires, series of PC membranes with nanochannel diameters of 45, 65, 85, 110, and 160 nm and Au back electrodes were fabricated and used as templates for the electrodeposition of ZnO, potentials ranging between 0.5 and 0.8 V at 80 °C from 0.1 M $Zn(NO_3)_2 \cdot 6H_2O$ were applied. Successful growth was observed for membrane with a pore diameter of 160 nm at 0.8 V vs. Ag/AgCl whereas no effective deposition occurred for smaller diameters at none of 0.5 and 0.8 V. The filling in these small pores was either very poor or missing. Therefore a more negative potential as compared to the wires discussed above was applied. Efficient depositions were performed as Ag/AgCl for all membranes with pore diameters between 45 and 160 nm. The need for higher deposition potential can be due to limited diffusion and mass/charge transport processes. When the diameter is decreased, the aspect ratio of the pores increases. Because the metal ion concentration in the electrolyte is relatively low (0.1 M $Zn(NO_3)_2 \cdot 6H_2O$), diffusion limitation results in a higher resistance of the electrolyte in the pores, and a higher electric driving force is needed for efficient deposition. It is also worth mentioning, that this set of samples had a Au substrate, while the wires mentioned in Section 4.1.4 were deposited on Cu substrate, which might influence the nucleation and growth of ZnO, however for this assumption no proof is available.

The chronoamperometric curves of the set of samples with diameters shown in Figure 24. The constant potential (vs. Ag/AgCl) was applied for 1, 2, 3, 4, and 5 h for membranes with a pore diameter of 160, 110, 85, 65, and 45 nm, respectively. The time was chosen according to the diameter, on the one hand to avoid overgrowth and formation of caps, and on the other hand to fill the pores sufficiently with material for XRD analysis. As the diameter of the pores and hence the effective area of the working electrode is decreased,

the absolute value of the current is also decreasing, although the current density should remain the same for all samples

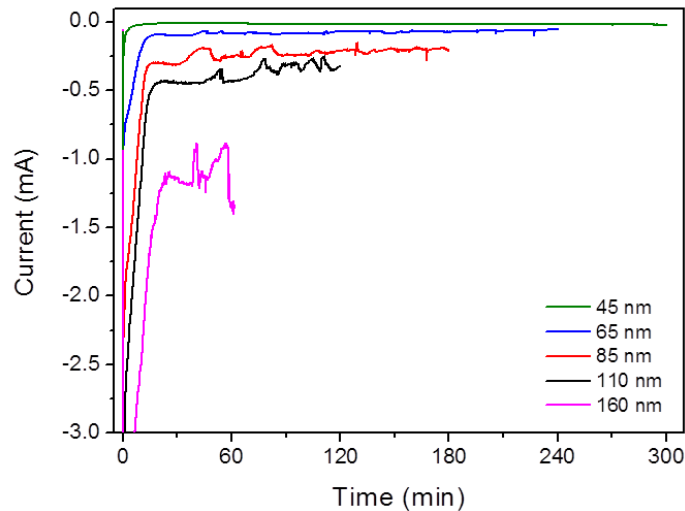


Figure 24 Chronoamperometric curves of ZnO nanowire electrodeposition in men diameters of 45 nm (green), 65 nm (blue), 85 nm (red), 110 nm (black), and 160 nm (magenta). The deposition was carried out in 0.1 M $Zn(NO_3)_2 \cdot 6H_2O$ electrolyte at a constant potential of $Ag/AgCl$ at 807

To analyze the nanowires by SEM, the polymer matrix was removed with dichloromethane. The detailed process of the sample cleaning and preparation for measurements are described in Chapter 4. Nanowires transferred onto Si wafers were analyzed by SEM with respect to their morphology and diameter. The mean diameter and the standard deviation of ~50 individual nanowires from different parts of the same sample were determined. The dependence of the average diameter on etching time is shown in Figure 25. The error bars represent the standard deviation values. The diameter values of pores and wires are in agreement and in both cases show a linear dependence on the etching time between 4.5 min. However, as it was observed earlier, the values measured for the channels are slightly (6 ± 1 nm) smaller than the diameters measured for the wires grown in the pores. This small difference is attributed to the 8 nm Au layer that was sputtered on the polymer surface for SEM investigation, slightly reducing the pore size by a few nm. Figure 25(b-f) display nanowires with average diameter of 160 ± 6 , 110 ± 4 , 85 ± 6.6 , 65 ± 4 and 45 ± 1.5 nm, respectively. All analyzed wires exhibit a relatively rough morphology resembling voids, but no clear dependence between morphology and wire diameter was observed. Since it is known from deposition of different kind of materials that the walls of pores in the polymer membrane are smooth, the roughness is ascribed to the high deposition rate of wires.⁴³ EDX analysis of single nanowires (area and line scans) showed the presence of zinc and oxygen in a ratio close to 1:1 and the absence of any impurities. A representative line scan is included in Figure 25(e). The Si signal originated from the substrate

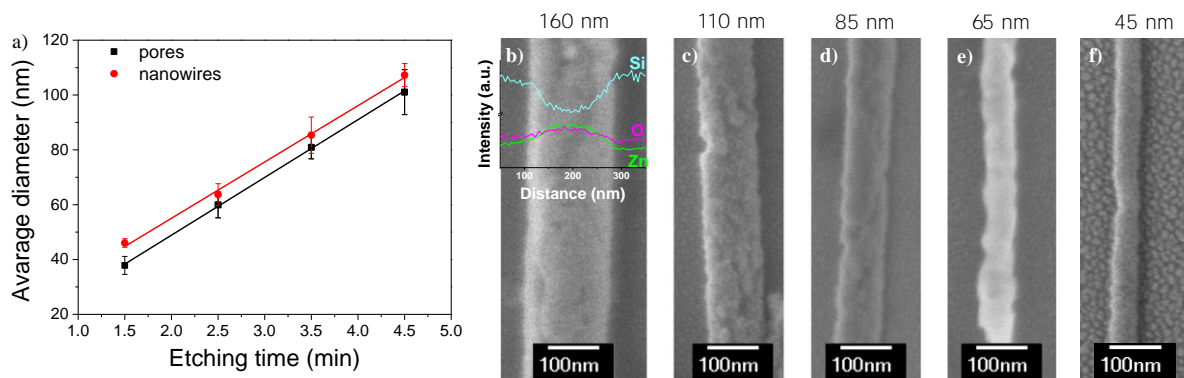


Figure 2 a) Average diameter measured by SEM for pores (black) and wires (red) at an etching time of 1.5, 2.5, 3.5, and 4.5 min. b-f) Individual nanowires with an average diameter of b) 160, c) 110, d) 85, e) 65, and f) 45 nm on Si wafers. Inset in (b) shows a representative EDX line scan.

For XRD characterization the nanowires were kept embedded inside the membranes. The XRD patterns measured on these samples are presented in Figure 3. The diffractograms are normalized to the ZnO reflections. Four ZnO reflections corresponding to the wurzite phase, namely (100), (101), (102), and (103) were observed whose relative intensities varied for the different samples. The mentioned reflections were more pronounced for the wires with smaller diameters, namely 45 and 65 nm, and slightly for 85 nm wires. For nanowire arrays with wire diameter of 110 and 160 nm reflections (100) and (101) are almost negligible. However, for TC calculations all 4 reflections were taken into account for a comparison of all samples. These patterns can also explain the morphology difference of the wires. Apparently, wires with smaller diameter tend to be more polycrystalline, which means that the random growth of the crystals result in the formation of voids and rough surfaces as it was shown in Figure 2. The two high intensity Au reflections originating from the back electrode. The XRD spectra confirm that the nanowires are pure ZnO and that there is no Zn deposition under the applied conditions. The calculated TC data are presented in Figure 4. The array of nanowires with largest diameter, namely 160 nm, displays the highest i.e. TC with a maximum TC value of 2.5. The texture coefficient for preferred orientation decreases for smaller wire diameters, while the TC value for the orientation increases slightly for 85 and 110 nm wires, and decreases again for thinner nanowires. For diameters below 80 nm the TC slightly increases. The tendency for having a preferred orientation and better crystallinity is higher for thicker wires, while the thinner nanowires have no defined preference of a certain orientation.

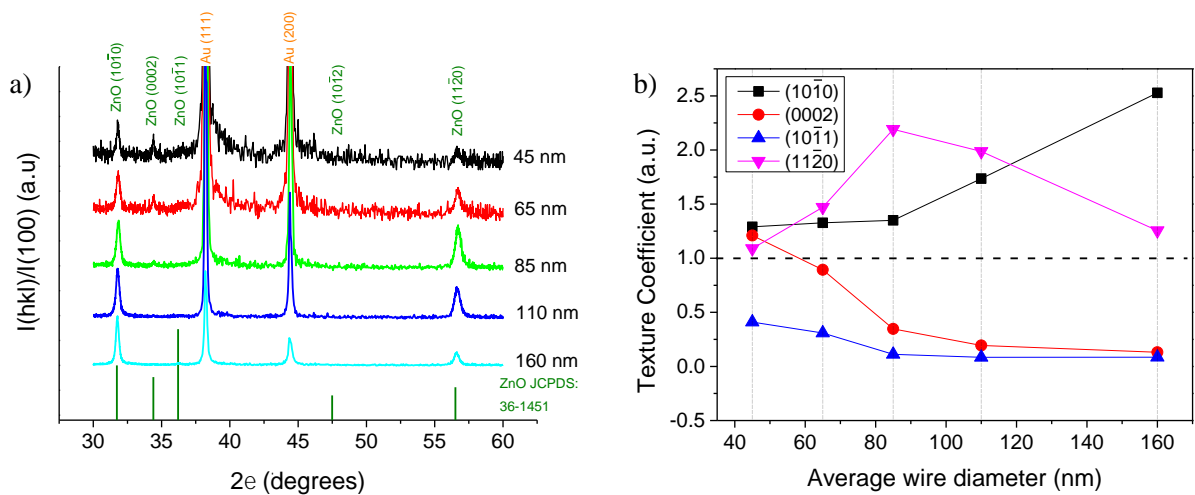


Figure 2 a) XRD diffractograms measured for arrays of nanowires with diameter of (red), 85 (green), 110 (blue), and 160 nm (cyan) and b) texture coefficient of the (black), (red), (blue), and (pink) reflections.

4.1.6. Crystallographic properties and composition depending on wire length

ZnO nanowires were grown on 1, 2, and 3.5 μm thick membranes with a diameter of 200 nm and number density of 10^2 . The electrodeposition was carried out using 0.1 M zinc nitrate hexahydrate electrolyte potential of -0.8 V vs. Ag/AgCl at 80 $^\circ\text{C}$. The crystallographic orientations of the nanowire arrays embedded in the membranes were analyzed using XRD. Figure 2a shows the configuration of the samples. The diffractograms measured for the three samples are shown in Figure 2b. In all cases, the (1010), (0002), (1011) and (1120) reflections were observed, which respectively correspond to the (1010), (0002), (1011) and (1120) planes of hexagonal wurtzite ZnO, matching well with the values available from the ZnO JCPDS 36-1451 (shown with black lines in Figure 2b). For all three samples, only these four reflections were present, indicating that the crystallinity of the ZnO wires does not change with wire length and does not depend on the deposition time. The reflection marked with a star at the angle of $2\theta = 38.2^\circ$ arising from the sputtered Au (111) layer. The copper signal arises from the electrodeposited back electrode. Wires produced under identical conditions exhibited very similar XRD spectra, confirming the reproducibility.

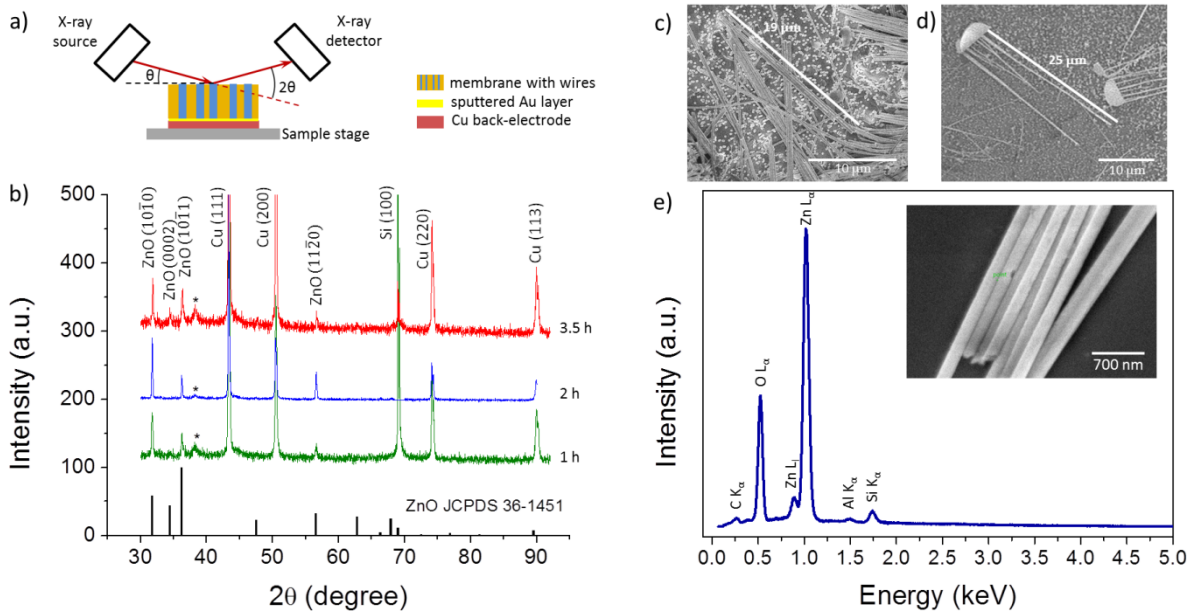


Figure 2:7a) Schematic representation of the XRD setup and the adjustment of the sample to the X-ray beam, b) XRD diffractograms of ZnO nanowire arrays with lengths of 10, 20 and 30 μm at 0.8 V vs. Ag/AgCl and 80 Torr for 1 h (green), 2 h (blue) and 3.5 h (red) in $0.1\text{M Zn(NO}_3)_2 \cdot 6\text{H}_2\text{O}$ electrolyte. The black lines represent the values known from the ZnO JCPDS card Nr. 361451. SEM images of c) $\sim 20\mu\text{m}$ and d) $\sim 25\mu\text{m}$ long ZnO nanowires in (d) the wires are still attached to the cap e) representative EDX spectrum of nanowires transferred onto a Si wafer (inset)

To measure the length of the wires deposited at different time periods as well as the chemical composition along the wires, the polymer was dissolved in methanol. During polymer dissolution some of the long wires broke and remained lying on the substrate allowing for measuring their length (Figure 27d). The average lengths for the samples for 1, 2 and 3.5 h were 7-10, 18-20 and 27-30 μm , respectively. For the sample grown for 3.5 h 3 μm wires were observed on top of several (Figure 27f). Wire transferred onto a Si wafer analyzed by energy dispersive X-ray (EDX) spectrometry for each wire at three points along the length (two at the edges and one in the middle) were measured. A representative EDX spectrum is shown in Figure 27e. The L lines of Zn and O are assigned to the wires. The K line of C probably originates from residual polymer on top of the wires. The signals from Al and Si correspond to the SEM sample holder and Si wafer, respectively. Figure 27e shows the SEM image of ZnO wires for which the presented EDX spectrum was recorded. For the majority of the measurements, the ratio of zinc and oxygen in the structure showed a stoichiometry close to 1:1, both signals were detected, suggesting that the wires consist only of Zn and O, with no significant impurities.

4.1.7. Mechanical stability of the arrays

For implementation of nanowire arrays electrodes, e.g. for solar cells or photoelectrodes for photoelectrochemical water splitting, wires are required. For the comparison of the mechanical stability of nanowire arrays samples were prepared

by electrodeposition of ZnO at 0.8 V vs. Ag/AgCl at 80°C using 0.1 M Zn(NO₃)₂·6H₂O in templates with pore number density of 10⁷ cm⁻². The two samples had similar wire diameter of ~250 nm, but different length ~7 and 20 μm. The third sample consisted of wires with diameter of ~125 nm and length of 20 μm. SEM images of arrays of ZnO nanowires with diameter of 250 nm and length of ~7 and ~20 μm respectively are shown in Figure 28(a) and (b). After dissolution of the membrane, the short wires (Figure 28a) are freestanding and have a perfectly parallel alignment, whereas the longer nanowires (Figure 28b) tend to bend and agglomerate forming bunches of nanowires with attached tips. This effect became even more crucial when decreasing the diameter of long nanowires to 125 nm (Figure 28c). These wires showed the least stability not only by bending but also by detaching from the back electrode during the cleaning process. Figure 28c, the white dots on the substrate are the bases of broken wires.

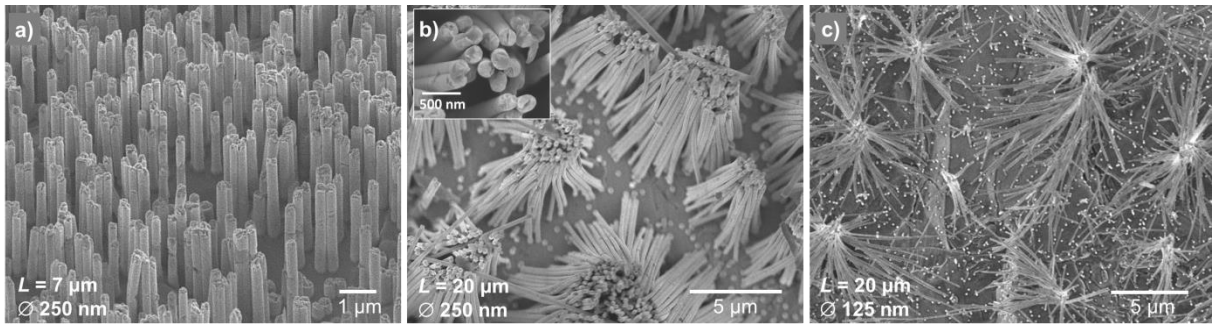


Figure 28 SEM images of (a) ~7 μm long nanowires (wire diameter of 250 nm) (b) ~20 μm long nanowires (wire diameter of 250 nm) showing mechanical stability and (c) ~20 μm long nanowires (wire diameter of 125 nm), having the poorest mechanical stability.

By increasing the wire diameter and decreasing their length, relatively stable wire arrays can be obtained. To enhance the stability and maintain the high aspect ratio of the nanowires, conical ZnO wires were studied.

4.2. Vertically aligned conical ZnO wires

For the fabrication of conical nanowires, asymmetrically porous membranes with 10⁷ pores/cm² were employed. As for cylindrical pores, also in this case the membranes were first sputtered with a thin gold layer which was reinforced with an electrodeposited layer. The potentiostatic growth of ZnO cones was carried out using the same setup and electrolyte as for the cylindrical nanowires with largest pores (200- 250 nm) namely 0.1 M Zn(NO₃)₂·6H₂O, applying a constant potential of 0.8 V vs. Ag/AgCl at a temperature of 80°C. Two different approaches of the growth process were employed: tip to base* growth¹²⁸. In the first case, the back electrode was deposited on the side of membrane with the large diameter (2- 2.5 μm) of the conical pores (referred to as base) for ~1.5 h. This

* The tip to base approach was proposed by Burr and is discussed in more details in¹²⁸

resulted in a Cu layer thickness of $\sim 152 \mu\text{m}$, which was expected to completely close pores. For the growth of the conical wires inside the pores, the samples were placed in the electrochemical cell in between Teflon compartments such a way that the open side of the conical pores with diameters below 100 nm was in contact with the $\text{Zn}(\text{NO}_3)_2 \cdot 6\text{H}_2\text{O}$ electrolyte (Figure 29). In the case of the tip-to-base growth, the back electrode was deposited on the membrane at the side where the electrolyte for the ZnO deposition entered into the pores from the base of the conical pores. The latter arrangement provided a faster filling and wetting and improved the ion diffusion inside the pores (Figure 29).



Figure 29 Schematic representation of the three-electrode setup for electrodeposition of conical nanowires with a) base-to-tip and b) tip-to-base approaches.

ZnO conical nanowire arrays were analyzed by SEM to determine the size of the base and tip as well as to study the surface morphology. Fig 30 shows SEM images of nanocones deposited by the base-to-tip method. Figure 30(a) and (b) show low and high magnification SEM images of a cone array on a substrate. At first sight, the cones look smooth with homogeneously grown walls. However, some of the cones exhibited a hollow structure near the base (marked with arrows in Figure 30). Such is typical for metals and metal oxides electrodeposited at a constant potential of sizes larger than a few hundred nm^{46,131}. The hollow bases of these cones weakened their mechanical stability and led to their breaking. However, broken wires lying on the substrate allowed measuring the diameter and length of the cones (Figure 30). Systematic analysis of different samples with identical preparation conditions yielded tip diameters in the range between 70 and 90 nm (Figure 30). The diameter of the base close to the back electrode was between 25 and 30 nm. The length of the cones after complete filling of the membrane was in the range between 25 and 27 μm . The measured cone base diameter at the point where the cone was broken was between 1.2 and 1.9 μm (Figure 30). The zone where the wires typically broke was found to be away from the back electrode. The hollow structure continued for the majority of the cones until the diameter of the conical channel in the membrane decreased to a less than a cone length of 10%. The schematic representation of the tubular structure is shown in Figure 30. The formation of a tubular shaped base of the cone results from the deposition

of the gold back electrode by sputtering. During this step the sputtered gold not only covers the surface of the membrane but also partly enters and coats the walls of the pores with a depth of up to several hundreds of nm. This coated area serves as a first nucleation center for electrodeposition, and the deposited material replicates the geometry of the sputtered Au tube at the base resulting in the growth of ZnO tubular cones.

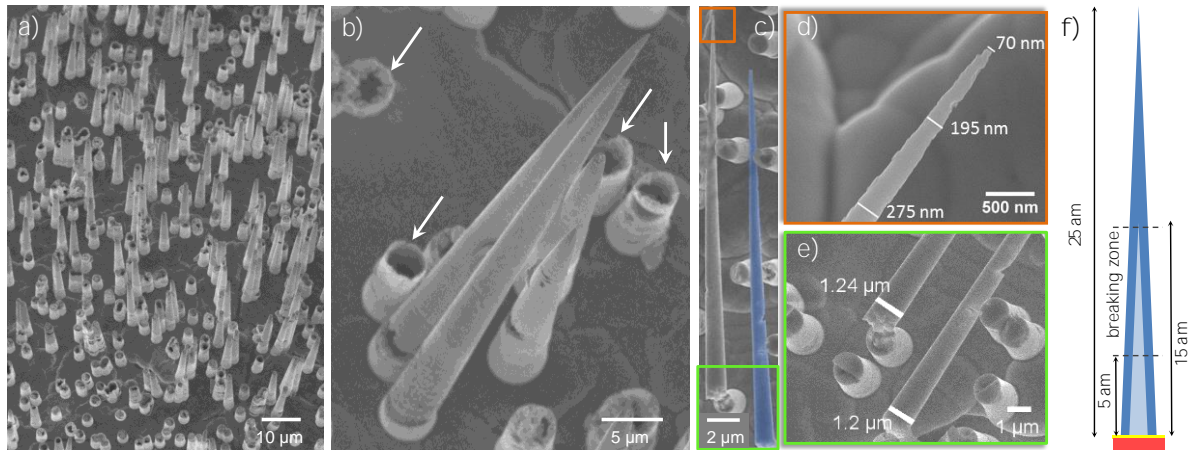


Figure 30. SEM images of ZnO conical nanowire arrays (a) and high (b) magnification showing freestanding and broken cones along individual ZnO conical nanowires with tip diameter varying between 70 and 90 nm and a base diameter at the breaking point being (c-f) schematic representation of the tubular structure of a cone with a breaking zone at the base.

The crystallographic orientation of ZnO nanowires embedded in the PC membrane was investigated using XRD. Figure 31 displays a representative XRD pattern measured on ZnO conical wires with a diameter of 90 nm. The spectrum shows the reflections of ZnO (which correspond to the 002 , 101 , 110 , 112 , and 200 planes of wurtzite ZnO). The presence of almost all possible crystallographic planes indicates that these cones are polycrystalline. The small reflection at 38.1° originates from the thin sputtered gold layer and is assigned to the (111) and (200) planes of Cu substrate. The vertical lines show the graph correspond to the values known from the ICDS cards of ZnO (green, No. 361451), Cu (purple, No. 033) and Au (yellow, No. 89369). Figure 31 shows the alignment of the sample relative to the X-ray beam. A schematic of ZnO hexagon together with the crystallographic orientations of several planes which are present in nanowires are shown in Figure 3d.

To better understand the significant difference of the crystallographic structure of ZnO conical nanowires compared to cylindrical wires, namely the presence of almost all reflections typical for ZnO powder, a closer look was taken at the hollow structure of these cones by investigating them with SEM. The typical morphologies of the inner structures observed on the same sample are presented in Figure 32.

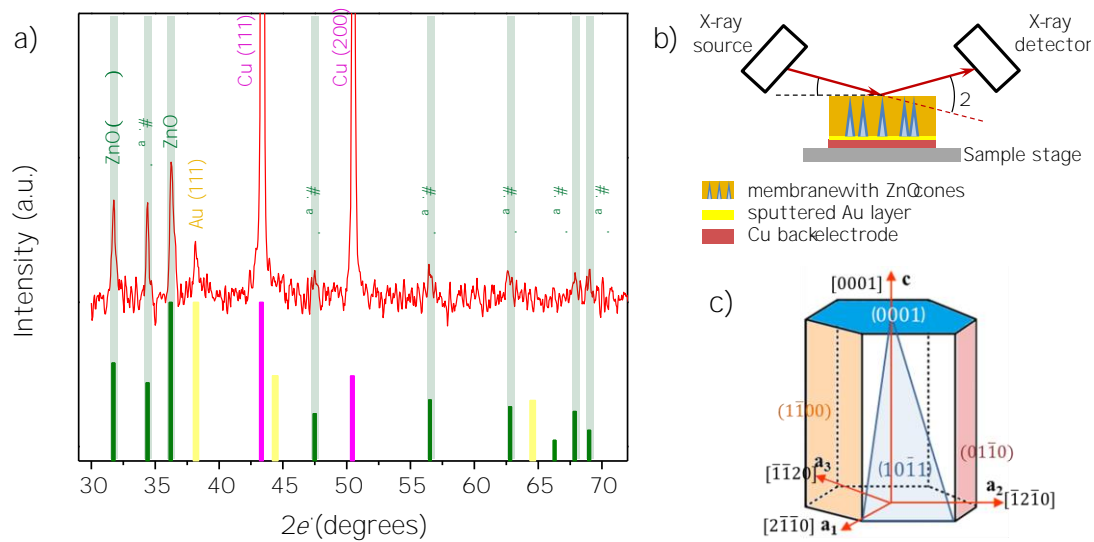


Figure 3: a) XRD pattern of conical nanowire array grown from base to tip, b) schematic representation of the XRD setup and the adjustment of the sample relative to the X-ray beam and c) the ZnO hexagonal crystal with the crystallographic orientations several planes which are commonly present in the ZnO wurtzite phase.

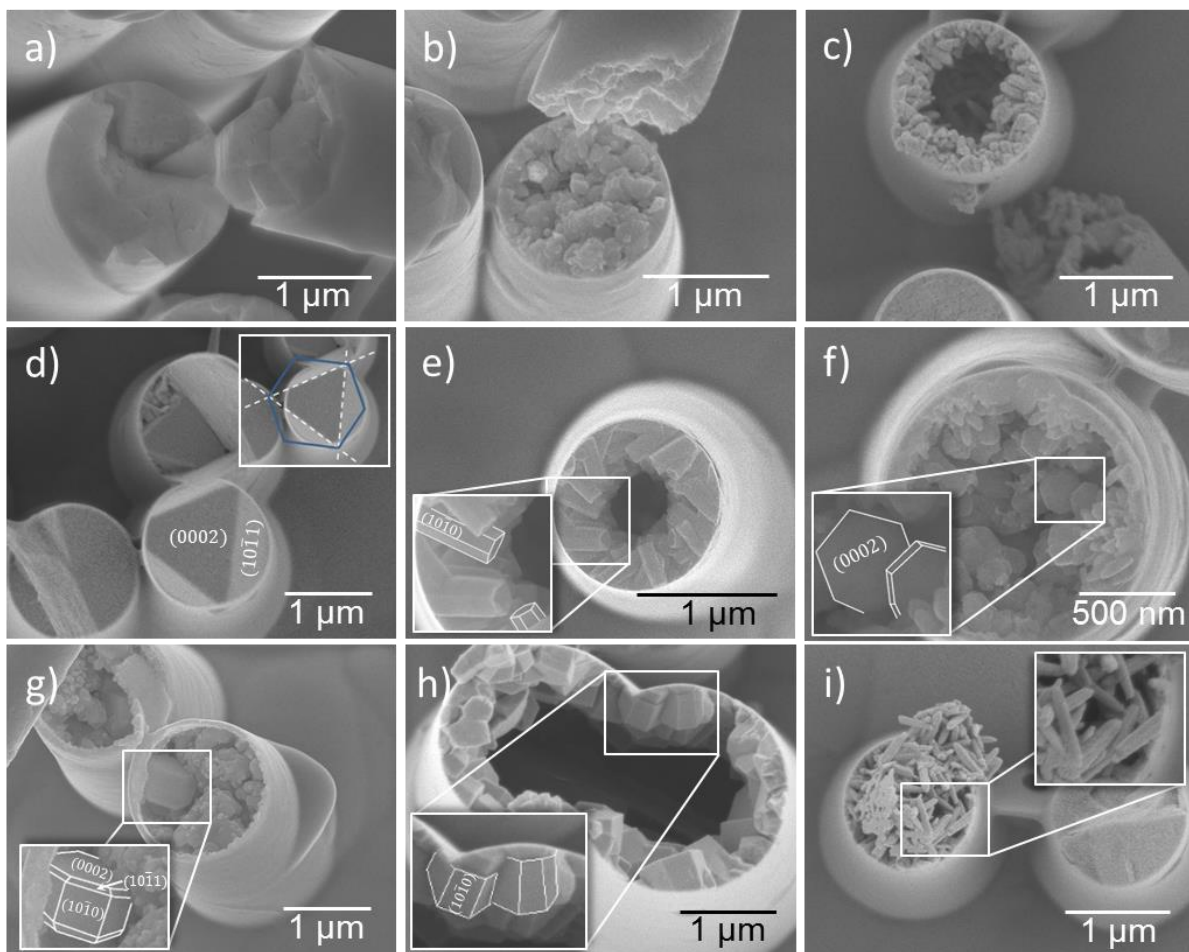


Figure 3: SEM images of typical morphologies of the inner structure of cones observed on the same sample electrodeposited at -0.8 V vs. Ag/AgCl at 80 °C from base to tip, revealing the individual nature of the growth and crystallization of ZnO inside different channels of the same membrane.

The breaking points of several cones of the same sample are shown in Figure 32. In all cases, the inner structure is completely different. In Figure 32a, the broken cone obviously consists of large faceted grains which can be detected at the breaking point of the cone. Figure 32b shows another broken cone with a completely filled base; however, in this case, the cone consists of features of smaller size and undefined shape. A tubular cone consisting of a thinner nanorod-based wall and a smoother outer wall is shown in Figure 32c. The wall of the tube, which was formed by nanorods, has a thickness of ~400 nm at the point where the cone broke. A very typical structure that was observed in many cones is shown in Figure 32d. The bases of the cones are almost completely filled and consist of very large grains having h and k conspicuous facets. The inset in this image shows the top view of the hexagonal plane (in blue) and the h planes (with dashed lines). Another hexagonal structure observed inside the cones was a helical tube (Figure 32e). These tubes, which had a length varying between 200 and 300 nm and a diameter between 100 and 150 nm (mainly 1:1 aspect ratio), formed the inner wall of the tubular base of the cone and were oriented randomly with respect to each other but parallel to the substrate. These structures are expected to have a strong reflection of family planes in the XRD pattern. Some other cones were filled with short nanorods and small hexagons, as shown in Figure 32f. Since these hexagons looked to be nicely positioned perpendicular to the wire growth axis, an enhancement of reflection signal during XRD measurement can arise from these structures. The mentioned three main reflections due to the structures shown in Figure 32 are the cone wall filled with grains consisting of all three types: solid hexagons forming a helical tube are shown in Figure 32g. In this case, the hexagons exhibited very diverse sizes and were oriented randomly. Last but not least, another common structure shown in Figure 32, was a cone filled with uniform nanorods with a length of 400 nm and a diameter of 70 nm.

Such a large variety of shapes made the complete array of cones (grown from base to tip) behave as a polycrystalline system. The homogeneity of the growth, which can be a result of poor diffusion and wetting processes through the small openings of the conical pores, leads to a rather poor mechanical stability. For this reason, the synthesis was inverted by growing the ZnO cones from tip to base. The applied conditions, namely the temperature, electrolyte and the potential were the same as for the cones grown from tip to base. A typical XRD pattern of a tip-to-base grown cone array embedded in the membrane is shown in Figure 33. As in the previous case, these cones also behave as polycrystalline with prominent h , k , and l and relatively lower m , n , and o reflections. The main difference compared to the base-grown samples is the dominant h reflection instead of k . No signal was detected from the h planes (Figure 33a).

angles. The inset in Figure 33 shows the schematic of the XRD setup alignment of the membrane with cones relative to the beam.

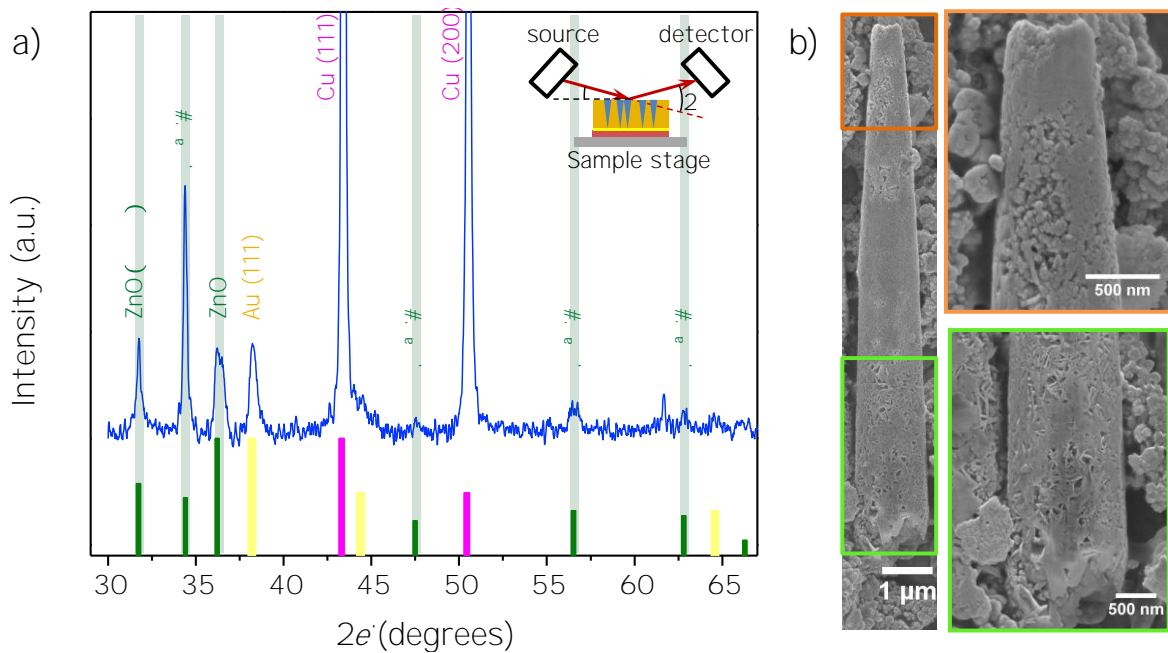


Figure 33 a) XRD pattern of a conical nanowire array grown from tip to base, the inset schematic representation of the XRD setup and the alignment of the sample relative to the beam, b) SEM images of a typical ZnO cone grown from tip to base. The highlighted zoomed images show the edges of the cone close to the tip (orange) and base (green).

The SEM image of a typical cone grown from tip to base is shown in Figure 33. In images of the two edges of the cone close to the tip (orange) and base (green) show a very rough morphology. These wires consist of arbitrarily oriented grains and walls which explain the polycrystalline character revealed by XRD.

To measure the tip and base diameters, individual cones were analyzed with SEM. These cones were mechanically very unstable and tended to break into pieces with a length between 5 and 15 μm (Figure 34a), thereby making it impossible to measure the diameters accurately. However, a closer look at these wires allowed the study of their morphology. Figure 34a shows a high magnification SEM image of two cones which consist of randomly oriented flakes, while the one in Figure 34b is mainly composed of very small sized features resulting in a very rough morphology. Figure 34c shows the edge of a cone closer to the base. The inset clearly reveals small hexagonal plates building the surface. However, it was unexpected that this amount of hexagons with randomly oriented planes could increase the reflection of the corresponding peak in the XRD pattern. Since XRD measurements were performed on the membranes still embedded in the membranes, the top view of the membrane with the cones inside was also studied. SEM images are shown in Figure 34 (e-g). Some of the wires developed caps while the surrounding pores remained not completely filled (Figure 34e). The diffusing ions might preferentially reduce on the caps rather than in

the pores. This means that the diffusion of ions from the electrolyte into the pores through the large opening of the cones (compared to the base growth) does not improve the homogeneity of these cones. Instead, due to the availability of higher concentration ions, a faster and preferential growth of hexagonal crystals of ZnO takes place which spread over the membrane as they reach the surface (Figure 34). Some of the hexagons can be single caps themselves, however, the size of the majority of the hexagons was smaller than the base diameter of the cones. These separate hexagons extracted from the larger caps and hexagons detached from the caps on the membrane are probably the main reason of the enhanced signal in the XRD pattern. Figure 34 shows a high resolution SEM image of an individual pore with homogeneous ZnO filling. All SEM images shown in Figure 34 belong to the same sample.

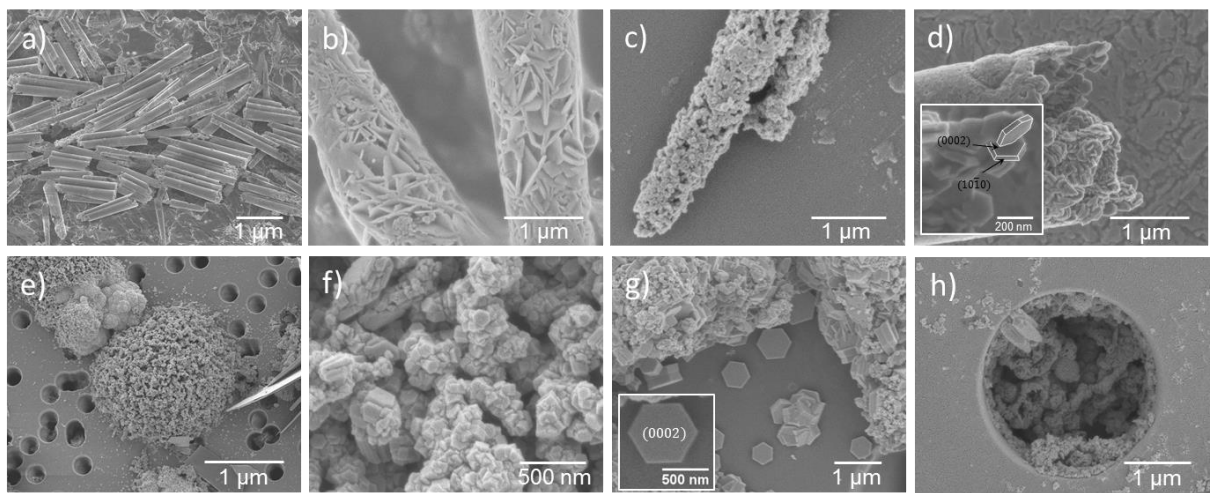


Figure 34 SEM images of (a) conical nanowires grown from tip at 0.8 V vs. Ag/AgCl at 80°C, (b) top view of the sample before polymer dissolution showing membrane with embedded ZnO cones, (c) top view of the sample after polymer dissolution showing membrane with embedded ZnO cones, (d) high-resolution SEM image of an individual pore with homogeneous ZnO filling, (e) top view of the sample before polymer dissolution showing membrane with embedded ZnO cones, (f) top view of the sample after polymer dissolution showing membrane with embedded ZnO cones, (g) high-resolution SEM image of an individual pore with homogeneous ZnO filling, (h) high-resolution SEM image of an individual pore with homogeneous ZnO filling.

Conical structures seemed to be promising for the synthesis of mechanically stable nanowire arrays due to the increased diameter of the base, serving as a supporting fundament. However, the expectations were neither for base-to-tip nor for tip-to-base growth method, probably because of the complex wurtzite structure of ZnO. To enhance the mechanical stability of the cones, a reverse-like network structure with preetched conical pores, as shown in Section 3.3 might be a solution. The network would serve as a reinforced fundament to obtain free-standing cones. Another alternative for mechanically stable nanowire-based structures is a network of wires, which is presented in the next section.

4.3. Nanowire networks

Compared to thin films, nanowire arrays possess a significantly higher surface area. Although there is a limit to the number density given by the overlap of the pores in the membranes due

to the random distribution of tracks. This restricts the further increase of the surface area of nanowire arrays. Alternatively, the length of the wires can be increased by fixing the number density. However, as mentioned for cylindrical and conical nanowire arrays in Sections 4.1.7 and 4.4, the mechanical stability becomes an issue when increasing the length or decreasing the diameter of the wires. This problem was avoided by using of network structures. Because of the complex matrix of the nanochannel networks, the electrodeposition of ZnO inside these templates had to be optimized. The synthesis and characterization of 3D nanowire and nanotube networks presented in this section.

4.3.1. Optimization of growth conditions for ZnO nanowire networks

For the fabrication of ZnO 3D nanowire networks, symmetrically etched templates with total nominal pore density of 2×10^9 , 2.5×10^9 , 4×10^9 , 8×10^9 , and 10^{10} cm^{-2} were employed. Throughout this thesis, the total pore density is referred as the sum of the fluence applied at different irradiation directions. e.g. if the PC foil was irradiated four times with a fluence of $2 \times 10^9 \text{ cm}^{-2}$, the total fluence will be $4 \times 10^9 \text{ cm}^{-2}$ which is given as 10^9 cm^{-2} . After etching on side of the membranes as first sputtered with a gold layer and then reinforced with a Cu or Au layer via electrodeposition (Section 4.1). All deposition conditions employed for the growth of parallel nanowires on a Cu substrate (potential between 0.5 and 0.8, 80 V) were subsequently applied to grow ZnO in membranes with interconnected nanochannels with pore diameter varying between 150–300 nm. The deposition potential of 0.8 V vs. Ag/AgCl at 80 V yielded reproducible and homogeneous growth in parallel channels, led to very low filling rates of the interconnected pores with a back electrode (as shown later in Figure 3.6a). No filling was observed when more positive potentials were applied. The complex channel geometry obviously has an influence on some of the processes involved in the electrodeposition, for instance, the diffusion and migration of the Zn^{2+} and OH^- ions inside the pores towards the working electrode. To adjust suitable deposition parameters for homogeneous and reproducible ZnO nanowire network growth, cyclic voltammetry was applied using 0.1 M electrolyte at 80 V on membranes with pore diameter of 220 nm, a density of $2 \times 10^9 \text{ pores/cm}^2$ and a Cu back electrode. Compared to templates with vertically oriented channels, of the reduction peak to more negative potentials, namely around 1.4 V vs. Ag/AgCl occurred. For nanochannel networks with a Au back electrode the reduction peak was close to 1.1 V vs. Ag/AgCl as in the case of parallel wires with a Au substrate. Among series of samples electrodeposited at 60, 70, and 80 V, electrodeposition at 70 V yielded the best filling for both substrates. Lower temperature resulted in a reduced deposition rate and thus in a homogeneous filling of the highly interconnected network channels.

Representative chronoamperometric curves for successful electrodeposition in network templates are shown in Figure 3.5. Both depositions were carried out in identical membranes with Au substrate and pore diameter and density of 50 nm and $2 \times 10^9 \text{ cm}^{-2}$, respectively.

Also the deposition conditions were the same, namely -1 V vs Ag/AgCl at temperature of 60 °C. Upon application of the potential, the measured current shows a sharp peak within the first few seconds, which is assigned to the charging of the double layer and formation of the diffusion layer, as explained in Section 1.2. Within the following 15 min, a second broad peak is recorded. The width of this peak changes from sample to sample and seems to depend on the porosity. This second peak was never observed for vertical wires and is probably related to the different growth mechanisms in network channels. Vassé *et al.* have reported a similar behavior for the electrodeposition of vertically aligned ZnO wires, explaining the second peak by the independent growth of ZnO nuclei that are smaller than the pore dimensions and the increasing surface area available for the nitrate¹³¹ reduction. After 15 min the curve in Figure 35c b h] b i Y g ` h c ` c g W] ` ` U h Y ` g \ decreasing with the growth inside the template proceeds, as the curve shown in Figure 35 stabilizes with time and shows the typical behavior known from the deposition of vertical wires. The oscillation effect was often observed and might be related to stepwise wetting with the electrolyte and hence with the increase of reduction charge deposition with time.

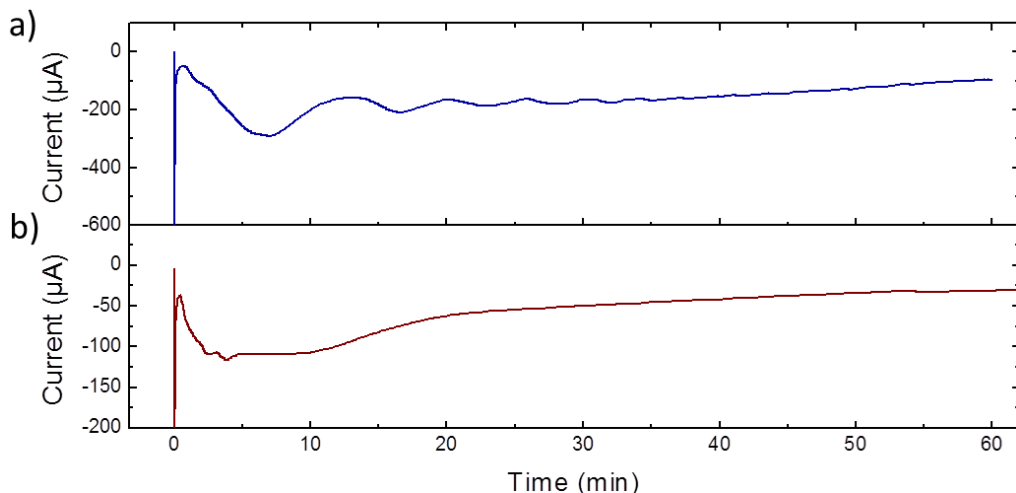


Figure 3 Two types of characteristic chronoamperometric curves of Zn membranes with a network with a pore diameter of 150 nm and a density of 80 pores/cm², grown at -1 V vs. Ag/AgCl and 60 °C.

To inspect the networks by SEM, the polymer matrix was dissolved in CH₂Cl₂. Figure 3(a) and (b) show two networks with a nominal wire diameter of 700 nm and a density of 10⁸ cm⁻² grown on a Cu substrate at different conditions shown in (a) $U = -0.8$ V, $T = 80$ °C and (b) $U = -1.4$ V, $T = 60$ °C. The network grown at high temperature and low potential (-0.8 V) looks sparse and incompletely filled, so that the substrate is visible through the network (Figure 3a). The inset reveals that the wires in the network possess undefined shapes due to poor filling of the pores. A homogeneous network grown at temperature 60 °C and higher potential -1.4 (V) is shown in Figure 3(b).

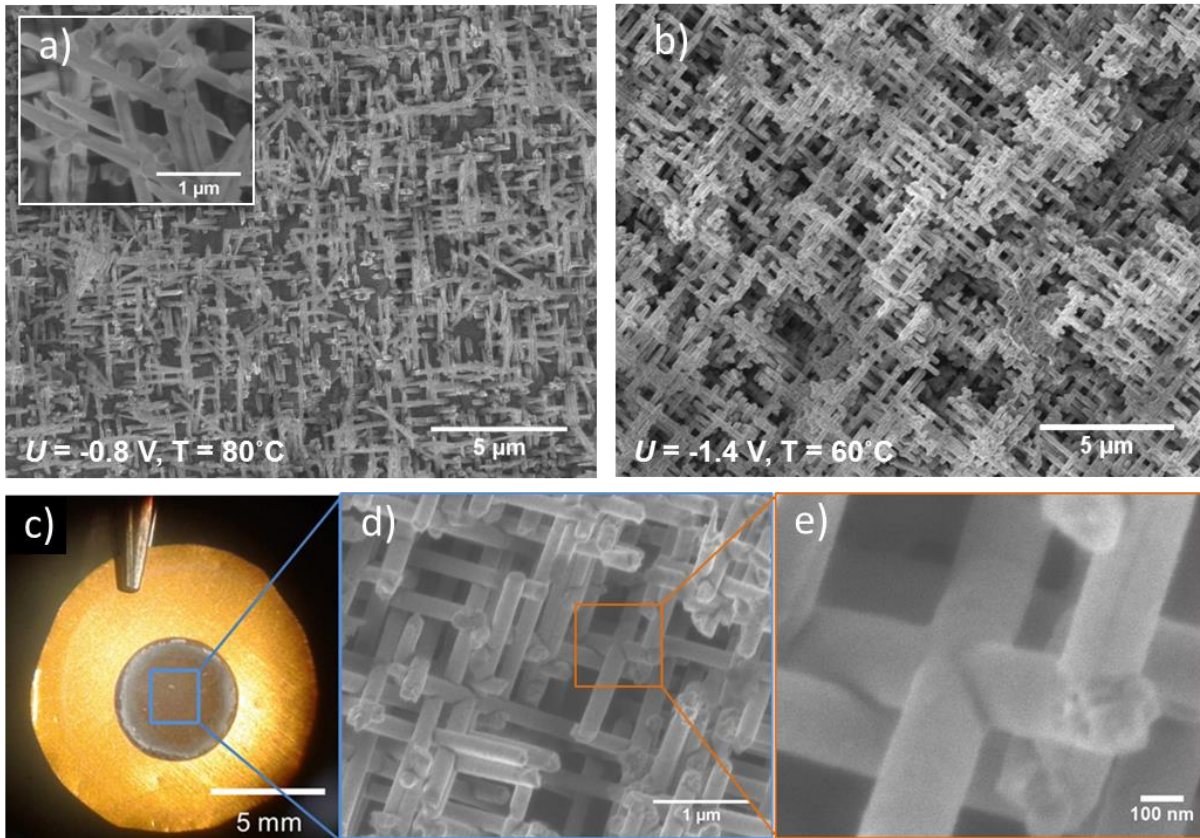


Figure 35 SEM images of two nanowire networks with nominal wire diameter of 220 nm and density of 10^9 wires/cm² deposited at different conditions (a) vs Ag/AgCl at 80 °C showing sparse filling and poorly shaped wires, (b) vs Ag/AgCl at 60 °C showing a good filling and well-defined cylindrical wires (c) Photograph of ZnO nanowire network on Au substrate with wire diameter of 190 nm and density of 10^9 cm², grown at 1 V vs. Ag/AgCl and at 60 °C and the corresponding SEM images of the network at (d) low and (e) high magnification

Figure 36 presents a photograph of a ZnO nanowire network on a Au back electrode after dissolution of the polymer membrane. The sample is easily handled with tweezers without damaging the network due to its high mechanical stability. The density and diameter in the network were in total 10^9 cm² and 190 nm, respectively, and the deposition was carried out at 1 V vs. Ag/AgCl and at 60 °C. The corresponding SEM images in Figure 36(d) and (e) show this network at low and high magnification, respectively, displaying an excellent interconnectivity between the wires. The connections serve both as points enhanced mechanical stability of the whole network and as electrical connection between several wires. It is worth mentioning that this network was deposited through a membrane which was irradiated with a mask where the ion irradiation was limited by a mask to 5 mm in diameter. The role of the mask is to limit the network area and to avoid leakage of electrolyte through the network pores at the edges of the membrane where no back electrode is deposited. To explain this principle, Figure 3 shows the schematic of two cells with membranes irradiated with (a) and with (b) a mask with 5 mm aperture in the center. The regions marked with R correspond to possible leakage through the pores at the

interface of the sample and the copper contact. The leakage of electrolyte to be observed for membranes irradiated without (a) mask while it is not possible for (b) since all pores are confined by the back-electrode. Another disadvantage of using the network templates with mask irradiation is that the wires are being deposited outside the area defined by the opening (diameter) of the Teflon cell. Whereas for the samples irradiated with mask the active area of the nanowire network after deposition is defined by the diameter of the irradiation mask. Figure 37(c) and (d) show photographs of etched membranes irradiated without and with 5 mm mask, respectively. An alternative to mask irradiation, the electrochemical cell can be redesigned. However, this would cause more technical issues, e.g. providing a homogeneous temperature in the solution.

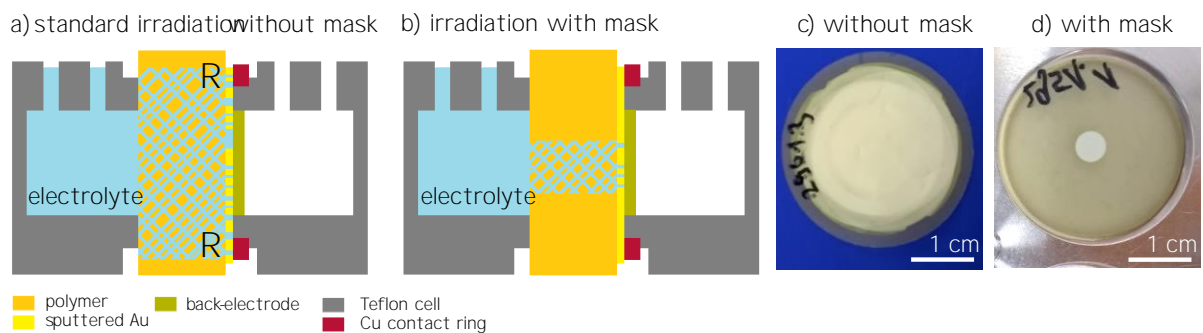


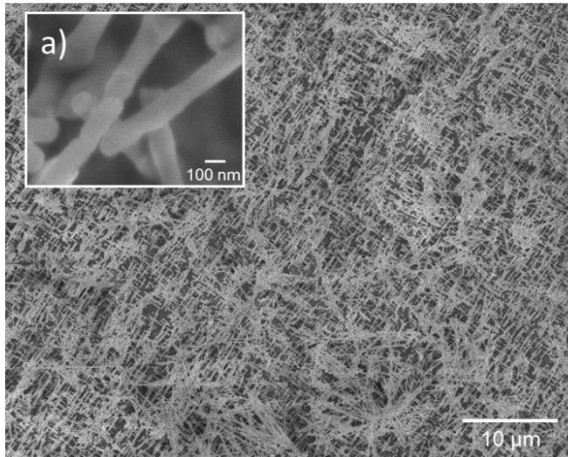
Figure 37: (a, b) Schematic representation of two electrodeposition cells with membrane without and b) with mask. The areas marked with F and U in the electrolyte can be thought of as the pores. Photographs of etched membranes irradiated c) without and d) with 5 mm mask.

The optimization of the wire density in the networks for improved mechanical stability is discussed in the next section.

4.3.2. Enhancement of the mechanical stability of the networks

Figure 38 shows two nanowire networks deposited in membranes with a diameter of 90 nm and a total density of a) 10^9 and b) 810^9 cm^{-2} (these PC foils were irradiated from four directions, each with a fluence of a) $5 \cdot 10^8$ and b) 210^9 ions/ cm^2). The electrodeposition was carried out at -1.4 V vs. Ag/AgCl at 60°C on a Cu back-electrode. The low magnification image in Figure 38 reveals an unstable network with interconnected wires being collapsed and forming bundles of wires. The high magnification image shown as an inset elucidates the lack of interconnections between the wires, which explains the instability of this network. In contrast, the network with a higher density of wires is shown to be very stable (Figure 38). The vast number of interconnections stabilizes the whole network structure and makes it free-standing. The inset in Figure 38 shows several crossing wires yielding a dense matrix. At very high number densities, the network will become too dense, losing the advantage of the one-dimensionality due to the significant overlap of wires along their length, resulting in unfavorable transport properties.

$4 \times 5 \times 10^8 \text{ cm}^{-2}$



$4 \times 2 \times 10^9 \text{ cm}^{-2}$

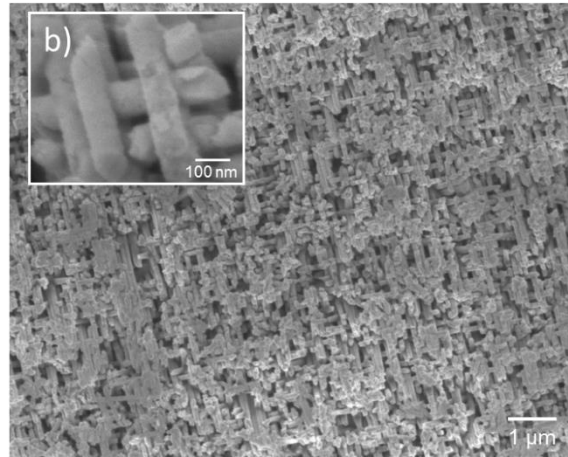
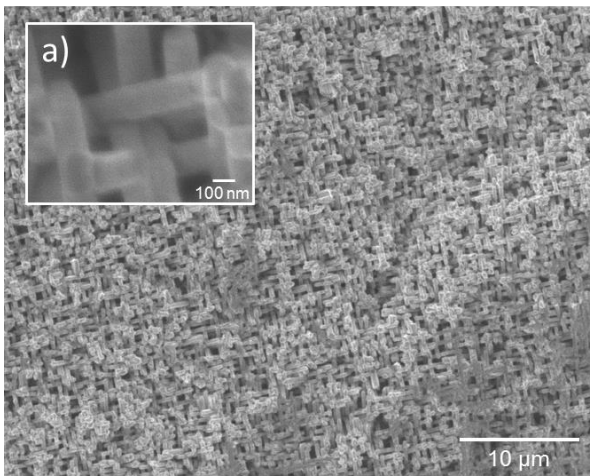


Figure 38: SEM images of nanowire networks with a wire diameter of 90 nm and number densities of a) $4.5 \times 10^8 \text{ cm}^{-2}$, and b) $4.2 \times 10^9 \text{ cm}^{-2}$, showing an enhanced mechanical stability for the network at a higher density.

The space between the wires (wire spacing) strongly depends on the density and diameter of the wires. Figure 39(a) and (b) show SEM images of networks having an identical density ($2 \times 10^8 \text{ cm}^{-2}$) but different diameters of wires being 150 and 210 nm. A stable network with dense individual wires with a diameter of 150 nm is revealed in Figure 39(a) whereas the nanowires with larger diameter (210 nm) overlap and merge significantly (Figure 39(b)).

$\varnothing 150 \text{ nm}$



$\varnothing 210 \text{ nm}$

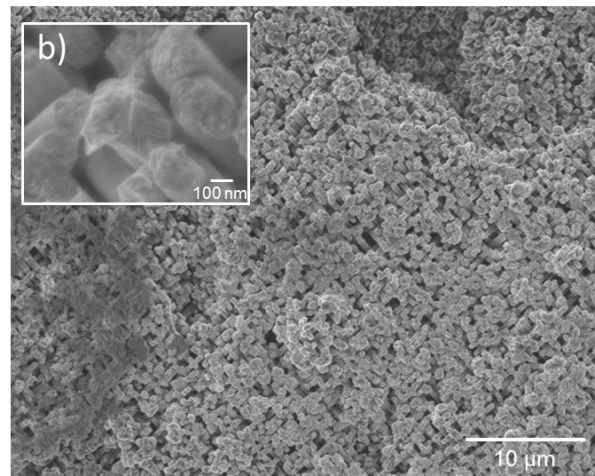


Figure 39 SEM images of nanowire networks with a wire density of $2 \times 10^8 \text{ cm}^{-2}$ and diameters a) 150 and b) 210 nm. The networks possess significant overlapping because of the large diameter.

To obtain networks which have large wire spacing and high stability at the same time networks were synthesized in membranes which were irradiated with an additional film position parallel to the surface normal. The preparation of membranes with combination of tilted and vertical pores is described in Section 3.3. The main advantage of these structures is the increase of the number density of wires without a significant increase of overlapping.

effect, which would be more probable as of irradiation from only four directions but with higher fluence. Additionally, the vertically oriented pores facilitate the wetting and diffusion of ions inside the membranes resulting in more homogeneous network growth.

SEM images of network with additional cylindrical wires oriented perpendicular to the substrate are shown in Figure 40. The diameter and number density of the wires are 150 nm and $5 \cdot 10^9 \text{ cm}^{-2}$, respectively. The low and slightly higher magnification SEM images (Figure 40a,b) show homogeneous growth of the network over the complete substrate. Figure 40 shows zoomed in SEM image and corresponding 3D representation of the network, the tilted wires of the network are marked in blue, and the red indicates the vertically aligned wires. The tip of the tilted wires show an oval shape, whereas the tips of vertically aligned wires have a perfect circular shape when looking from the top of the network. The high magnification SEM image of the area marked in orange is shown in Figure 40c, which displays junctions between multiple wires. Regions marked in white illustrate that many wires can cross through each other at the same position. Several of the tilted and vertically aligned wires are marked with blue and red, respectively. The advantage of this network structure is that the overlap of wires is limited to junctions, and the wires have almost no overlap along their length until the next junction with this keeps the one dimensionality of the structure, especially for applications where the size of the structure should be comparable to the diffusion length of the charge carriers in order to minimize the recombination probability for photoelectrochemical water splitting. Another high magnification SEM image is shown in Figure 40d, which clearly shows wires with different orientations (one tilted and one perpendicular to the substrate).

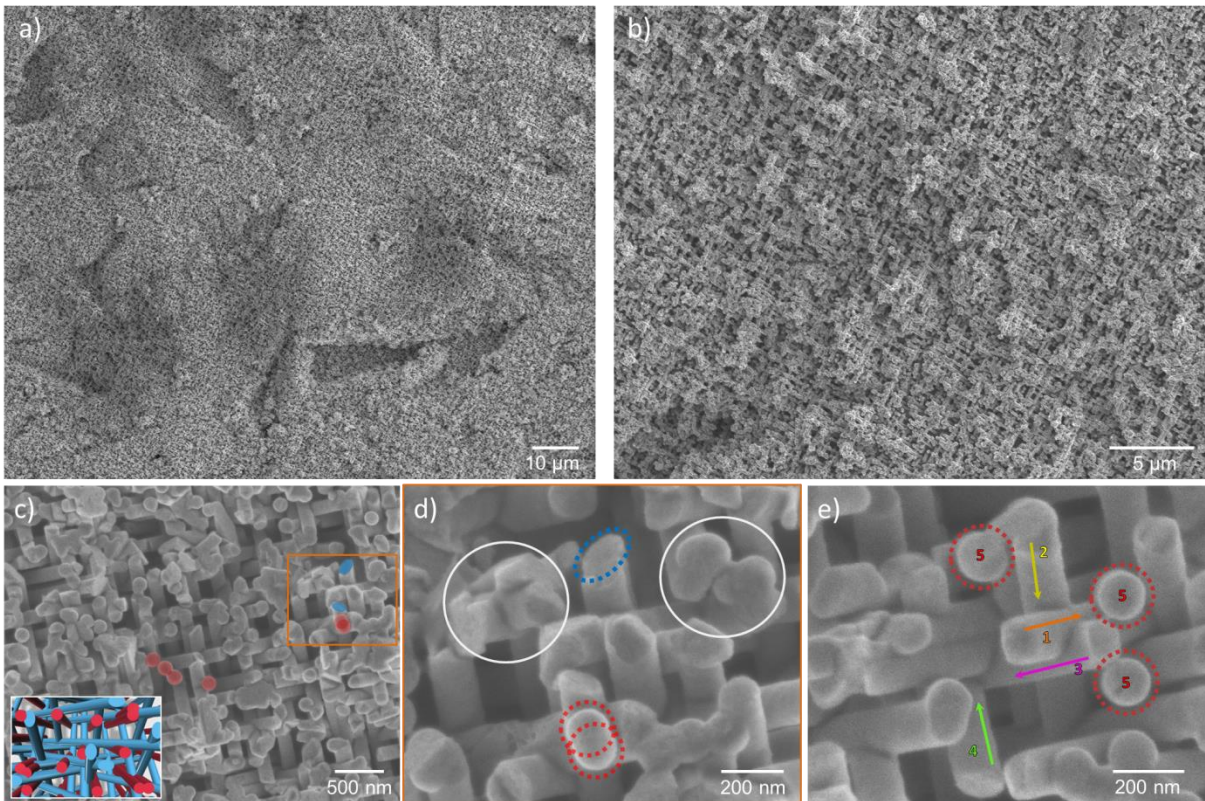


Figure 40 SEM images of nanowire network with a wire diameter and density of 150 nm and 10⁸ wires/cm² respectively. (a) Low magnification SEM image of parallel cylindrical wires and (b) high magnification SEM image of the network. The inset in (c) shows a 3D illustration of the top view of the network with wires tilted perpendicular (red) with respect to the substrate. (d) and (e) are zoomed SEM images of the network showing intersections of several wires and the five orientations of

The flexibility of the ion-track technology provides a wide range of diameters and wire densities, but the selection of diameter and density should be done carefully. Therefore, the limits and challenges of fabrication of ZnO nanowires with high number density were investigated and discussed in the next section.

5. Passivation of ZnO nanowires and nanowire networks with TiO₂ shell

This chapter provides knowledge about the crystallinity and composition of ZnO networks as well as TiO₂ shell of ZnO/TiO₂ nanowire and networks coated by atomic layer deposition at different temperatures.

5. ZnO nanowires and nanowire networks with a TiO₂ shell

To protect ZnO nanowires from corrosion and make them more suitable for photoelectrochemical measurements, core/shell structures with a titania (TiO₂) shell were investigated. The TiO₂ layer is expected to protect ZnO from (electro)chemical corrosion in aqueous media. Different combinations of ZnO and TiO₂ structures are known from the literature as photoelectrodes for photoelectrochemical dye sensitized solar cells or biological applications.^{61,132,133,134} In this chapter, two types of ZnO/TiO₂ core/shell structures are discussed: i) nanowires coated with amorphous titania, and ii) nanowire networks with a TiO₂ shell.^{135,136}

5.1. ZnO nanowires with amorphous TiO₂ shell

Array of ZnO nanowires with a diameter of 80 nm was electrochemically deposited on a D 7^{a} Y (10 pores/cm²) by applying -0.8 V vs. Ag/AgCl at 80°C using 0.1 M Zn(NO₃)₂·6H₂O. After subsequent dissolution of the polymer matrix, the nanowires were coated with TiO₂ at 110°C at GSI using a flow-type ALD reactor-200 Basic from PICOSUN™. As first and second precursors and purging gas, TiCl₄, H₂O, and N₂ were used respectively. One cycle consisted of 5.2 s of TiCl₄ and 0.4 s of H₂O exposure, and 50 s purging with N₂ between the exposure steps. 950 cycles were applied to deposit a 10 nm thick layer.⁵⁸

Figure 41(a) and (b) illustrate schematically an electrodeposited and coated ZnO nanowire. The SEM image in Figure 41 shows several wires on a Au TEM grid. As expected, there are continuous and completely filled. In the SEM image inspected by using a low secondary electron detector transmission mode (Figure 41d), the slight contrast at the edges and along the wires is assigned to the TiO₂ shell. In the corresponding ED spectrum (Figure 41e) the L and K lines of Zn originate from ZnO, the K lines of Ti result from the TiO₂ shell. The C and Au signals are assigned to the Au TEM grid with carbon film. In addition, Cu L and K lines are detected, which are better visible in the inset in Figure 41e.

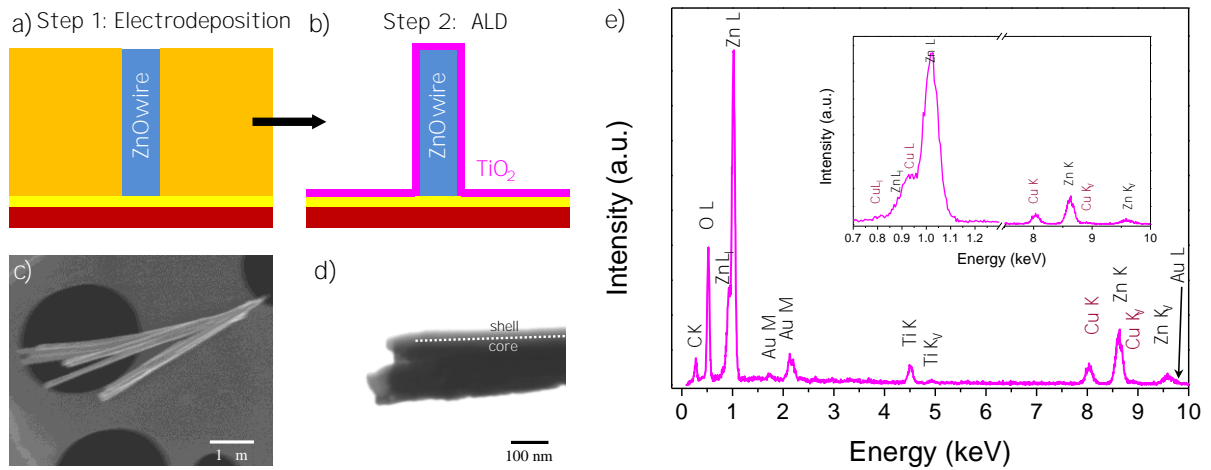


Figure 4: (a-b) Schematic representation of the a) electrodeposition of ZnO wires on a substrate, and b) atomic layer deposition of TiO₂ shell on top of ZnO nanowires after dissolving the polymer matrix. (c) TEM image of ZnO/TiO₂ core/shell wires captured with a c) scanning electron detector and d) low-magnification secondary electron detector in transmission electron microscopy. (e) EELS spectrum of a ZnO/TiO₂ core/shell wire.

To understand where the Cu signal originates from, the ZnO wires were investigated using high-resolution transmission electron microscopy (HRTEM) with high-angle annular dark field (HAADF) imaging and electron energy loss spectroscopy (EELS) in collaboration with Dr. Wilfried Sigle at the MPI for Solid State Research in Stuttgart. The HAADF image of a ZnO/TiO₂ nanowire is shown in Figure 2a. The ZnO core and the TiO₂ shell can be distinguished due to the contrast difference. The core is continuously coated with a homogeneous TiO₂ shell (~7 nm) and some surface voids due to the roughness of the ZnO wire. Figure 4(b) and (c) present the elemental mapping and the EELS spectrum, respectively. The spectrum image clearly shows the presence of Cu in the wires (blue), which is confirmed by the spectrum in Figure 4(e). These ZnO wires obviously contain Cu contamination, most probably arising from the diffusion of Cu from the substrate into the ZnO wires. Cu diffusion into ZnO is a known effect which is often used to dope ZnO with Cu¹³⁹, e.g. for ferromagnetic application of ZnO:Cu systems.¹⁴⁰ Figure 4(d) shows a low-magnification HAADF image of several ZnO/TiO₂ nanowires where areas of contamination with Cu can be detected due to the color contrast (marked with blue arrows). The inset shows a feature with well-defined edges which suggests that the structure is crystalline. For the investigation of the synthesis process of ZnO nanowires and their characterization, contamination with copper is an undesired effect. Thus, for further ZnO synthesis, Au substrates were used (especially for photoelectrochemical measurements).

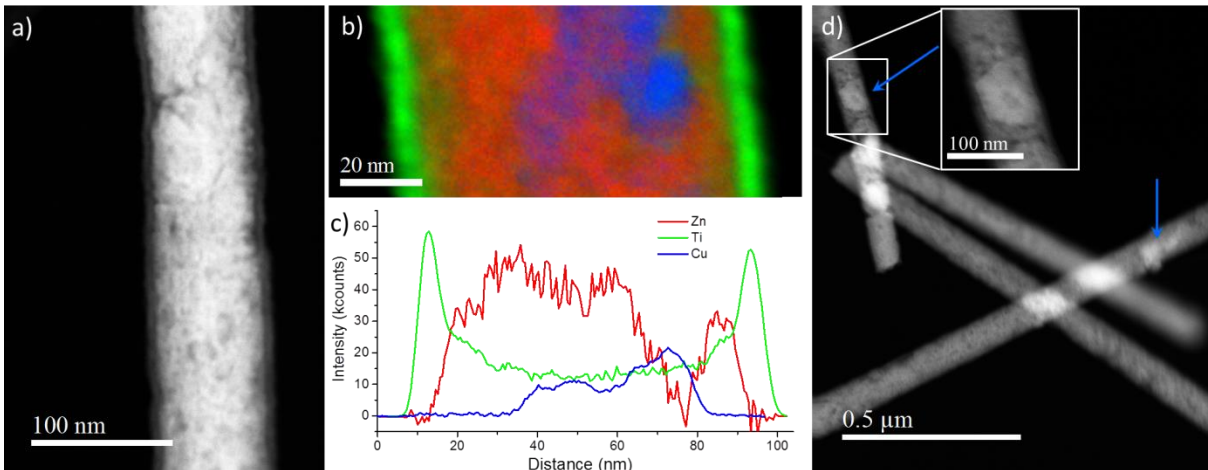


Figure 4: a) HAADF image of ZnO/TiO₂ nanowire with 100 nm core and ~7 nm shell (b) elemental mapping and c) EELS spectrum of corresponding nanowire showing presence of Cu in some areas of the wire d) low magnification HAADF image showing areas on nanowires with (marked by arrows) with possible Cu contamination. The inset shows a small crystal with well defined edges

To measure the coating thickness more precisely and to investigate the crystalline structure of the core/shell wires HRTEM was applied. Figure 3a presents a low magnification HRTEM image of several nanowires lying on a Au TEM grid. The corresponding TEM image of the area marked with a yellow frame is shown in Figure 4b. The cores of the wires show sharp and continuous fringes corresponding to the (0002) planes of ZnO, according to the measured plane distance being 0.26 nm. However, in some small areas with defined fringes, the measured distance of the planes was smaller, namely 0.36 nm (Figure 4c), which matches well with the spacing value of the (111) planes of CuO. This can mean that in the ZnO nanowires the Cu detected by EELS measurements, exist as an oxide state. HRTEM images of different areas of a ZnO/TiO₂ core/shell nanowire are shown in Figure 4d (e). The mean thickness of the shell is 8 nm. In general, the TiO₂ layer looked amorphous, which is expected for low temperature ALD of TiO₂. However, fringes were detected in some areas of the shell (see framed areas in Figure 4.3). The white lines show the orientation of the fringes. Two high magnification HRTEM images of areas marked in Figure 3a are shown in (f) and (g). The measured spacing matched with the (101) planes of anatase, which was confirmed by the Fourier transform image (Figure 4.3) of the area shown in Figure 4.3. So, it can be concluded that TiO₂ shell ALD-deposited at 110 °C has an amorphous structure, with some areas consisting of fringes corresponding to the anatase phase of titania.

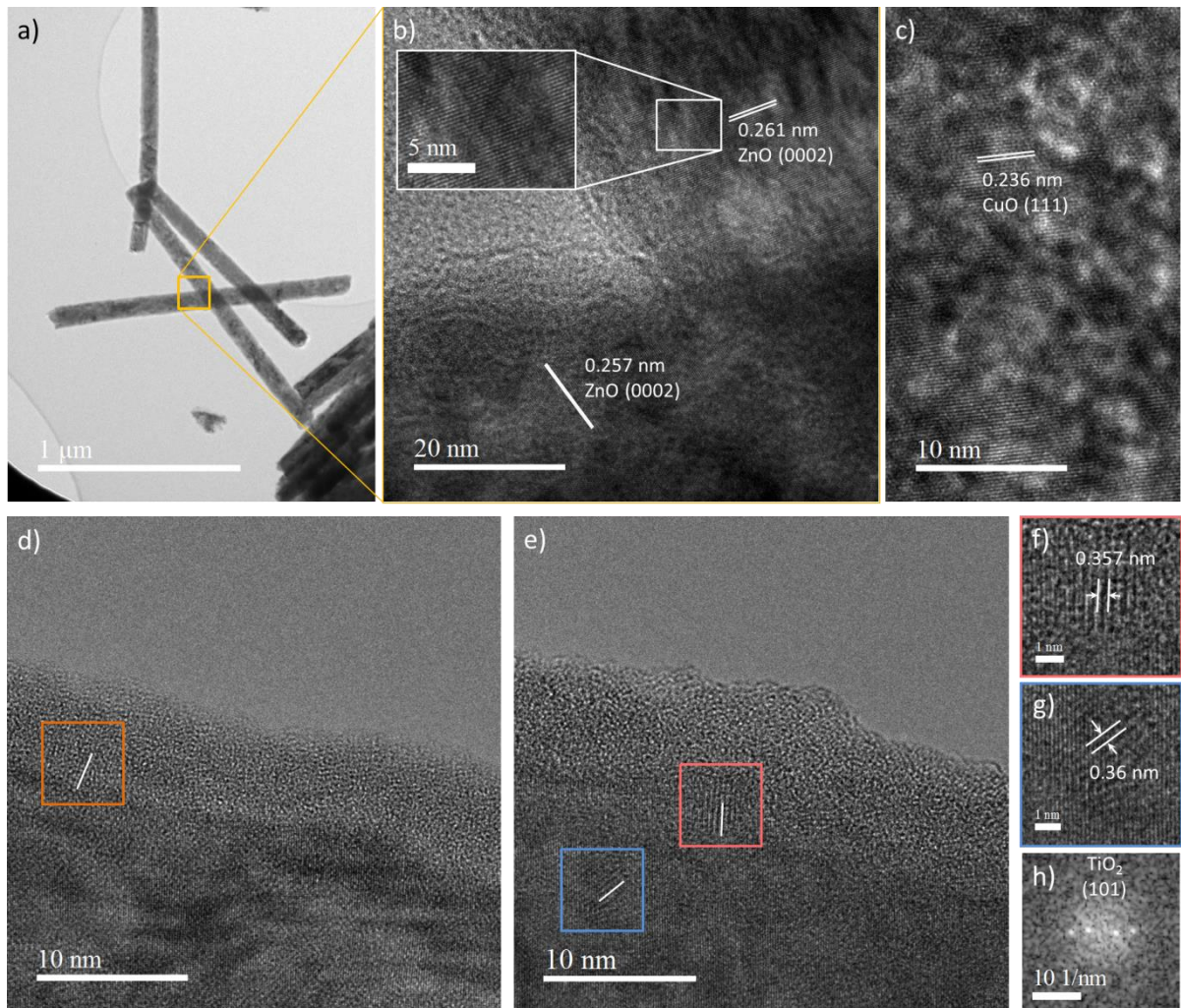


Figure 3. HRTEM images of (a) ZnO/TiO₂ core/shell nanowires at low magnification showing the well-ordered and continuous planes of ZnO (0002) spacing of ~0.26 nm and (b) high magnification image of a nanowire which consists of well-ordered fringes with a plane distance of 0.26 nm corresponding to the (111) plane of monoclinic CuO. (c) HRTEM image of a core/shell nanowire with a thick shell, which has small features showing fringes with small features on the shell in high magnification, with measured d-spacing of 0.356 nm which can be related to anatase TiO₂ (101). (d) Fourier transform image corresponding to (f) confirming that the observed planes are titania.

5.2. ZnO and ZnO/anatase-TiO₂ core/shell nanowire networks

ZnO nanowire networks were electrodeposited in membranes with Au substrates at Ag/AgCl and 60°C using 0.1 M Zn(NO₃)₂·6H₂O. For some series of samples, a TiO₂ layer with a thickness of 20 nm was deposited on the network (total number density of 10⁸ cm⁻²) using ALD. The temperature of the ALD process was increased to 150°C in order to obtain crystalline TiO₂. For better transport properties, the deposition was carried out by using TTIP as a first precursor with an exposure time of 1 min, followed by purging with N₂ for 30 s. The exposure of TiCl₄ as a second precursor was 1 min and the residual molecules were afterwards purged with N₂ for 30 s. According to the calibration value, these parameters result in a deposition of 0.0197 nm² TiO₂ per cycle, i.e. to achieve a ~20 nm coating thickness 1000

cycles were applied to study the influence of the temperature in the ALD chamber on the morphology of the ZnO nanowire network, the samples were systematically studied by SEM before and after ALD.

Figure 4 shows SEM images of the same sample before (a) and after (d) TiO_2 coating in different magnifications. The low magnification images (a, d) give an overview of the homogeneous growth of the network. Higher magnification images (b, e) show a denser matrix for the image after coating, which is related to the layer decreasing with interwire spacing. Images at even higher magnification (c, f) show that the network underwent a morphological modification. Before the ALD process, the wires have tips with sharp edges, looking almost like needles. After coating the tips look rounded, which indicates that the high temperature has a slight influence on the morphology. However, it is important to note, after ALD the wires did not change their cylindrical shape and the network structure with interconnected wires in a random fashion. The diameter of the wires measured before and after the ALD process was 50 and ~ 190 nm, respectively, which matches with the expectation of a ~ 20 nm thick coating.

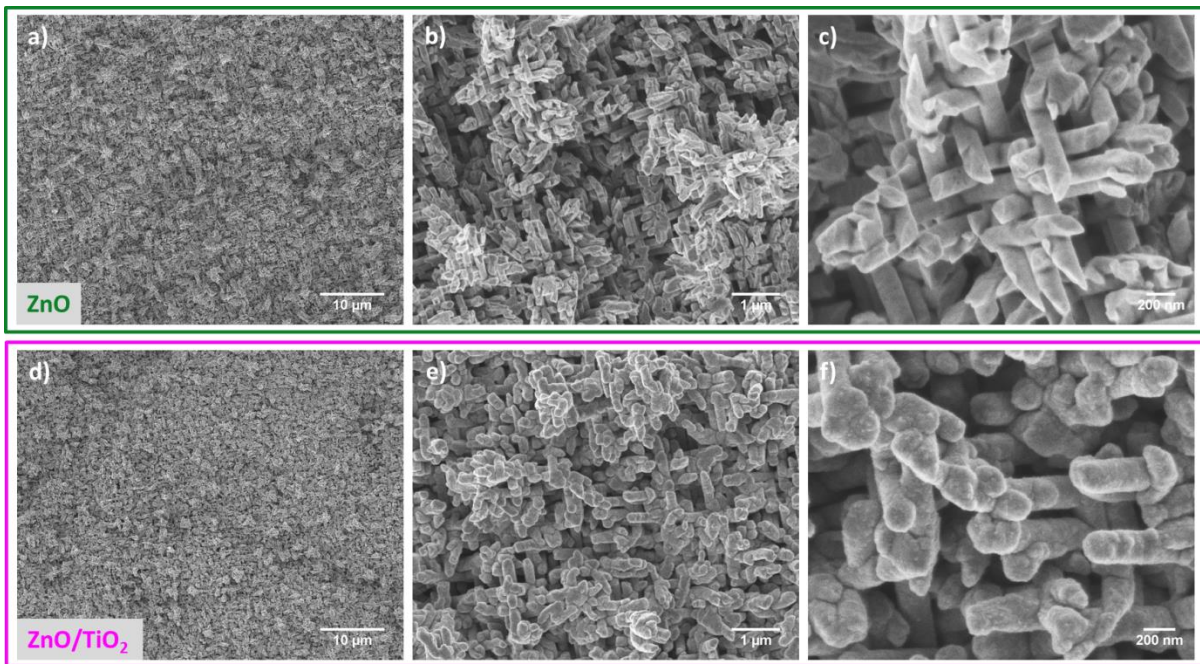


Figure 4 SEM images of the same ZnO wire network with a number density of 810^8 cm^{-2} and a diameter of 150 nm before (a, b, c) and after (d, e, f) ALD coating at 250 °C with ~ 20 nm thick TiO_2 .

The corresponding EDX spectra of this sample before and after coating are shown in Figure 4.5. In both cases the characteristic L and K lines of Zn and the L line of O are detected. In the spectrum measured after coating, L lines of Ti are also observed. The Au peaks are assigned to the Au substrate of the network, and the Al signal originates from the SEM sample holder. No other peaks were detected, meaning that there were no impurities in the wires.

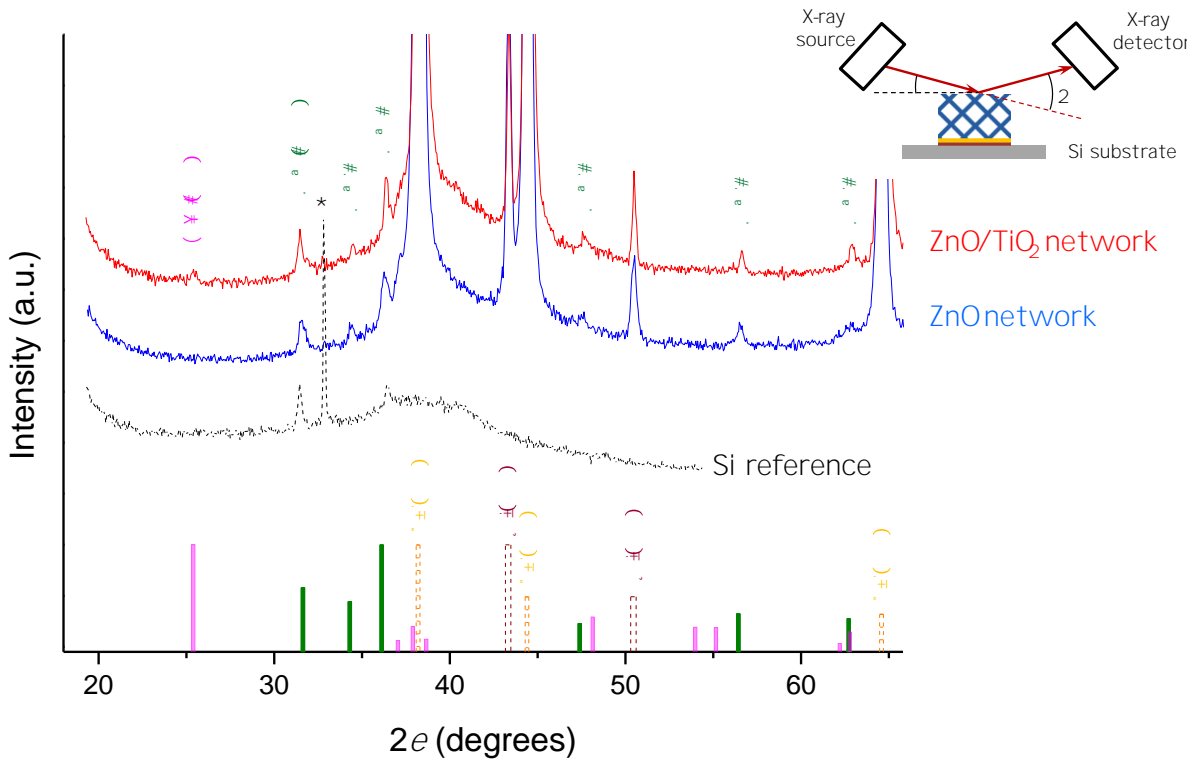


Figure 4.6 XRD diffractograms of bare (blue) and -20 nm TiO₂ coated (red) ZnO nanowire network. The coated samples show a reflection corresponding to (101) planes of ZnO. The asterisk (black) is from the Si reference sample which served as a substrate for Au and Cu signals originate from the network substrate itself.

Because of the complex structure of nanowire networks which consist of individual wires having $U \cdot h \cdot h$ respect to the surface normal, the many interconnections between them, more precise techniques were required for further analysis of crystallinity as well as the morphology and elemental composition. The ZnO and ZnO/TiO₂ wires detached from the networks were further investigated using HRTEM, HAADF, and EELS. The samples imaged with SEM after transferring them onto TEM grid are presented in Appendix E.

Figure 4.7 shows the HAADF image of a ZnO nanowire from a nanowire network. Due to the contrast difference, small gray/black areas are noticeable on the wire, which represent surface voids that arose from the roughness of the network. In Figure 4.7g high magnification HAADF image of the same wire is shown. Within the entire area, the wire exhibits continuously ordered layers. The higher magnification images of the areas numbered with 12, and 3 are shown in Figure 4.7, and e), respectively. These images reveal the well-defined layers, including in the area of the void (e) and prove the continuous growth of the same planes being ZnO (0002) according to the measured spacing of 0.257 nm.

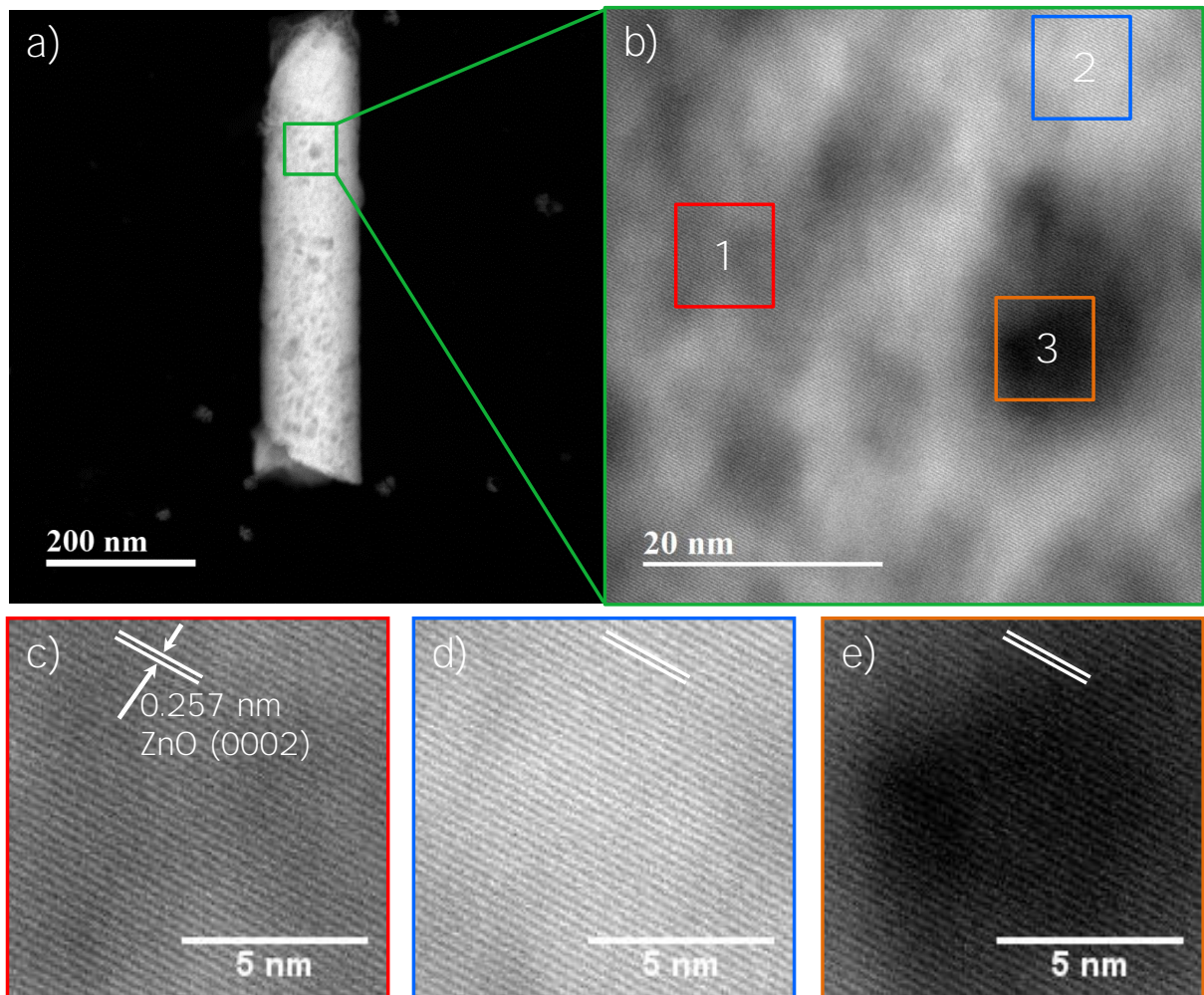


Figure 4: HAADF images of a) coated ZnO nanowire with a diameter of 150 nm, (b) correspond to voids arising from the roughness of the wire; b) the wire shown in (a) magnification, elucidating the continuously layered structure independent on the void between the wire axis and the growth direction, and c, d, e) three areas indicated in (b) magnification, showing similar and well-ordered layers.

The results of HRTEM studies on the structural properties of both ZnO wires and ZnO/TiO₂ are presented in Figure 4. The HRTEM image of ZnO (Figure 4a) gives similar information as the HAADF images shown in Figure 4. The measured distance between the planes was 0.26 nm indicating that the observed planes are (0002). The lattice fringes are continuous along the wire (including the edge) without any disorder. The corresponding SAED pattern of the wire is shown in Figure 4b. The wire shows a strong diffraction of (0002) planes of hexagonal ZnO, indicating that the wire has a rather single crystalline nature in the analyzed area. Network wires coated with nominal 20 nm TiO₂ also show a crystalline ZnO core and a polycrystalline TiO₂ shell (Figure 4c). It has a texture of (101) planes of the anatase phase according to the measured plane distance of 0.353 nm. In Figure 4d, so twin grains with the same (101) planes can be detected. The measured thickness of the TiO₂ shell was ~19 nm, which is in good agreement with the expected coating thickness of ~20 nm. Fringes of ZnO with (0002) and (010) planes were also observed for this wire. Figure 4e shows the

SAED pattern of a core/shell wire with strong reflections of the ZnO (0002) and (002) planes and weak reflections of the TiO₂. The inset reveals the Fourier transform image of the TiO₂ shell without an influence from ZnO core, which was created from the HRTEM image shown in the inset in Figure 4.8. The spacing measured from the Fourier transform image was 0.352 nm, which matched well with the value measured from HRTEM corresponding to the (101) planes of anatase TiO₂.

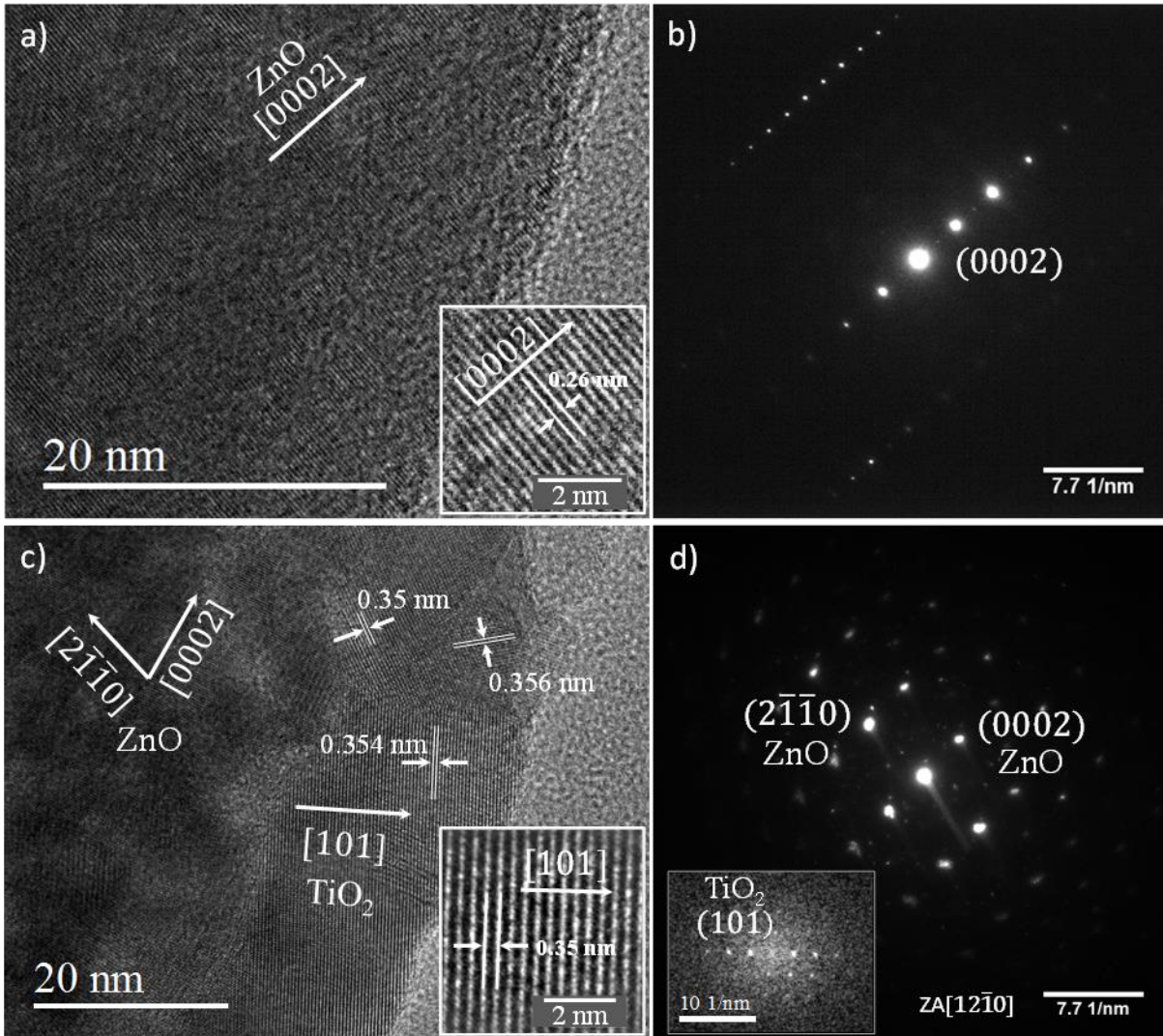


Figure 4.8 HRTEM images of a) ZnO and ZnO/TiO₂ nanowires. The insets show magnification images with measurements of 0.26 nm (a) and 0.35 nm (c) corresponding crystallographic planes of ZnO (0002) and TiO₂ (101) respectively. SAED pattern of c) ZnO/ZnO/TiO₂ nanowires with inset in (d) showing the Fourier transform image of the TiO₂.

It was also possible to image a region from the tip of wires extracted from a core/shell network. Figure 4.9 shows the HRTEM image of this area, with an inset zoomed-in region presenting ordered fringes which belong to ZnO (0002) planes according to the distance between the planes. The corresponding SA pattern is given in Figure 4.9. The bright points arise from the (0002) planes of ZnO, while the intense points (marked with green arrows in the image) assigned to anatase TiO₂.

planes based on the value of the calculated spacing (Figure 49c) and (d) show a HAADF image of a junction of two wires and the corresponding mapping by EELS, respectively. Both images prove the conformal coating of the ZnO wires with a continuous layer of 20 nm TiO₂. EELS spectrum image is displayed in Figure 49e along with a chemical composition profiles across the wire shown in Figure 49f.

Figure 4.9a) HRTEM image of an intersection area of two wires, showing well-resolved wurtzite ZnO with (0002) planes having a spacing of 0.264 nm, b) the corresponding SAED pattern of the area shown in (a); c) HAADF image of a junction of two wires, corresponding to the area shown in (a); d) corresponding elemental mapping by EELS showing a conformal coating of 20 nm TiO₂ layer; e) zoomed EELS spectrum image and f) corresponding chemical composition profile of the ZnO nanowire.

Based on the structural and compositional analysis of the ZnO wires coated with a layer of ~20 nm TiO₂ at 250 °C, it is possible to conclude that the wire network consists of a ZnO core preferentially oriented along the [0001] direction. Some fringes (200) planes (200) were also observed. The growth at the junctions is complete with continuous planes. The wires are uniformly coated with a homogeneous and polycrystalline TiO₂ consisting of twin grains with mainly (101) planes of the anatase phase. While the XRD pattern shows various reflections indicating a polycrystalline nature of the wires, analysis revealed highly crystalline sections of wires, which is an important property for efficient transport with minimized recombination of charge carriers. Further investigations are required to determine the grain size and observe the presence of grain boundaries.

Bare ZnO and core/shell ZnO/TiO₂ nanowire networks similar to those presented in this section were used as photoanode model systems to test the compatibility of these network structures for photoelectrochemical water splitting, which is presented in Chapter 6.

